Headwinds and Bow Shocks:

The Interaction of Relativistic Outflows from Compact Objects with Interstellar Matter

by

Doosoo Yoon

A dissertation submitted in partial fulfillment of the

requirements for the degree of

Doctor of Philosophy

(Astronomy)

at the
University of Wisconsin – Madison

2015

Date of final oral examination: July 9, 2015

The dissertation is approved by the following members of the Final Oral Committee:

Sebastian Heinz, Professor, Astronomy
Ellen Zweibel, Professor, Astronomy and Physics
Richard Townsend, Associate Professor, Astronomy
Elena D'Onghia, Assistant Professor, Astronomy
Dan McCammon, Professor, Physics

Abstract

An X-ray binary is a stellar binary system in which one of the components is a compact object (a black hole or a neutron star). The companion star transfers its gas to the compact object, and in some X-ray binaries the portion of the energy accreted to a disc produces a relativistic jet. The jet interacts with ambient medium, generating observational signatures, which are crucial in understanding jet dynamics and inferring the physical properties for the jet and the compact object. However, developing a theoretical framework for the interactions has been challenging.

X-ray binaries are classified into two sub-categories based on the mass of their companion stars: high-mass X-ray binaries and low-mass X-ray binaries. In this thesis, I have performed a theoretical study of the jet-interstellar matter interaction for both systems. In Chapter 2, attention is given to the evolution of jet trails and bow shocks in fast-moving low-mass X-ray binaries. I have numerically proven that the interaction between the radio plasma released by microquasar jets from such high-velocity binaries in the interstellar medium always produces a structure that consists of a bow shock, a trailing neck, and an expanding bubble, which is detectable in H_α and X-ray emissions. In Chapter 3, I extended this model to a bow-shock pulsar wind nebula, particularly the Guitar Nebula, which has apparent multiple bubbles behind the pulsar. In this study, I focused on the effect of inhomogeneous ambient medium

on the evolution of bow shocks and bubbles. I showed that when the pulsar encounters a density discontinuity, the bubbles can be produced due to the abrupt change of the standoff radius, at which a pressure balance occurs between the pulsar wind pressure and the ram pressure from the ambient medium. In Chapter 4, I studied the interaction between microquasar jets and stellar wind from the companion star in high-mass X-ray binaries. I derived a robust analytic solution of the jet-bending angle as a function of jet power and wind thrust, and applied it to Cygnus X-1 and Cygnus X-3 to constrain their minimum jet kinetic power.

To Chooza, and my little angels

Whom I love with all my heart forever and ever.

Acknowledgements

I would like to begin by saying that I have long dreamt for this moment of writing the acknowledgements section. When I looked at sparkling stars over the night sky for the first time, the vast universe was full of curiosity to me. This curiosity has led me to step in the astronomy field, and now I feel I have more questions about the universe than I had at the start of my academic journey. I would like to thank God for creating the universe with some rules so that I can dare to even try to answer the questions.

I truly appreciate my advisor, Sebastian Heinz. Without his expert guidance, this thesis would be incomplete. My work has had a shape of *science* by his efforts on teaching and training me to overcome numerous academic challenges. Also, I specially thank Brian Morsony, who helped me improve my skills and knowledge in a vast number of discussions. When I joined our group, Samuel Friedman and Paul Sell warmly embraced me, which made it easier to become acquainted with the group. Thank you all. For the current group members, Yi-Hao Chen and Gandhari Wattal, your hard work has always stimulated me. I believe you will have great success in your work. I also wish to thank my thesis committee — Ellen Zweibel, Richard Townsend, Elena D'Onghia, and Dan McCammon — for their involvement. Their thoughtful and insightful feedback gave me a chance to see my work in a

bigger picture. I have benefited greatly from individual discussions and classes in the department, but I must especially thank Jay Gallagher, Senzana Stanimirovic and Alex Lazarian for giving me useful insights.

To my fellow graduate students, Katelyn Milliman, Greg Mosby and Nick Hill. I always keep in mind how we went through the courses and pre-lim together. And to Thiem Hoang, Blakesley Burkhart, Erin Boettcher, and Alisha Kundert, you are the best officemates. I took over the desk from Isak Wold who has two kids, and now I will be the father of two kids in two months also. Thanks Isak, and I wish this productivity continues to next person who will occupy this desk. Steve Anderson, Sheri Pittman, Gary van Ryzin, and Angela Normington have always supported me from the astronomy office, and Aaron Teche has revived my computer and servers with magic whenever those machines were in malfunction. Without their help, I would have been distracted by overwhelmed tasks outside the research.

Outside the department, I need to thank many people who have guided me in the direction through which I would better walk. I appreciate Prof. Wong-Tae Kim who led me to join the field of the computational astrophysics. He has fully supported me even after I detached myself from his group a while ago. And, thanks to Enrico Ramirez-Ruiz who showed interest in my work and supported me. In addition, Andrzej Zdziarski gave me insightful feedback to improve my paper substantially. Whenever I was stuck in using python with YT, Matthew Turk always immediately responded to my questions and resolved the issues that I encountered.

In addition to the aforementioned astronomers, I am also fortunate to have the best teachers for my daughter at VA Kids: Marisa, Barbara, Christy, and Cyndi. Without their thoughtful and attentive care to my angel, I could have not focused

on my work.

Being a parent as a grad student has not been easy for me. But, my parents and mother-in-law have always supported my family, enabling us to determine our future track without any distractions.

And lastly, but certainly the most important person in my life — Chooza Moon. No sooner than I saw you first on the rainy Gangnam street, I went across the event horizon of falling in love with you. Now we have lovely two kids (Natalie Seohee and Sarang), and this is a perfect family that I have long dreamt. I love you.

Contents

List of Tables

List of Figures

Chapter 1

Introduction: The role of compact objects in studying astrophysical outflows

An X-ray Binary (XRB) is a binary system which consists of a compact object (a neutron star or a black hole) and a companion star. In some cases, the companion star is a normal main-sequence star, but it also can be an evolved star or other compact object. As gas is transferred from the companion star, it enters the outer edge of the accretion disk and spirals into the central object, producing vigorous X-ray radiation due to the high temperature in the disk. If the compact object has a surface (*i.e.*, a neutron star), the X-ray will be brightest at the center of the disk, and if it is a black hole, the inner edge of the disk would be cut off at the innermost stable orbit. For example, Cygnus X-1 is the black hole candidate and is the most-studied XRB since its discovery with the first X-ray telescopes in the 1960s (Bowyer et al. 1965). The hard state spectral model of Cygnus X-1 indicates that it has a low temperature disk, in which the inner edge can be close to the innermost stable orbit, $R_{\rm IN} \approx 6\,G\,M/c^2$ (Nowak et al. 2012).

Currently, about 280 XRBs have been discovered in our galaxy [catalogued by Liu et al. (2000, 2001)], and several hundred XRBs have also been discovered in nearby galaxies Liu et al. (2007). It is argued that there are 10^8 stellar mass black holes in the galaxy, which are not observable because of the lack of accretion sources (van den Heuvel 1992). Compact objects are ubiquitous, and the number of detected objects has been sharply growing as satellite telescopes that detect high energy photons have launched (*e.g.* XMM-newton, launched in 1999; Chandra X-ray observatory, launched in 1999; and NuSTAR, launched in 2012).

Some of these systems present non-thermal radio emission (Mirabel & Rodríguez 1999; Gallo et al. 2005). This type of emission is thought to be synchrotron radiation from relativistic electrons in bipolar jets around the compact objects. The formation

of jets is believed to be due to a combination of the following physical ingredients: the spin of the black hole (Penrose 1969; Blandford & Znajek 1977), the existence of strong magnetic field (Hawley & Balbus 2002; McKinney & Gammie 2004), and the rapid rotation of the inner accretion disk (Blandford & Payne 1982). The presence of steady jets indicates that X-ray is low/hard state which is associated with flat/slightly inverted radio-to-mm spectra and persistent radio flux (Gallo 2010). However, many aspects of such relativistic jets are still uncertain: jet composition (*i.e.* electrons & protons, electron-position pairs, or heavy elements), jet speed, and jet power. It has been discussed for decades [*e.g.* Reynolds et al. (1996); Wardle et al. (1998)], but estimating the properties is still challenging.

Direct measurement of the physical properties of jets and compact objects is challenging due to their small size, even though they are located in our galaxy. As an alternative method to infer these properties, astronomers expand their view to the global dynamics of jets interacting with surrounding medium. Sell et al. (2010) have studied the dynamics of Circinus X-1 with Chandra X-ray observation. From the analysis of the shocked shell, which is produced by the collimated jet interacting with nearby cool interstellar medium (ISM), they suggested that the jet power might be estimated to $3 \times 10^{35}\,\mathrm{erg\,s^{-1}} < \mathrm{P_{jet}} < 2 \times 10^{37}\,\mathrm{erg\,s^{-1}}$. Gallo et al. (2005) showed that Cygnus X-1 is surrounded by a large-scale (5 pc in diameter) ring-like structure that appears to be inflated by the radiatively inefficient jets.

The jet-medium interaction also plays a key role in studying active galactic nuclei (AGN) scale jets. The X-ray observations of giant cavities and shock fronts in galaxy clusters provide powerful way to study how this interaction can constrain the properties of AGN jets [McNamara & Nulsen (2007), and references therein]. Forman

et al. (2005) studied the X-ray cavities of M87, produced by the expansion of radio plasma around radio jets, and shock fronts associated with outbursts; and calcualted the mean power driving the shock of $2.4 \times 10^{43}\,\mathrm{ergs\,s^{-1}}$, which is sufficient to quench the cooling flow in M87. McNamara et al. (2005) showed that the energy involved in the shock fronts of enermous cavity systems in MS0735+7421 is $\sim 6 \times 10^{61}$erg, which is enough to quench a cooling flow for several Gyr. O'Sullivan et al. (2011) analyzed X-rays from a hot intragroup medium to examine the interaction between radio galaxy NGC4261 and its environment and argued that the mechanical jet power is $\geq 10^{43}\,\mathrm{ergs\,s^{-1}}$. With the growing interest in observational study of the interactions, development of the theoretical framework is needed to support observations. This motivated me to work on the numerical study of jets interacting with surrounding medium.

XRBs with resolved jets are called as *microquasars*, given the apparent similarities with extragalactic quasars (Mirabel et al. 1992). Both objects have a black hole, an accretion disk heated by viscous dissipation, and collimated jets. Although their scales are different (microquasar: a few $\mathrm{M_\odot}$, quasar: $\sim 10^8\,\mathrm{M_\odot}$)(Mirabel & Rodríguez 1998), the physics of flows in those jets are fundamentally similar (Sams et al. 1996): the jets produced by these objects have remarkably similar morphology, and they typically emit the same flat power-law spectrum. Thus, jets from compact objects are not qualitatively different from jets from supermassive black holes. Heinz & Sunyaev (2003) suggested a *model-independent* scaling relation between the core radio flux and the mass of the black hole that is applicable through any mass scales from XRBs to AGN.

XRBs are crucial for studying jet dynamics because of their proximity, acces-

sible dynamical time scale, and well-known energy source. Many XRBs are detected in our galaxy, approximately within 10 kpc, and their orbital time scales are several days, enabling us to trace dynamical changes of the system in real time. This is a key advantage of XRBs because the typical time scale of large-scale AGN accretion is several thousands of years which is too long to follow any changes of AGN and jets. Moreover, in XRBs, it is well understood that the matter is transferred from the companion star to the compact object. This allows to estimate accretion rates more accurately.

XRBs can be separated into two populations: low-mass XRBs (hereafter LMXBs, where "low mass" refers to the companion star which donates its gas into the accretion disk of the compact object) and high-mass XRBs (hereafter HMXBs). While the LMXBs are relatively old and concentrated near the galactic bulge, HMXBs are young and located near the galactic disk (Grimm et al. 2002; Lutovinov et al. 2008; Revnivtsev et al. 2008). The region in which matter is gravitationally bound to a star is called Roche lobe; if matter crosses the Roche lobe, it becomes gravitationally bound to the compact object. In LMXBs, this is the main mass-transfer mechanism, called Roche lobe overflow (Davidson & Ostriker 1973). In HMXBs, the stellar wind of the companion star is strong; therefore, part of the wind matter can be directly captured into the accreting region. However, regardless of the feeding mechanism, jet production is thought to be common for XRBs in the low/hard state (Fender & Maccarone 2004).

In the thesis, I have studied the dynamical evolution of jets in both LMXBs and HMXBs. The study of LMXBs was extended to investigate bow shock pulsar wind nebulae (PWNe) because of their morphological and dynamical similarity. Both

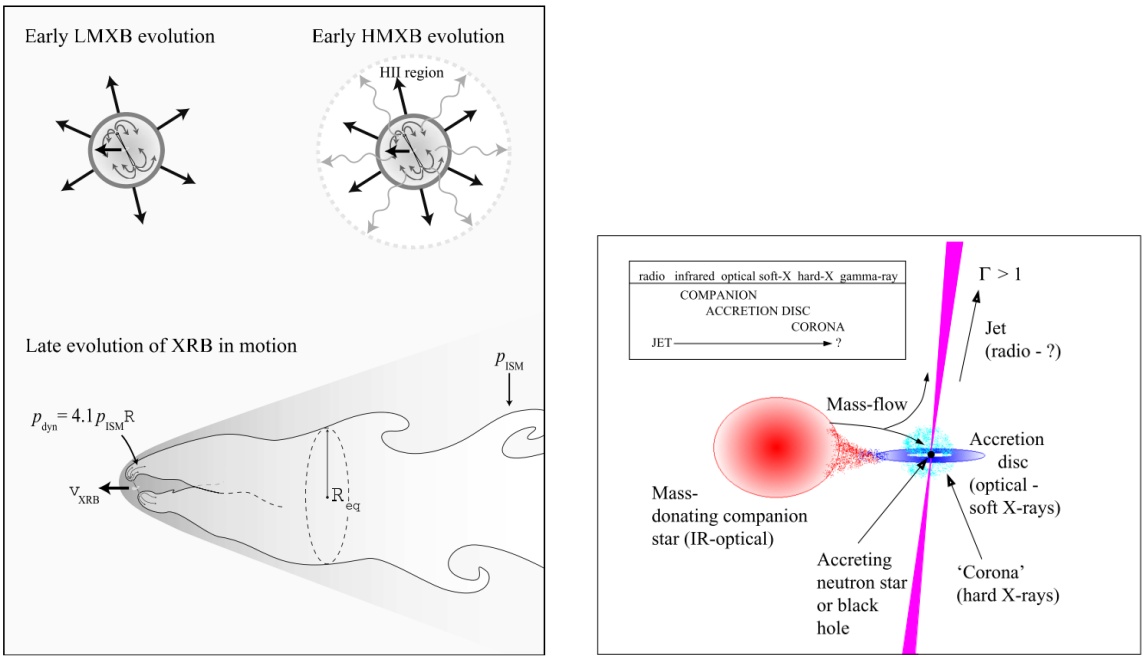

Fig. 1.1. — : Left panel: Sketch of early and late evolutionary phases in LMXBs (Heinz et al. 2008). Right panel: Sketch of physical components in HMXBs (Fender & Maccarone 2004)

pulsar winds in bow shock PWNe and microquasar jets are swept back by ram pressure producing bow shock structures when the objects move through ISM. Although pulsar winds are more isotropic than collimated jets, the global structures are not influenced by the shape of the sources.

To study the dynamical evolution of relativistic outflows from compact objects, I carried out hydrodynamic simulations using the FLASH code (Fryxell et al. 2000), which is a modular, adaptive mesh refinement (AMR) code capable of handling general compressible flow problems. In the block-structured AMR grid, an individual block of cells is refined/de-refined dynamically by certain criteria so that the area of interest can have a higher resolution when it otherwise has a lower one. This is

essential for my work because the dynamic range of simulation domain is substantial. For example, the required cell size to resolve jet nozzle is of the order of 10^9 cm in this work for microquasar jets but the typical length of the steady-state jets is of the order of 10^{13}, implying that it needs over 10^12 cells in the uniform grid in 3-D to obtain the appropriate result. The simulations were carried out mainly by using the department server (184 processors) and a high-performance computer at the university's Advanced Computing Initiative (320 processors for each run). For large scale runs, I used a super-computing system at the Extreme Science and Engineering Discovery Environment, given 10^6 cpu-hours.

In Chapter 2, I present the dynamical evolution of jet trails, and provide observational diagnostics for fast-moving LMXBs. Many LMXBs move with supersonic velocity likely due to being kicked out when they were formed in a supernova explosion. Several microquasars have been detected to move with a velocity of $v_{\rm bh} > 100\,{\rm km\,s^{-1}}$ [*e.g.*, Mirabel et al. (2001)]. Unlike the stationary black hole which produces characteristic cocoons or radio lobes at the end of the jets [1E1740.7-2942 in Mirabel et al. (1993), and perhaps Cygnus X-1 in Stirling et al. (2001)], in a fast-moving black hole, relativistic jets are likely swept backward, generating bow-shock head and trailing streams (See left panel of Figure 4.6). This structure has long been observed in extragalactic analogue, such as narrow/wide angle tails on radio galaxies, called "bent doubles" (Miley et al. 1972; Freeland et al. 2008). My first project focused on the dynamical evolution of global structures in LMXBs, attempting to understand how jets from LMXBs interact with ISM when they have large velocities relative to the ISM. In this work, I proposed a dynamical model of LMXBs and gave constraints on physical properties of the systems.

In Chapter 3, I present the effects of inhomogeneous ambient density on the evolution of bow-shock PWNe. This study was extended from the theoretical model I developed for fast-moving LMXBs. Although the power engine of PWNe is different from that of XRBs, the global features are the same in those fast-moving objects. A pulsar is a fast-spinning neutron star that launches a highly relativistic magnetized wind from its spin-down energy. Many pulsars have supersonic motion with a velocity over several 100s $\mathrm{km\,s^{-1}}$ (Lorimer 1998; Arzoumanian et al. 2002; Faucher-Giguère & Kaspi 2006) due to the natal kick (Sagert & Schaffner-Bielich 2008; Hanke et al. 2012). The Guitar nebula (named for its guitar-like shape) is one of such bow-shock PWNe, and it has a prominent bow-shock head, trailing neck and multiple bubbles (Chatterjee & Cordes 2002). The origin of the bubbles is not clear. I proposed that if a pulsar run through inhomogeneous density medium, it likely produces multiple bubbles; and tested with hydrodynamic simulations.

In Chapter 4, as a series of XRBs studies, I present a theoretical approach of jet evolution in HMXBs. In HMXBs, the presence of a companion star is crucial, because the star generates a strong stellar wind with a substantial mass loss rate, $\dot{M} \sim 10^{-7} - 10^{-5}\,\mathrm{M_\odot\,yr^{-1}}$ (Fender & Maccarone 2004). Such a strong stellar wind likely affects nearby jets, bending or disrupting the jets (See right panel of Figure 4.6). I developed a theoretical framework on the jet-wind interaction model and applied it to observationally resolved jets for Cygnus X-1 and Cygnus X-3, constraining the minimum jet kinetic power.

In Chapter 5, I summarize the conclusions of my thesis and briefly discuss future work.

References

Arzoumanian, Z., Chernoff, D. F., & Cordes, J. M. 2002, ApJ, 568, 289

Blandford, R. D., & Payne, D. G. 1982, MNRAS, 199, 883

Blandford, R. D., & Znajek, R. L. 1977, MNRAS, 179, 433

Bowyer, S., Byram, E. T., Chubb, T. A., & Friedman, H. 1965, Science, 147, 394

Chatterjee, S., & Cordes, J. M. 2002, ApJ, 575, 407

Davidson, K., & Ostriker, J. P. 1973, ApJ, 179, 585

Faucher-Giguère, C.-A., & Kaspi, V. M. 2006, ApJ, 643, 332

Fender, R., & Maccarone, T. 2004, in Astrophysics and Space Science Library, Vol. 304, Cosmic Gamma-Ray Sources, ed. K. S. Cheng & G. E. Romero, 205

Forman, W., Nulsen, P., Heinz, S., et al. 2005, ApJ, 635, 894

Freeland, E., Cardoso, R. F., & Wilcots, E. 2008, ApJ, 685, 858

Fryxell, B., Olson, K., Ricker, P., et al. 2000, ApJS, 131, 273

Gallo, E. 2010, in Lecture Notes in Physics, Berlin Springer Verlag, Vol. 794, Lecture Notes in Physics, Berlin Springer Verlag, ed. T. Belloni, 85

Gallo, E., Fender, R., Kaiser, C., et al. 2005, Nature, 436, 819

Grimm, H.-J., Gilfanov, M., & Sunyaev, R. 2002, A&A, 391, 923

Hanke, F., Marek, A., Müller, B., & Janka, H.-T. 2012, ApJ, 755, 138

Hawley, J. F., & Balbus, S. A. 2002, ApJ, 573, 738

Heinz, S., Grimm, H. J., Sunyaev, R. A., & Fender, R. P. 2008, ApJ, 686, 1145

Heinz, S., & Sunyaev, R. A. 2003, MNRAS, 343, L59

Liu, Q. Z., van Paradijs, J., & van den Heuvel, E. P. J. 2000, A&AS, 147, 25

—. 2001, A&A, 368, 1021

—. 2007, A&A, 469, 807

Lorimer, D. R. 1998, Advances in Space Research, 21, 177

Lutovinov, A., Revnivtsev, M., Gilfanov, M., & Sunyaev, R. 2008, ArXiv e-prints, arXiv:0801.3589

McKinney, J. C., & Gammie, C. F. 2004, ApJ, 611, 977

McNamara, B. R., & Nulsen, P. E. J. 2007, ARA&A, 45, 117

McNamara, B. R., Nulsen, P. E. J., Wise, M. W., et al. 2005, Nature, 433, 45

Miley, G. K., Perola, G. C., van der Kruit, P. C., & van der Laan, H. 1972, Nature, 237, 269

Mirabel, I. F., Dhawan, V., Mignani, R. P., Rodrigues, I., & Guglielmetti, F. 2001, Nature, 413, 139

Mirabel, I. F., & Rodríguez, L. F. 1998, Nature, 392, 673

—. 1999, ARA&A, 37, 409

Mirabel, I. F., Rodriguez, L. F., Cordier, B., Paul, J., & Lebrun, F. 1992, Nature, 358, 215

—. 1993, A&AS, 97, 193

Nowak, M. A., Wilms, J., Hanke, M., Pottschmidt, K., & Markoff, S. 2012, Mem. Soc. Astron. Italiana, 83, 202

O'Sullivan, E., Worrall, D. M., Birkinshaw, M., et al. 2011, MNRAS, 416, 2916

Penrose, R. 1969, Nuovo Cimento Rivista Serie, 1, 252

Revnivtsev, M., Lutovinov, A., Churazov, E., et al. 2008, A&A, 491, 209

Reynolds, C. S., Fabian, A. C., Celotti, A., & Rees, M. J. 1996, MNRAS, 283, 873

Sagert, I., & Schaffner-Bielich, J. 2008, A&A, 489, 281

Sams, B. J., Eckart, A., & Sunyaev, R. 1996, Nature, 382, 47

Sell, P. H., Heinz, S., Calvelo, D. E., et al. 2010, ApJ, 719, L194

Stirling, A. M., Spencer, R. E., de la Force, C. J., et al. 2001, MNRAS, 327, 1273

van den Heuvel, E. P. J. 1992, Endpoints of stellar evolution: The incidence of stellar mass black holes in the galaxy, Tech. rep.

Wardle, J. F. C., Homan, D. C., Ojha, R., & Roberts, D. H. 1998, Nature, 395, 457

Chapter 2

Jet trails and Mach cones: The interaction of microquasars with the ISM

This chapter has previously appeared in The Astrophysical Journal

D. Yoon, B. Morsony, S. Heinz, K. Wiersema, R. P. Fender, D. M. Russell, & R. Sunyaev, 2011, vol. 742, p. 25

Abstract

A sub-set of microquasars exhibit high peculiar velocity with respect to the local standard of rest due to the kicks they receive when being born in supernovae. The interaction between the radio plasma released by microquasar jets from such high-velocity binaries with the ISM must lead to the production of trails and bow shocks similar to what is observed in narrow-angle tailed radio galaxies and pulsar wind nebulae. We present a set of numerical simulations of this interaction that illuminate the long term dynamical evolution and the observational properties of these microquasar bow shock nebulae and trails. We find that this interaction always produces a structure that consists of a bow shock, a trailing neck, and an expanding bubble. Using our simulations to model emission, we predict that the shock surrounding the bubble and the neck should be visible in H_α emission, the interior of the bubble should be visible in synchrotron radio emission, and only the bow shock is likely to be detectable in X-ray emission. We construct an analytic model for the evolution of the neck and bubble shape and compare this model with observations of X-ray binary SAX J1712.6-3739.

2.1 Introduction

It is now well established that accretion onto black holes can lead to the production of powerful jets, both in the case of AGN, in which case we call the object a radio galaxy, and in the case of X-ray binaries (XRBs), in which case we call the object a microquasar. We have since learned that even neutron star X-ray binaries as well as some accreting white dwarfs behave in the same way (Fender et al. 2004; Migliari & Fender 2006; Tudose et al. 2009; Körding et al. 2008).

When powerful jets run into their environment, they produce bright external shocks (called hot spots or working surfaces) and generally inflate pockets of relativistic plasma that emit diffuse synchrotron emission. If the black hole is stationary, these pockets take on roughly ellipsoidal shapes and are called radio lobes or cocoons. They are surrounded by the interstellar or intergalactic gas that was occupying the volume prior to inflation, compressed into a narrow shell. This picture is most easily observed in the case of X-ray cavities in galaxy clusters inflated by AGN jets (Rafferty et al. 2006, and references therein), but has also been discovered around a few microquasars (Gallo et al. 2005; Hao & Zhang 2009).

However, when the black hole is moving at appreciable speed with respect to its environment, the ram pressure of the headwind can dramatically alter the dynamics of the outflowing radio plasma, sweeping it back and generating a bow shock ahead of the moving black hole. This has long been known in the case of radio galaxies (e.g. Miley et al. 1972), which, depending on the angle at which the plasma is bent back, are called narrow or wide angle tail sources (generically, these sources are also

called "bent doubles").

Given that the black holes at the core of microquasars are born in supernova explosions, and given that supernovae can impose significant kick velocities on the compact objects they produce, Heinz et al. (2008) suggested that a similar phenomenon to "bent doubles" should occur around a sub-population of microquasars: the high-velocity tail of the population of low-mass X-ray binaries (LMXBs). It is now known that several microquasars are moving through the ISM at relative velocities in excess of $v_{\rm ext} > 100$ km s^{-1} (Mirabel et al. 2001).

The phenomenology of these trailed microquasars should be broadly similar to their supermassive AGN equivalent, leading to the production of a low-surface brightness trail of synchrotron emitting relativistic plasma, and a brighter bow shock nebula. While the mode of inflation is fundamentally different, the end product should also be very similar to pulsar wind bow-shock nebulae that are formed by interaction between strong wind from pulsars with significant kick velocities in the interstellar medium. The general bow shock features have been well observed in H_α emission for PSR B1957+20 (Stappers et al. 2003), PSR B0740-28 (Stappers et al. 2002), PSR J0437-4715 (Bell et al. 1995), and PSR B2224+65 (the "guitar" nebula) (Chatterjee & Cordes 2002). Also, G359.23-0.82 which is powered by PSR J1747-2958 shows bright head and X-ray & radio "trails" (Gaensler et al. 2004).

The first candidate of a bow shock around such a trailed source, the LMXB SAX J1712.6-3739 , was discovered in an H_α image by Wiersema et al. (2009, originally found by in 't Zand et al. 1999). It is broadly consistent with the predictions of Heinz et al. (2008). Future searches for large scale nebula and diffuse synchrotron emission around known LMXBs are needed to further test the predicted existence of

this population of sources.

The model developed in Heinz et al. (2008) was purely analytic and a number of important aspects of the evolution of such trailed microquasars was left open. Numerical simulations are needed to investigate the production of these sources in more detail and to confirm the qualitative predictions of Heinz et al. (2008).

In this paper, we model the evolution of the XRBs moving through the ISM by using 3-dimensional hydrodynamic simulations and to derive a more detailed dynamical model for the large scale evolution of these sources.

A key aim of this study is to develop quantitative diagnostics that can be used to derive important constraints on the core parameters of microquasars from observations of trailed microquasars, such as their age, their relative velocity with respect to the local standard of rest ($v_{\rm XRB}$), and the jet power from observational parameters like the opening angle of the bow shocks, the size of the hot bubble at the terminus of the trail, and the brightness of the shock, trail, and bubble. In addition, our simulation results can be used to predict the brightness of H_α, bremsstrahlung, X-ray, and radio synchrotron emission and to design targeted observational searches for these sources.

This paper is organized as follows: In §2, we present the numerical method and the initial conditions for our numerical study. In §3, we discuss the evolution of XRBs, scaling relations, and observational expectations. In §4, we compare our results with new observations of the LMXB SAX J1712.6-3739. Finally, in §5 we summarize our results.

2.2 Technical Description

2.2.1 The code

Simulations are carried out in 3 dimensions with the FLASH 2.4 hydrodynamic code (Fryxell et al. 2000), which is a modular, adaptive mesh refinement code. It solves the Riemann problem using the piecewise-parabolic method. The code is formally accurate to second order. The gas is modeled with either an adiabatic equation of state with index γ=5/3 or with radiative line cooling. Radiative cooling from an optically thin plasma is implemented in FLASH adopting a piecewise-power law approximation that evaluates a plausible fit to $\Lambda(T)$ within the temperature range of $4.4 \times 10^3 < T < 10^8$K

2.2.2 The jet nozzle

In order to simulate the injection of collimated, supersonic jets into the grid, we employ a numerical "nozzle", as first developed and described in (Heinz et al. 2006): An internal inflow boundary of cylindrical shape placed at the location of the XRB, injecting fluid with prescribed energy, mass, and momentum flux to match the parameters we chose for the jet.

For reasons of numerical stability, we impose a slow lateral outflow with low mass flux in order to avoid complete evacuation of zones immediately adjacent to the nozzle due to the large velocity divergence at the nozzle. The injection of energy and mass due to this correction is negligible.

We generally follow the prescription for jet injection used in previous simulations of AGN jets described in (Heinz et al. 2006), but keep the location of the XRB fixed in space, instead letting the external medium stream by at velocity $-v_{\rm ext}$.

Unlike our AGN simulations, we do not impose a random jitter on the jet axis in this case.

We chose to inject the jet at an internal Mach number of 10. While our adiabatic simulations are strictly scale free, we picked a set of fiducial dimensions for our box that lead to the following natural scaling: For computational feasibility, we chose a jet velocity of $v_{\rm jet} = 3 \times 10^9\,{\rm cm\,s^{-1}}$. The jet is turned on initially and continues to inject material for the entire length of the simulation.

The simulations were carried out with Adaptive Mesh Refinement in order to capture the large dynamic range required, ensuring that the nozzle is resolved with at least 8 cells across. For our fiducial scaling, the maximum resolution for the standard model is about 0.156 pc near the jet nozzle.

Based on the estimated power of the jet in Cyg X-1 from Gallo et al. (2005), the jet power in our simulation is set to a constant value of $W_{\rm jet} = 10^{37}$ ergs s^{-1} in our fiducial scaling. Note that since the Cyg X-1 is known to be one of the most powerful XRB sources, sustaining the hard X-ray state for about 90% of the time. The jets in our model might be more powerful than those of typical LMXBs. However, with the exception of our simulations with cooling, our simulations are scale free and can thus be adjusted easily to other parameter combinations.

2.2.3 Initial conditions

We placed the XRB in a moving medium inside a box large enough that boundary conditions never influence the dynamics. We varied the velocity of the gas relative to the XRB to be $v_{\rm XRB} = 30$ km s^{-1}, 100 km s^{-1} and 300 km s^{-1} (see Table 3.1). The lowest velocity case represents a typical LMXB, given that the LMXB velocity dispersion is $37\,{\rm km\,s^{-1}}$, while the largest represents the most extreme case plausible

(a marginally unbound source). The simulations we ran for this study are listed in Tab. 3.1.

The fiducial ISM pressure we use is $P_0 = 3 \times 10^{-12}$ ergs cm^{-3} following Cox (2005), and we use an ISM number density of $n_{\rm ISM} = 1$ cm^{-3}, giving a sound speed in the ISM of $c_s = 17.3$ km s^{-1}.

Typically, simulations were carried out to 1 Myr in our fiducial scaling (much longer than the dynamical evolution of the jet, and long enough for the quasi-steady state of the bow shock and the self-similar solution we will discuss below to be established).

Table 3.1 also includes one case with our standard parameters and radiative cooling (with $v_{\rm XRB} = 300$ km s^{-1}), the hvc case. We used this run to verify that the morphology of our simulations are not strongly affected by cooling and to properly model emission (see §3.3). A further 3 simulations with cooling, fit1, fit2 and fit3, were carried out to attempt to match H$_\alpha$ observations of SAX J1712.6-3739 (see §4.1)

Because of the self-similar nature of the flow, the simulations lend themselves to a staggered refinement scheme. As we will describe below, the radio plasma forms of a large scale bubble and a neck connecting the XRB to this bubble. We can

Table 2.1. : Parameter of the Simulations

Name	$v_{\rm XRB}$	Maximum Resolution	Luminosity	Radiative Cooling
lv	30 km s^{-1}	0.312 pc	10^{37} erg/s	no
mv	100 km s^{-1}	0.156 pc	10^{37} erg/s	no
hv	300 km s^{-1}	0.156 pc	10^{37} erg/s	no
hvc	300 km s^{-1}	0.156 pc	10^{37} erg/s	yes
fit1	100 km s^{-1}	0.039 pc	8.47×10^{33} erg/s	yes
fit2	200 km s^{-1}	0.039 pc	8.47×10^{33} erg/s	yes
fit3	300 km s^{-1}	0.039 pc	2.29×10^{35} erg/s	yes

therefore de-refine the simulation on cylinders on increasing radius around the axis of propagation of the XRB and again de-refine with increasing distance from the XRB along the axis of propagation. We decrease the refinement by a factor of two for every power of two increase in radius and distance.

2.3 Results

2.3.1 Morphological Evolution

Heinz et al. (2008) presented a simple, analytic model for the long term dynamical evolution of trailed microquasars. Our simulations allow us to move beyond the initial heuristic model and describe the dynamics of microquasar driven bow shock nebulae in detail.

The initial evolution of the system follows the prediction of Heinz et al. (2008) almost exactly: The jets inflate a single large, roughly spherical bubble that expands following the self-similar solution for a continuously driven bubble by Castor et al. (1975), surrounded by a thin shell of swept-up ISM.

Initially, the expansion velocity of the bubble is much faster than the space velocity of the XRB, v_{XRB}, implying that the XRB remains roughly at the bubble's center. As the expansion slows down, the XRB begins moving towards the shell and eventually breaks out of the expanding bubble.

At this point, the dynamic pressure of the ISM due to the XRB's velocity causes the jets to bend backwards, and a trail of radio plasma is created behind the XRB, connecting it to the bubble. The backflow of the ejected material from the jets is similar to that seen in the model of case 3 in Bosch-Ramon et al. (2011). The radio plasma released by the XRB continues to inflate the bubble, akin to a balloon

inflated by a straw. The bubble, therefore, continues to expand spherically even though the binary can be far outside the bubble.

As it propagates, the XRB is driving a bow shock into the ISM. As predicted in Heinz et al. (2008), dynamical instabilities develop at the contact discontinuity between the bow shocked ISM and the backflow along the radio trail, dissipating some of the backflow energy along the channel.

The dynamical evolution described above is shown in Fig. 2.1 as a time sequence of density slices through the center of the simulation box. Relativistic, axisymmetric simulations of a pulsar wind nebula in Bernstein & Hughes (2009) created a similar structure with a bow shock connected to an expanding bubble. This indicates that, away from the jet or wind source, the evolution of XRBs and pulsar nebulae are nearly identical, except for the scale.

2.3.2 Scaling relations

Based on the observed evolution of the trail and bubble, we can construct a simple analytic model for the inflation of bow shock nebulae by microquasars (and, by extension, pulsar wind bow shock nebulae) that can be tested directly against the simulations. This will allow us to formulate analytic expressions for observables.

The jets initially inflate a nearly spherical cavity that evolves as a wind driven bubble (Castor et al. 1975). The bubble expands as

$$R_b(t) = C_1^{1/5} \left(\frac{L}{\rho_0}\right)^{1/5} t^{3/5} \tag{2.1}$$

where L is the source luminosity, ρ_0 is the ISM density and C_1 is a constant that equals $\frac{25}{14\pi}$ for an adiabatic index of $\Gamma = 5/3$. In terms of the fiducial parameters for our simulations, this is

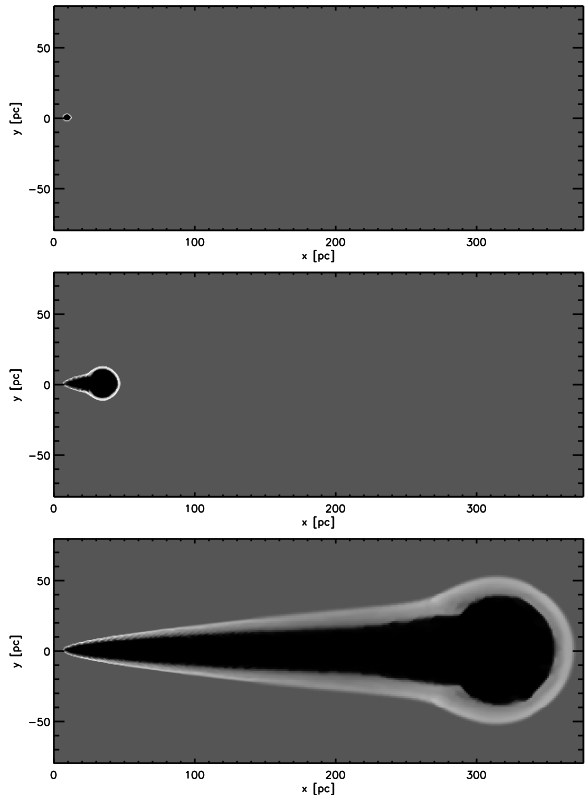

Fig. 2.1. — : Density slice through our 300 km s^{-1} simulation at 10,000 years (top), 100,000 years (middle) and 1 Myr (bottom). The XRB is located toward the left of the images. At 10,000 years (top) the XRB is surrounded by a spherical bubble, although the XRB is nearing the left edge. At 100,000 years (middle), the XRB has broken out of the bubble and created a distinctive shape. The jets, directed up and down, are curved back at the bow shock (curved shock at left) and directed back to the large bubble to the right, where they terminate and power the bubble expansion. A neck connects the binary and bubble, and is surrounded by an oblique shock. At 1 Myr (bottom), the *shape* is similar to that at 100,000 years, except that the neck is more elongated, with a smaller opening angle.

$$R_b(t) = 13.1 \text{ parsec} \left(\frac{L_{37}}{\rho_{0H}}\right)^{1/5} t_5^{3/5} \tag{2.2}$$

where $L_{37} = \frac{L}{10^{37} \text{ erg s}^{-1}}$, $\rho_{0H} = \frac{\rho_0}{1.67\times10^{-24} \text{ g cm}^{-3}}$, and $t_5 = \frac{t}{100{,}000 \text{ years}}$. The expansion velocity of the bubble is

$$v_b(t) = \tfrac{3}{5} C_1^{1/5} \left(\frac{L}{\rho_0}\right)^{1/5} t^{-2/5} = 76.7 \text{ km s}^{-1} \left(\frac{L_{37}}{\rho_{0H}}\right)^{1/5} t_5^{-2/5} \tag{2.3}$$

and the pressure inside the bubble is

$$P_b(t) = P_0 \left(\tfrac{5}{4} M_b^2 - \tfrac{1}{4}\right) \tag{2.4}$$

where $M_b = \frac{v_b}{\sqrt{\gamma P_0/\rho_0}}$ is the Mach number of the spherical shock and P_0 is the ISM pressure. Assuming at least a moderately strong shock, the pressure goes to

$$P_b(t) \approx \tfrac{5}{4} P_0 M_b^2 \approx \tfrac{27}{100} C_1^{2/5} L^{2/5} \rho_0^{3/5} t^{-4/5} \approx 8.25 \times 10^{-11} \text{ erg cm}^{-3} L_{37}^{2/5} \rho_{0H}^{3/5} t_5^{-4/5} \tag{2.5}$$

Initially, the expansion of this bubble is faster than the velocity of the XRB. However, as the expansion of the bubble slows while the velocity of the source remains constant, the source eventually breaks out of the bubble at a time t_{break}. The breakout time scales with source velocity v_s as

$$\begin{aligned} t_{\text{break}} &= C_1^{1/2} \left(\frac{L}{\rho_0}\right)^{1/2} v_s^{-5/2} \\ &= 185{,}000 \text{ years} \left(\frac{L_{37}}{\rho_{0H}}\right)^{1/2} \left(\frac{v_s}{100 \text{ km s}^{-1}}\right)^{-5/2} \end{aligned} \tag{2.6}$$

The radius of the bubble at the breakout time therefore scales as

$$R_{break} = C_1^{1/5} \left(\frac{L}{\rho_0}\right)^{1/5} t_{\text{break}}^{3/5} = C_1^{1/2} \left(\frac{L}{\rho_0}\right)^{1/2} v_s^{-3/2} = 18.9 \text{ parsec} \left(\frac{L_{37}}{\rho_{0H}}\right)^{1/2} \left(\frac{v_s}{100 \text{ km s}^{-1}}\right)^{-3/2} \tag{2.7}$$

After breakout, the source continues to power bubble expansion. A bow shock develops in front of the source which bends the jets back in the opposite direction of the source motion. A low-density channel remains which connects the source to the bubble. Jet material flows back through this channel, adding energy to the interior of the expanding bubble. So long as the volume of this channel remains small compared to the volume of the bubble, the expansion rate of the bubble continues to be described by eqn. 2.1, the self-similar equation of a continuously powered bubble.

As seen in Fig. 2.1, the resulting shape is an expanding spherical bubble connected to the source by a thin neck. The neck consists of a shock surrounding a narrow cavity filled with jet material. At any point x along the neck, the shape is described by w_1, the width of the inner cavity, and w_2, the distance from the mid plane to the outer edge of the shock. In the frame of the binary, the cavity has a fixed shape and is in pressure balance with the surrounding shocked material. The flow of material can therefore be described using an adiabatic equation of state, the Bernoulli equation and mass continuity:

$$P_x = a\rho_x^{\gamma} \tag{2.8}$$

$$\tfrac{1}{2}v_x^2 + \frac{\gamma}{(\gamma-1)}\frac{P_x}{\rho_x} = b \tag{2.9}$$

$$\rho_x v_x w_1^2 = c \tag{2.10}$$

where v_x, ρ_x and P_x are the velocity, density and pressure of material in the cavity at position x, γ, the adiabatic index, is 5/3, and a, b and c are constants. In term of a, and with $\gamma = 5/3$, $b = a^{3/5}(\rho_0 v_s^2)^{2/5}$ and $c = L\, a^{-3/5}(\rho_0 v_s^2)^{-2/5}$.

Rearranging eqns. 2.8 to 2.10 we solve for w_1 and find that

$$w_1 = \left(\frac{ca^{3/5}}{\sqrt{2a^{3/5}}}\right) \frac{1}{\left[(\rho_0 v_s^2)^{2/5} P_x^{6/5} - \frac{5}{2} P_x^{8/5}\right]^{1/4}} \tag{2.11}$$

Making the approximation $P_x \ll \rho_0 v_s^2$ (i.e., the source velocity is supersonic), this reduces to

$$w_1 = 5^{-1/4} 2^{1/2} L^{1/2} a^{3/10} (\rho_0 v_s^2)^{-3/10} P_x^{-3/10} = C_2 P_x^{-3/10} \tag{2.12}$$

The pressure will be set by the jump conditions for an oblique shock, with θ and β the angle with respect to the direction of motion of the inner and outer edges of the shock, respectively:

$$\tan(\theta) = \frac{M_0^2 \sin^2\beta - 1}{\tan\beta(1 + \frac{(\gamma+1)}{2} M_0^2 - M_0^2 \sin^2\beta)} \tag{2.13}$$

$$\frac{P_x}{P_0} = \frac{2\gamma M_0^2 \sin^2\beta - (\gamma - 1)}{(\gamma + 1)} \tag{2.14}$$

where $M_0 = v_s/\sqrt{\gamma P_0/\rho_0}$ is the Mach number of the binary relative to the ISM, $\tan\theta = dw_1/dx$ and $\tan\beta = dw_2/dx$. Making the approximation that θ and β are small, this reduces to

$$\theta = \frac{M_0^2\beta^2 - 1}{\frac{4}{3}\beta M_0^2} \tag{2.15}$$

$$P_x = P_0(\tfrac{5}{4} M_0^2 \beta^2 - \tfrac{1}{4}) \tag{2.16}$$

$$\beta = \sqrt{\frac{4\frac{(w_1/C_2)^{-10/3}}{P_0} + 1}{5M_0^2}} \tag{2.17}$$

Substituting we find

$$\theta = \frac{dw_1}{dx} = \frac{3(C_2^{10/3} - P_0 w_1^{10/3})}{M_0 P_0 w_1^{10/3}} \left(\frac{20 C_2^{10/3}}{P_0 w_1^{10/3}} + 5 \right)^{1/2} \tag{2.18}$$

This differential equation can then be integrated numerically to find $w_1(x)$ and this in turn can be used to find $w_2(x)$.

As the pressure drops along the neck, however, it eventually reaches a minimum value equal to the pressure in the expanding bubble. Beyond this point, the angle of the shock is constant such that the post-shock pressure is equal to the P_b, the pressure in the bubble, which is set by the expansion rate of the bubble v_b. The incoming velocity towards the shock will be $v_s - v_b$, because the bubble is expanding towards the source, giving a minimum shock angle of

$$\beta = \frac{v_b}{v_s - v_b} = \frac{dw_2}{dx} \tag{2.19}$$

The angle of the inner surface is then approximately

$$\theta = \frac{M_2^2 \beta^2 - 1}{\frac{4}{3} M_2^2 \beta} = \frac{dw_1}{dx} \tag{2.20}$$

where $M_2 = (v_s - v_b)/\sqrt{\gamma P_0/\rho_0}$ is the Mach number of the shock. In our simulations, this asymptotic limit dominates and the shape described by eqn. 2.18 only describes a small region near the jet source. Note that the width of the neck where it reaches the minimum value of β is described by eqn. 2.12 with $P_x = P_b$, giving $w_1(P_b) = C_2 P_b^{-3/10}$. This equation depends on the normalization constant a in the adiabatic equation (eqn. 2.8), which in practice depends on the amount of mixing between jet and ISM material. The width at this point also depends on the radius of curvature

of the bow shock, which is not taken into account in this analytic model Therefore, we use a as a free parameter to get the proper fit for the width of the neck where the minimum value of β is reached.

Figure 2.2 shows density slices of the 300 km s^{-1}, 100 km s^{-1} and 30 km s^{-1} simulations (models hv, mv and lv) at 1 Myr. The white lines are results of our analytic model for the bubble size, $w_1(x)$ and $w_2(x)$. In the first two cases, the predicted shape of the inner and outer edge of the neck are a good fit to the simulations. In the 30 km s^{-1} case, the XRB is still inside the spherical bubble at 1 Myr.

The outer shock angle β decreases with time as the pressure in the bubble and the expansion velocity drop. The width of the neck where it meets the bubble is approximately

$$w_{2,meet} = \beta(v_s t - R_b) + w_1(P_b) \tag{2.21}$$

$$w_{2,meet} = \frac{v_b}{v_s - v_b}\left(v_s t - \tfrac{5}{3} v_b t\right) + C_2\left(\tfrac{5}{4} P_0 M_b^2\right)^{-3/10} \tag{2.22}$$

Asymptotically, this width goes to $w_{2,meet} = \beta v_s t = v_b t = \frac{3}{5} R_b$. Therefore, the ratio of the bubble radius to the neck width approaches a constant ratio of 3/5, and the width of the neck is always smaller than the radius of the bubble.

The volume of the neck scales asymptotically as

$$V_{\rm neck} = \tfrac{1}{3}\pi v_s t \left(\tfrac{3}{5} R_b\right)^2 = \tfrac{1}{5}\pi C_1^{2/5} v_s \left(\frac{L}{\rho_0}\right)^{2/5} t^{11/5} = 3.23 \times 10^{58}\ {\rm cm}^3 \left(\tfrac{v_s}{100\ {\rm km\ s^{-1}}}\right) \left(\frac{L_{37}}{\rho_{0H}}\right)^{2/5} t_5^{11/5} \tag{2.23}$$

while the volume of the bubble scales as

$$V_{bub} = \tfrac{4}{3}\pi R_b^3 = \tfrac{4}{3}\pi C_1^{3/5} \left(\tfrac{L}{\rho_0}\right)^{3/5} t^{9/5} = 2.75 \times 10^{59}\ \mathrm{cm}^3 \left(\tfrac{L_{37}}{\rho_{0H}}\right)^{3/5} t_5^{9/5} \tag{2.24}$$

the ratio of the volumes is therefore

$$\frac{V_{\rm neck}}{V_{bub}} = \frac{9}{100}\frac{v_s t}{R_b} = \frac{3}{20} C_1^{-1/5} v_s \left(\frac{L}{\rho_0}\right)^{-1/5} t^{2/5} = 0.117 \left(\frac{v_s}{100\ \mathrm{km\ s^{-1}}}\right) \left(\frac{L_{37}}{\rho_{0H}}\right)^{-1/5} t_5^{2/5} \tag{2.25}$$

The volume of the neck and bubble will eventually become equal when the length of the neck ($v_s t$) is about 11.1 times the bubble radius. The width of the shock where it meets the bubble is about $w_{2,meet} = \frac{3}{5} R_b$, so the angle when the volumes are equal is $\beta = 27/500 = 0.054$ However, the angle of the shock around the neck cannot be less that $\beta \simeq 1/M_0$, so the volumes become equal before the shock becomes weak only if $M_0 \geq 18.5$. Our assumption that the volume of the neck is small will hold until bubble expansion starts to become marginally sonic, unless the source has a very high Mach number relative to its surroundings.

While our simulations have not run long enough to probe the sub-sonic regime of bubble expansion, it is worth speculating about the late state evolution of trails and bubbles. Given that the bounding pressure of the bubble will be dominated by the internal pressure of the ISM, the expansion velocity of the bubble will drop below the self-similar value for an energy driven bubble (with $R \propto t^{1/3}$). In addition, the ISM will no longer be strongly compressed into a narrow shell. Since the neck and bow shock will maintain their stationary shape, one should expect that the late state evolution of a bow-shock/trail nebula will eventually lose the terminating bubble and the trail pressure will eventually approach the ISM pressure, consistent with the late state structure of the trail proposed in Heinz et al. (2008).

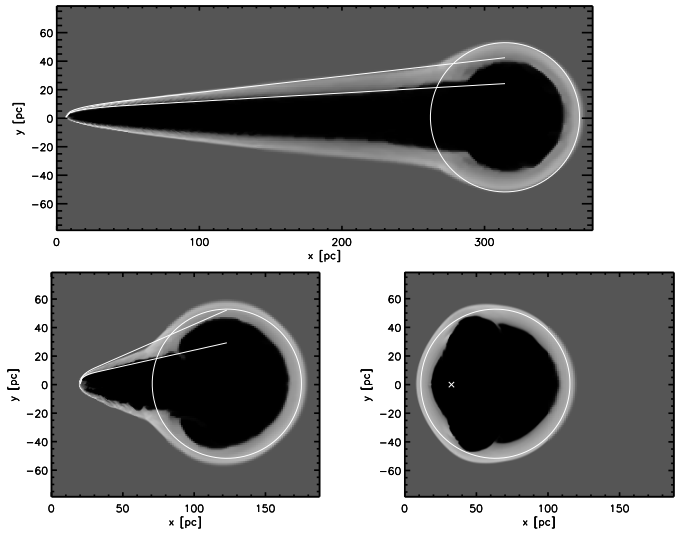

Fig. 2.2. — : Density slice of 300 km s^{-1} (upper), 100 km s^{-1} (lower left) and 30 km s^{-1} (lower right) simulations at 1 Myr. The white curves trace the analytic solution for w_1 and w_2, the neck shape, and the circle is the size of the bubble from eqn. 2.1. Values of a used to fit the bow shock width are 10^{31} for the 300 km s^{-1} simulations and 10^{33} for the 100 km s^{-1} simulation. In the 30 km s^{-1} simulation the XRB (marked with an $\times$) is still inside the bubble, but significantly offset from the center.

2.3.3 Observable properties of microquasar bow shock nebulae and trails

2.3.3.1 H_alpha emission

For XRBs moving supersonically through cold or warm ISM, the compressed, hot gas in the bow shock will produce collisionally excited line emission, most importantly H_α (as well as the classic spectrum of nebular lines like [OIII]). In fact, Wiersema et al. (2009) detected the nebula of SAX J1712.6-3739 in H_α. Our models

support the jet-ISM interaction scenario (Heinz et al. 2008) and the numerical simulations show an apparent quantitative agreement with the observed results for H_α emission.

To calculate the H_α emission, we first determine the ionization balance in the shocked gas, using the MAPPINGS III code (Sutherland & Dopita 1993); the code uses a time-dependent algorithm for accurate equilibrium balance calculation. The typical temperature of the shocked shell is estimated to be around $10^5 - 10^6$ K in the adiabatic case, hence the gas is inferred to be nearly fully ionized at the shocked region. Figure 2.3 (bottom left panel) shows the surface brightness in H_α for the model hv. Note that all simulations can be scaled with XRB jet luminosity by reducing the predicted surface brightness, nebula size, and simulation time by a factor of $(L_{37})^{-1/2}$.

The bubble is relatively bright in H_α. The shock around the neck is also visible in H_α in fig. 2.3. A similar feature has been identified with SAX J1712.6-3739 (Wiersema et al. 2009). We discuss the morphological similarity between that source and our simulations in §4.1.

Radiative cooling has little influence on the dynamical evolution of the XRBs. The upper panels of fig. 2.3 reveal that overall morphologies for two models (with and without radiative cooling) are broadly similar. Radiative cooling leads to a significantly thinner shell of shocked material around the bubble and neck, giving the appearance of a slightly narrower neck. Because of the cooling-induced contraction of the gas, the shell also appears to develop some irregularities in shape, though the overall shape of the hot (radio) plasma inside the trail and bubble occupies essentially the same volume.

However, the radiative cooling has a pivotal role for H_α, because of the strong temperature sensitivity of the ionization balance and thus the recombination line emission. This is because the cooling time scale is comparable to the dynamical time scale of XRBs, leading to significantly lower temperatures in the shell than in a purely adiabatic simulations.

The bow shock immediately surrounding the XRB is very dim because the temperature is too high for strong H_α emission. As cooling becomes important down stream, the temperature at the shock quickly drops to the range of a few 10,000 K. As a result, the emission becomes stronger by about a factor of 50.

Because H_α emission depends non-trivially on temperature, it is not straight forward to express brightness predictions semi-analytically. Figure 2.3 is therefore specific to our simulation using fiducial parameters only.

2.3.3.2 Radio emission

Given that the trail itself should be filled by magnetized, relativistic plasma released by the jets, they will emit synchrotron radiation. As the plasma travels along the jet, particles will cool both adiabatically and due to synchrotron losses. As is well known from studies of AGN jets and radio lobes, this introduces a cutoff to the electron energy distribution and to the synchrotron spectrum.

Following, e.g., Heinz & Begelman (1997), the cutoff frequency, as a function of travel time along the trail, will be given by

$$\gamma_{max} \simeq \frac{\left(\frac{P}{P_0}\right)^{1/4}}{\int \frac{4}{3}\sigma_T U_B \left(\frac{P}{P_0}\right)^{1/4} dt}. \tag{2.26}$$

with an associated cutoff frequency of

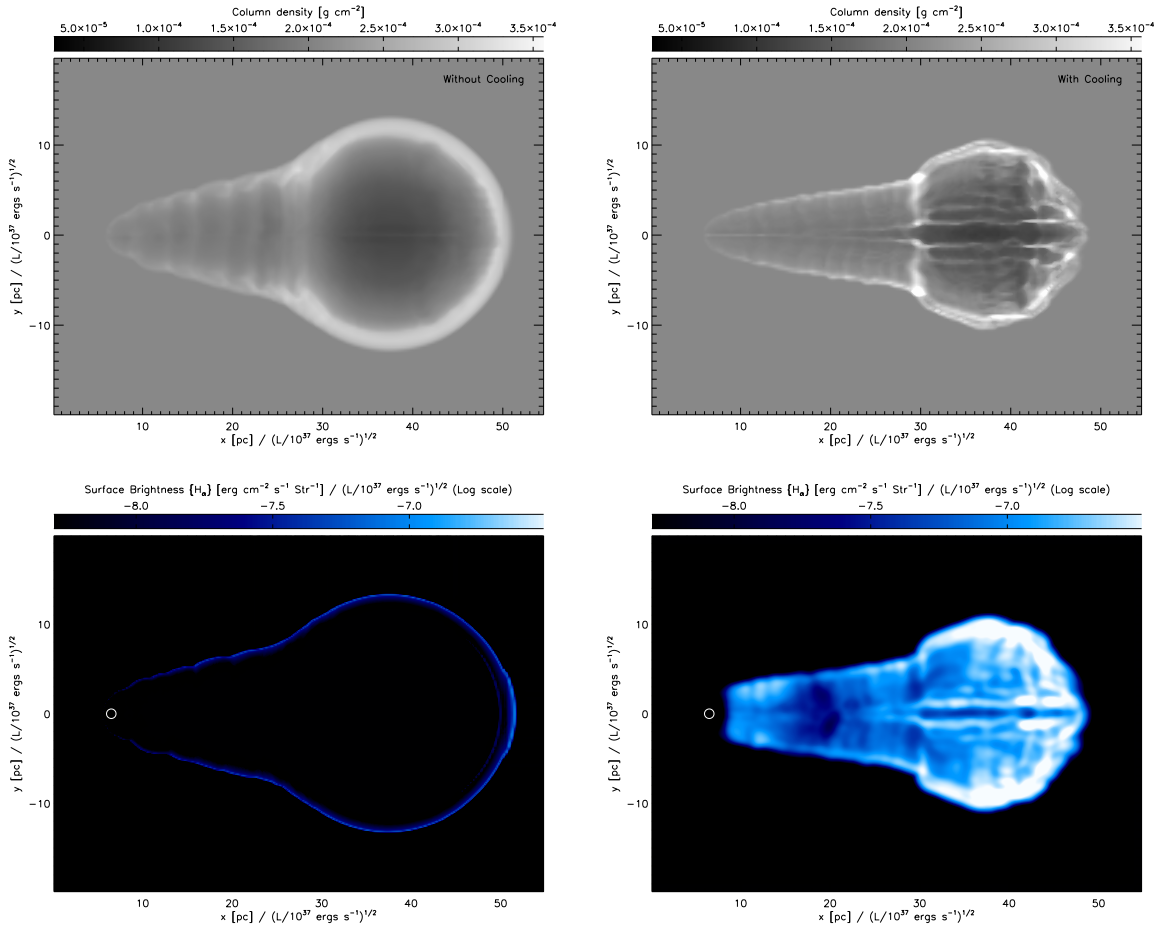

Fig. 2.3. — : The density contour map for the model without the radiative cooling (upper left) and with the radiative cooling (upper right) at 100,000 yr (v_{xrbs} = 300 km s^{-1}). The bottom panels shows H_α emission for each case (log scale). The predicted surface brightness can be scaled to different XRB jet luminosities by reducing the surface brightness, size scale and simulation time by a factor of $L_{37}^{-1/2}$.

$$\nu_{max} \approx \frac{9eB\gamma_{max}^2}{4\pi m_e c^2}, \tag{2.27}$$

Given that the flow through the trail assumes a quasi-steady state behind the XRB, we can simply integrate this equation through single frames to lowest order to derive the cooling frequency as a function of position along the trail. The result is shown in fig. 2.4. For our fiducial parameters, the cooling frequency is estimated to fall within $10^{13} - 10^{15}$ Hz, well above the radio band.

This implies that synchrotron emission should be a good tracer of these trails at all frequencies, not just at low frequencies. This is in contrast to the estimates in Heinz et al. (2008), who suggested that cooling could be important along the trail. The reason for this difference is the significant backflow velocity along the trail, which was left as a free parameter in Heinz et al. (2008), and which allows radio emitting particles to traverse the trail without significant losses.

Figure 2.5 shows synchrotron surface brightness for the 300 km s^{-1} simulation at 100,000 years. Surface brightness for synchrotron emission is strongest at the front-edge where the jets are bent by ram pressure. The terminal radio bubble is also bright and emits the bulk of the total radio luminosity.

In fig. 2.5, the typical brightness temperature inside the bubble is estimated to be of order a few K in model hvc at 0.1 Myr at a frequency of 1 GHz. Since the synchrotron emission depends only on the pressure, the typical values of brightness temperature in other models ($v_{\rm XRB}$=30, 100 km s^{-1}) are essentially the same.

If the intensity of synchrotron emission is high enough, synchrotron self-absorption will occur and the emission will drop out at low frequencies, proportional to $\nu^{5/2}$ regardless of the electron power index. However, in our particular simulation, the

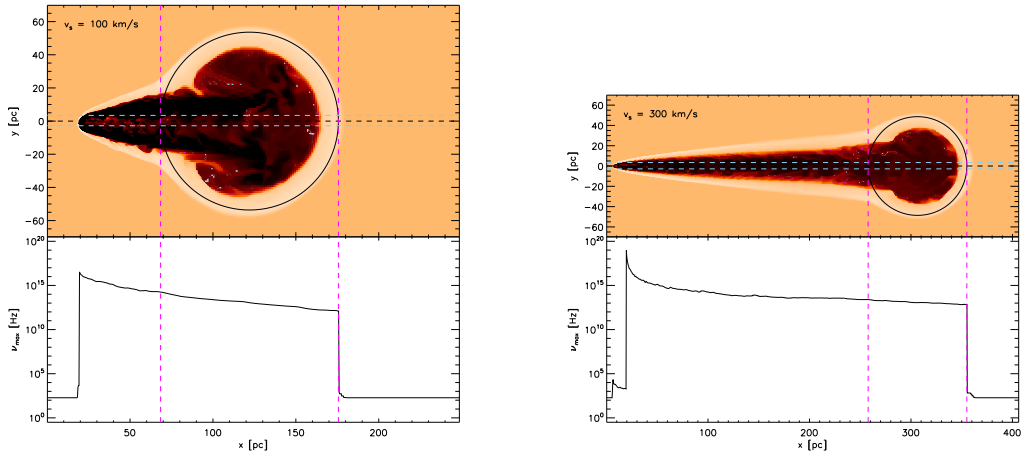

Fig. 2.4. — : Synchrotron cooling frequency for X-ray binaries at 100 km s^{-1} (left panel) and 300 km s^{-1} (right panel) at 1 Myr. Top images indicate the density map with logarithmic scale. The vertical magenta lines indicate edges of the bubble area (marked with the solid circle). The cutoff frequency is calculated by integrating along the two blue lines and assuming a steady state.

optical depth at 1 GHz is quite transparent (about $\tau = 10^{-2}$) so this effect would be negligible.

The bright temperature can be extrapolated into a few 10^{-3} K in submm wave bands that might be detectable by a new generation detectors such as SCUBA-2 or ALMA. In the case of the XRBs in our galaxy, assuming that the distance would be a few kpc, the angular size of the bubble is large enough to be resolved by these detectors.

Since the pressure inside the bubble decreases with time, the surface brightness will also decrease with time and synchrotron radiation will be easier to observe at an earlier XRB age if the bubble is resolved.

The synchrotron emission from the bubble can easily be predicted analytically.

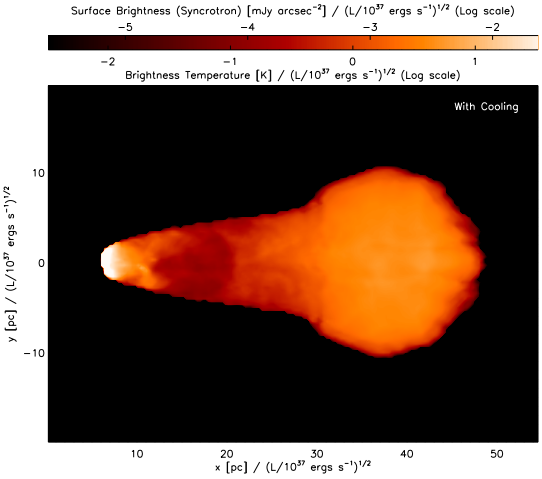

Fig. 2.5. — : Surface brightness of radio synchrotron emission for the frequency of 1 GHz at 100,000yr ($v_{\rm XRB} = 300$ km s^{-1}).

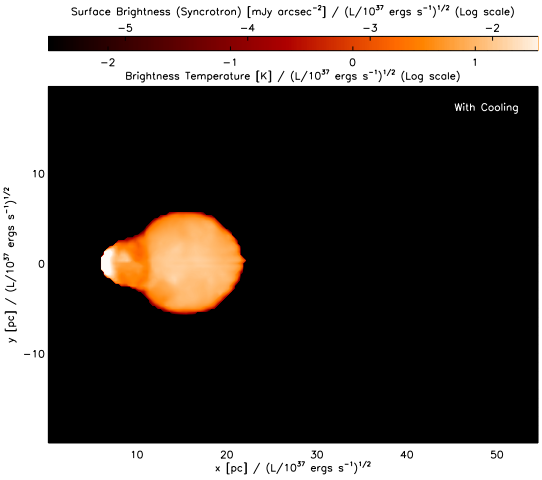

Fig. 2.6. — : Surface brightness of radio synchrotron emission for the frequency of 1 GHz at 30,000yr ($v_{\rm XRB} = 300$ km s^{-1}).

For a power-law distribution of electrons, $N(\gamma)d\gamma = A\gamma^{-p}d\gamma$: if we assume the power-law index (p) is 2.5, the total emissivity per unit volume per unit frequency can be calculated as,

$$\epsilon_{sync} = C_3 P^{15/8}, \tag{2.28}$$

where P is the pressure in the bubble and C_3 is approximately 1.44×10^{-17} and depends on the ratio of electron to magnetic pressure. Throughout this discussion we will assume that the plasma is in equipartition (with equal energy density in electrons and magnetic field), making the estimated fluxes *upper limits*.

The pressure of the hot bubble can be estimated from the shock jump conditions. If we set the adiabatic index to 5/3, the pressure jump condition in the shell of the bubble are given by eqn. 2.5.

Figure 2.7 shows that the inferred post-shock pressure is consistent with the simulation results, although the data from the simulation have a slightly smaller values. The small discrepancy is negligible in estimating the surface brightness.

The surface brightness can be derived from the emissivity (eqn. 2.28) with post-shock pressure and the path length of the line of sight in bubble. Hence the maximum value of path length is $\mathrm{R}_{bub}(\mathrm{t})$, and the surface brightness becomes

$$\begin{aligned} I_{sync} &\approx \frac{C_3}{4\pi}\left(\frac{27}{100}C_1^{2/5}L^{2/5}\rho_0^{3/5}t^{-4/5}\right)^{15/8} C_1^{1/5}L^{1/5}\rho_0^{-1/5}t^{3/5} \\ &\approx 1.37\times10^{-3}\mathrm{mJy\ arcsec^{-2}} \times (L_{37})^{19/20}\,(\rho_{0H})^{37/40}\left(\frac{t}{1\mathrm{Myr}}\right)^{-9/10} \end{aligned} \tag{2.29}$$

This theoretical calculation is in good agreement with numerical data shown in fig. 2.8. The relation confirms that the synchrotron emission decreases over time,

implying that younger XRBs are more easily detected in the radio.

XRB bubbles in other galaxies will be difficult to resolve with radio observations, but may be detectable as unresolved sources, at locations *different* from the X-ray point source. If we set the distance to the XRBs to be D, then we can estimate the unresolved flux as,

$$\begin{aligned} \mathrm{Flux}_{\mathrm{sync}} &\approx \frac{C_3}{16\pi}\left(\frac{27}{100}C_1^{2/5}L^{2/5}\rho_0^{3/5}t^{-4/5}\right)^{15/8} C_1^{3/5}L^{3/5}\rho_0^{-3/5}t^{9/5}D^{-2} \\ &\approx 0.04\ \mathrm{mJy}\times\left(L_{37}\right)^{27/20}\left(\rho_{0H}\right)^{21/40}\left(\frac{t}{1\mathrm{Myr}}\right)^{3/10}\left(\frac{D}{1\mathrm{Mpc}}\right)^{-2} \end{aligned} \quad (2.30)$$

This flux includes only the bubble area, and neglects the synchrotron emission from near the jets. Because we do not resolve the base of the inner regions of the jet in our simulations, and because microquasars are generally highly variable, we cannot make any quantitative statements about the relative flux from the inner jet and the bubble. Note that the total flux from the trail and bubble *increases* with time, indicating that older XRBs will be easier to detect than young ones in unresolved observations.

The state-of-the-art radio observatories are well suited for this type of objects; the eVLA has been upgraded to have the excellent sensitivity, frequency coverage, and imaging capability that allows for good quality radio spectra resolved over the source, and the WSRT APERTIF that has very large field of view at 1.4 GHz, allowing for deep continuum surveys capable of detecting trailed nebula.

2.3.3.3 Free-free emission

For the expected temperature range in the bow shock, we can expect the gas to be mostly or completely ionized, which will give rise to the emission of

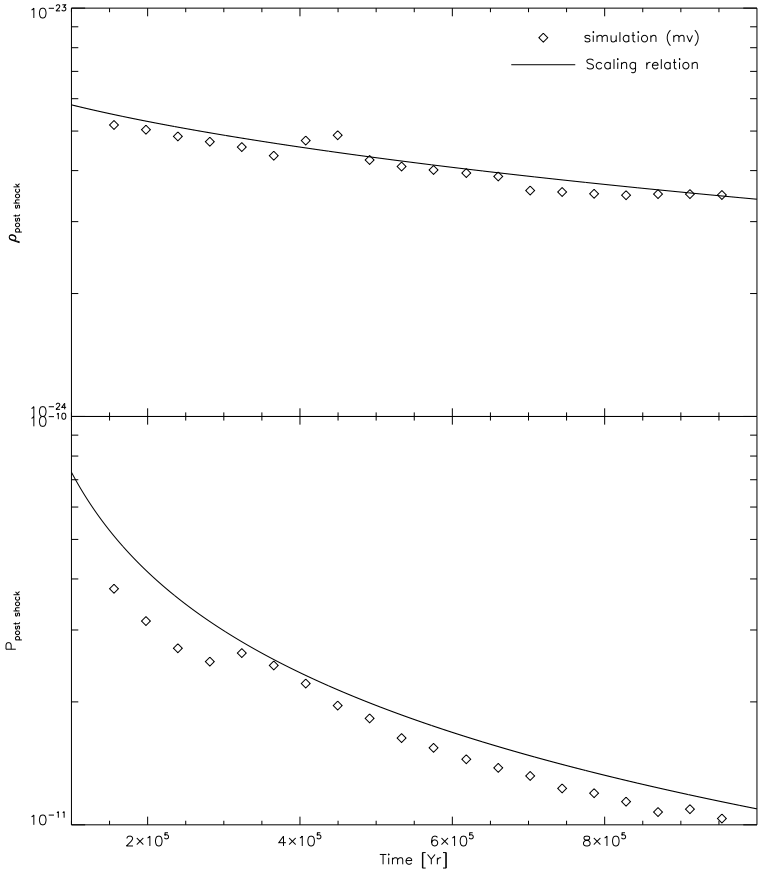

Fig. 2.7. — : The solid line indicates that post shock pressure and density derived from scaling relation and diamond marks the results from simulation.

Bremsstrahlung. Figure 2.9 shows a simulated radio image in free-free emission for the case of $v_{\rm XRB}$ =300 km s^{-1}. The emission is edge–brightened, given that it comes exclusively from the compressed ISM shell.

The temperature at the shell of the bubble can be calculated by the post-shock density and pressure as

$$T_{bub} = \frac{\mu}{k}\frac{P_1}{\rho_1} \approx \frac{27}{400} C_1^{2/5} \frac{\mu}{k} \rho_0^{-2/5} L^{2/5} t^{-4/5},$$

where μ is mean molecular mass. If we assume fully ionized gas inside the shell, the

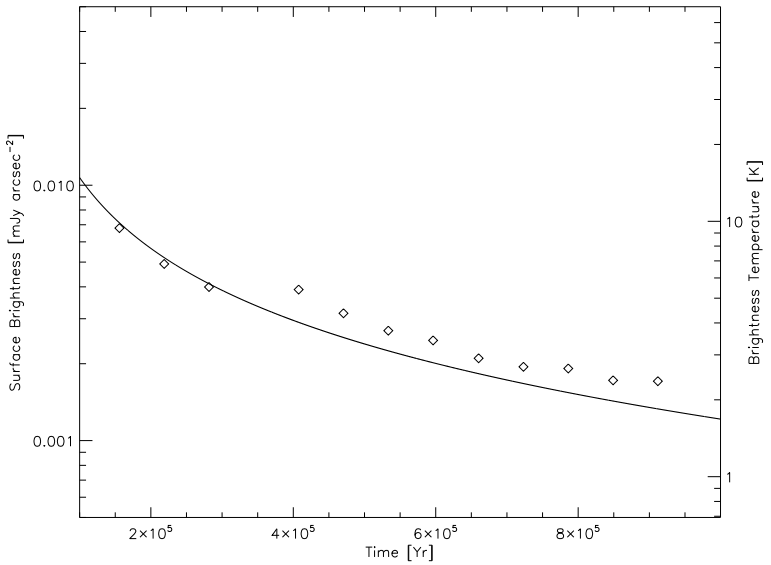

Fig. 2.8. — : The solid line indicates the theoretically expected surface brightness in synchrotron emission and diamond indicates the results from simulation.

free-free surface brightness through the shock can be approximately written as

$$I_{ff} \approx 3.91 \times 10^{-20} \text{ ergs s}^{-1}\text{cm}^{-2}\text{Hz}^{-1}\text{str}^{-1} \times (\rho_{0H})^2 \left(\frac{t}{1\text{Myr}}\right) \qquad (2.31)$$

where we assume a strong shock with $\rho_{shock} \approx 4\rho_0$ for simplicity.

Free-free emission is dimmer than the synchrotron emission in the bubble, and is expected to be undetectable or marginally detectable at ν=1Ghz.

For the shock temperatures in our simulations ($10^4 - 10^6$ K), optical emission is dominated by cooling lines rather than free-free continuum emission. However, for a fast source the temperature in the bow shock may initially exceed 10^6 K, in which case free-free emission would be the dominant coolant.

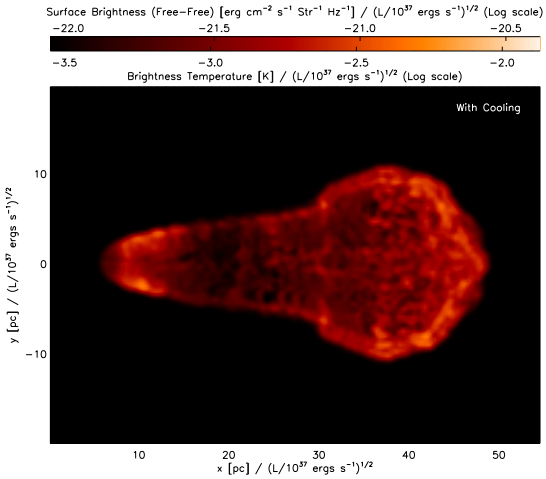

Fig. 2.9. — : Surface brightness of free-free emission for the frequency of 1GHz at 100,000 yr ($v_{xrbs} = 300$ km s^{-1}).

2.3.3.4 X-ray

For large enough space velocities, the temperatures at the stagnation point of the bow shock can be sufficiently high to produce X-rays. Fig. 2.10 shows a simulated Chandra X-ray observation produced using the XIM program (Heinz & Brüggen 2009) for the 300 km s^{-1} simulation at a distance of 5 kpc with a 100 ks exposure at 10^6 years.

For the fiducial parameters, there is a significant flux only from the bow shock, which has a temperature of about 2×10^6 K. However, it may be difficult to distinguish this flux from the emission from the XRB. There is a small amount of X-ray emission from the neck, but it is only marginally distinguishable from the background, and fades as you go farther down the neck.

At early times, the expanding bubble produces a detectable X-ray flux. Figure 2.11 shows a simulated Chandra X-ray observation for the 300 km s^{-1} simulations

(hvc) at a distance of 8 kpc with a 100 ks exposure at 30,000 years. Although it has a low surface brightness, the bubble and neck can be seen, in addition to the bright bow shock, in a smoothed image.

A shock will only be detectable in X-rays if its temperature is above about 5×10^5 K, which corresponds to a shock velocity of about 100 km s^{-1} for the parameters in our simulations. Assuming a strong shock, the shock temperature is

$$T_s \sim 6.79 \times 10^3 K \times M_s^2 \times \left(\frac{P_0}{3 \times 10^{-12}}\right)\left(\frac{\rho_0}{1.67 \times 10^{-24}}\right) \tag{2.32}$$

The bubble expansion falls below about 100 km s^{-1} at about 36,000 years. After this, the bow shock is still visible, if the XRB is moving fast enough, but the bubble and neck are unlikely to be detected. The bow shock is always visible, but only for XRBs moving faster than about 100 km s^{-1}.

The synchrotron emission from relativistic particles does not produces a detectable X-ray flux.

2.4 Comparison with SAX J1712.6-3739

While the numerical results and the analytic approximations derived from them are primarily predictive, we can, at the very least, directly apply them through comparisons to the one known XRB with a bow shock nebula.

SAX J1712.6-3739 is so far the only XRB found to display a prominent H_α bow shock nebula (Wiersema et al. 2009). Following the original discovery of the bow show, a deep VLT observation of the source was obtained to confirm the detection and look for further structure in the H-alpha map. This observation is shown in

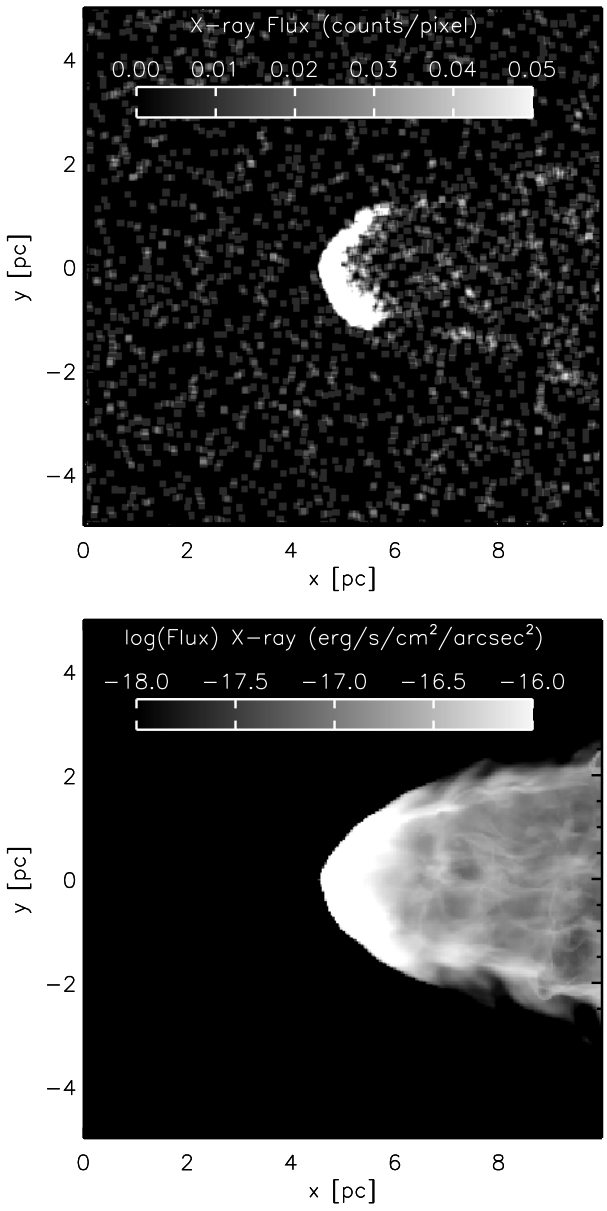

Fig. 2.10. — : Simulated Chandra X-ray image (top) and surface brightness (bottom) of the bow shock for the 300 km s^{-1} simulation at 1 Myr. 100 ks exposure at 5 kpc and flux is integrated from 0.3 to 3 keV. The maximum flux in the bow shock is about 1 count/pixel.

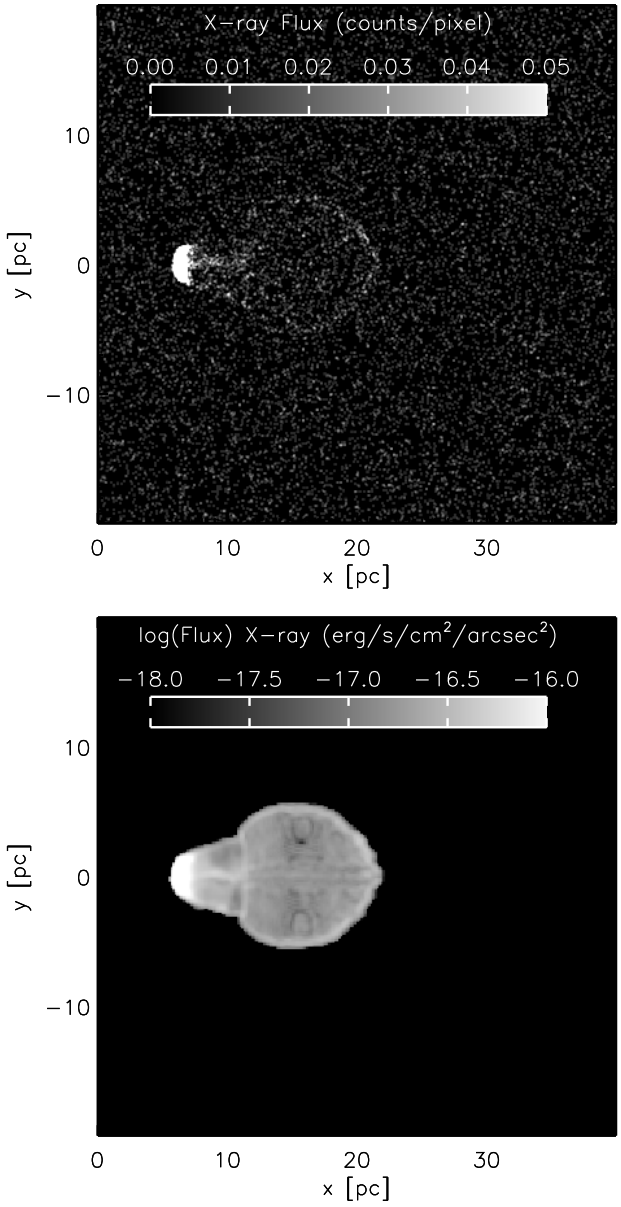

Fig. 2.11. — : Simulated Chandra X-ray image (top) and surface brightness (bottom) of the bubble for the 300 km s^{-1} simulation (hvc) at 30,000 years. 100 ks exposure at 8 kpc and flux is integrated from 0.3 to 3 keV.

Fig. 5.1.

2.4.1 Data reduction

The data were taken using the Focal Reducer and low dispersion spectrograph (FORS2) on the Very Large Telescope (VLT, Chile), using the H$_\alpha$+83 interference filter. As part of a larger programme (ESO programme ID 385.D-0100, PI Russell), we obtained 34 exposures of 60 seconds each on 16 April 2009, under excellent seeing conditions (average 0.7 arcseconds).

The data were reduced using standard procedures in *IRAF* and combined. Details on the reduction and flux calibration of these data will be reported in a forthcoming publication (Russell et al. in prep.). The FORS2 data cover a much larger sky area than the EFOSC2 data reported in Wiersema et al. (2009) at a better resolution, and have significantly better signal to noise, allowing us to search for fainter features and both small and large scale structure.

2.4.2 Model comparison

The new VLT observation confirms the presence of a bright bow shock nebula, as first reported in Wiersema et al. (2009). In addition, the image suggests the presence of a roughly circular shell of H$_\alpha$ emission with a radius of 76" which connects to the previously observed linear H$_\alpha$ features near the XRB. While the level of patchy background H$_\alpha$ emission makes a firm identification difficult, we interpret this cavity or shell as the bubble inflated by the backflow through the channel. The estimated location of the bubble and neck are sketched in the lower panel of figure 5.1. The distance from the end of the neck to the center of the bubble is about 190" .

We estimate the half opening angle of the bow shock seen in the H$_\alpha$ emission

to be about 15°, which can be converted into the projected oblique shock angle of $\beta = 0.261799$. From the observed ratio of bubble size to neck length, our analytic model would predict a neck opening angle of about 19°, somewhat larger than the observed value. Assuming the bubble is expanding supersonically, we can set a lower limit on the Mach number of the source from eqn. 2.19 of

$$M_s \geq \frac{1+\beta}{\beta} M_b \geq 4.8 \tag{2.33}$$

For our assumed sound speed of 17.3 km s^{-1}, this implies the velocity of the source is $v_s \geq 83$ km s^{-1}. The source could also have a component of motion towards or away from us which is not constrained by the opening angle of the neck.

Given the distance of the object of $D \sim 7\,\mathrm{kpc}$ and the approximate angular size of the putative shell of 76", we estimate the physical radius of the bubble to be $R_{\mathrm{bubble}} \sim 2.6\,\mathrm{pc}$. In order to check the consistency between the observation and our model, we carried out a simulation with $v_s = 100$ km s^{-1}. Using the scaling relation of bubble radius from eqn. (2.2) and a standard ISM density of $1\,\mathrm{cm}^{-3}$, the appropriate luminosity is $L = 8.5 \times 10^{33}$ ergs s^{-1} and the age of the bubble would be approximately 70,000 years:

$$t_{SAX} \approx 70,000 \text{ yr} \left(\frac{L_{8.5e33}}{\rho_{0H}}\right)^{-1/3} \left(\frac{R_b}{2.57\mathrm{pc}}\right)^{5/3} \tag{2.34}$$

where $L_{8.5e33} = \frac{L}{8.5\times10^{33} \text{ ergs s}^{-1}}$.

In terms of source power and ISM density, the velocity of SAX J1712.6-3739 can be estimates to be

$$v_s \;=\; 100 \text{ km s}^{-1} \left(\frac{L_{8.5e33}}{\rho_{0H}}\right)^{-1/3} \tag{2.35}$$

A higher energy (or lower ambient density) implies a higher velocity required of the source by eqn. 2.35 to have the same neck length at a given bubble size. If the motion of the binary is not perpendicular to our line of sight, but rather inclined at an angle α, then the true opening angle of the source is $\beta_{true} = \beta \sin \alpha$ and the velocity of SAX J1712.6-3739 would have to increase by $1/\sin \alpha$. Eqn. 2.35 is therefore a lower limit on the source velocity for a given set of parameters. Based on the velocity analysis, a proper motion of SAX J1712.6-3739 can be estimated as a few mas/yr. This proper motion scale will be observable from the LSST. If the velocity is measured directly, it would help to constrain our models and allow us to determine the jet power in terms of just the ambient density or vice versa.

In figure 5.1, the H_α emission in the neck is brighter than that in the expanding bubble while we expect it to be relatively dim from our fiducial simulations.

It is possible that this is due to the inclination angle for the moving XRBs with respect to the line of sight. If the source is moving at a substantial angle with respect to the plane of the sky, then the amount of neck material we are looking through increases while the thickness of the spherical bubble stays the same. As a result, with some large inclination angle, the emission of the neck can be brighter than that of the bubble.

It is also possible that radiative cooling in the shell around the bubble has moved much of the gas to temperatures too low to emit in H_α, while the neck is still at a sufficiently high temperature to emit, given that the bow shock and Mach cone have a higher Mach number and pressure than the bubble and shell. Because radiative cooling breaks the scale invariance of our simulations, a more detailed investigation would require the construction of a large grid of simulations at different

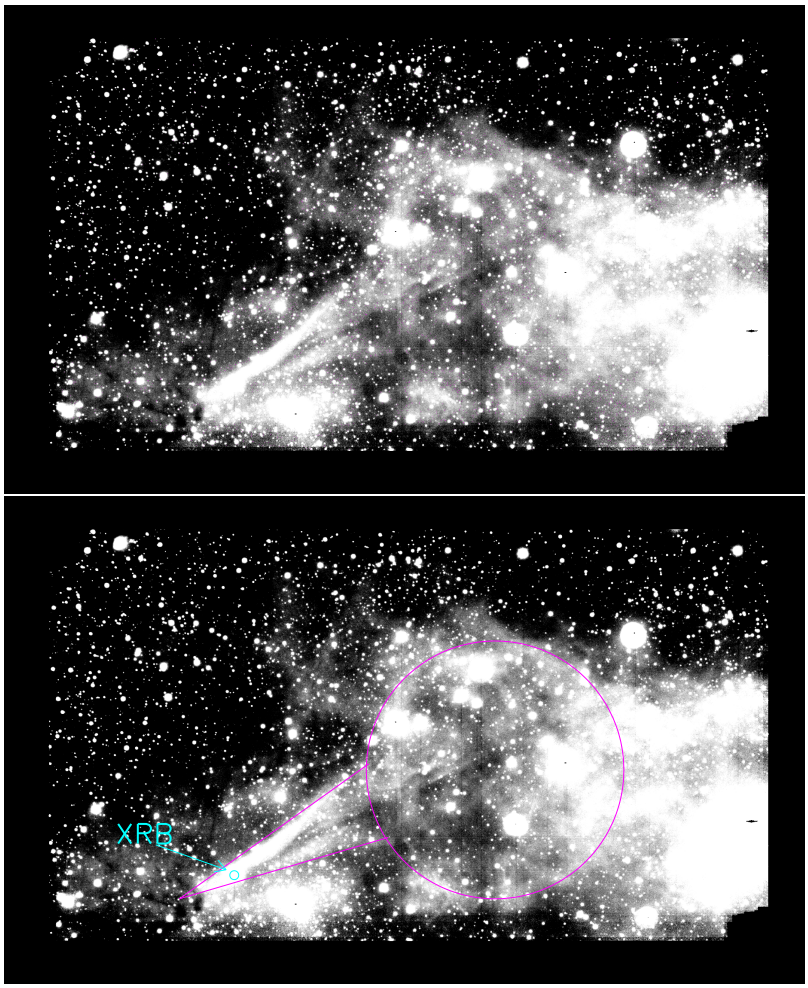

Fig. 2.12. — : SAX J1712.6-3739 image from the VLT FORS2 H_α data (upper panel), and same image with location of the neck and bubble highlighted (lower panel).

source powers and ISM temperatures, which would be well beyond the scope of this paper.

It is also possible that the relative brightness is simply a result of the complicated morphology of background emission surrounding the observed H_α nebula. The surrounding emission is clearly non-uniform. A more detailed and quantitative investigation of the new VLT observations is forthcoming in a separate paper.

The difficulty in interpreting the complex structure of the observation notwithstanding, we carried out three simulations with the initial conditions expected to produce a size and shape close to SAX J1712.6-3739 to test whether we could match the observed shape and relative brightness of the neck and bubble. The parameters of these simulations are listed in table 1 as fit1, fit2 and fit3. In figure 2.13, the top panel shows the results when the ejected energy is 8.47×10^{33}ergs s^{-1} and the velocity of the XRB is 100 km s^{-1} (model fit1). There is bight H_α emission in the bow shock and dimmer but still bright emission from the bubble. However, the emission in most of the neck is relatively dim compared to the shell.

In order to inspect the inclination angle effect, we ran simulation fit2 with a higher velocity of 200 km s^{-1} and display it with an inclination angle of 60° (middle panel). In this case the emission is brightest in the bow shock, part of the neck and the leading edge of the bubble, with somewhat dimmer emission from the trailing edge of the bubble. This is somewhat closer to the bright neck seen in SAX J1712.6-3739, although the location of bright neck emission does not match the observation exactly. The width of the neck relative to the bubble size is about the same as the 100 km s^{-1} case, and there is still a large gap in the neck with very little emission.

Finally, we ran simulation fit3 with a larger power of $L = 2.29 \times 10^{35}$ergs s^{-1}, and higher velocity velocity of $v_{\rm XRB} = 300$ km s^{-1} (bottom panel). For the given bubble size, the age is reduced to 23,000 years (eqn. 2.34). Note that because the emission is significantly brighter in this model, the intensity scale for the bottom panel is increased by a factor of 10 compared to the other two panels to avoid color saturation. In this case, there is no emission from the bow shock, due to the high temperature caused by the faster source. There is bright emission in part of the neck,

where the shock has become cool enough to emit in H_α, and there is about equally bright emission from the bubble edges. By varying the source velocity, it is possible to move the location of bright neck emission from the bow shock (for model fit1) far down stream in the neck (for model fit3) and it could be moved even farther away from the XRB for a faster source velocity.

These three simulations differ substantially in their relative surface brightness distributions of H_α emission in bow shock, neck, and shell, showing that it should be possible to construct a reasonable fit to the observations with sufficient fine tuning.

2.5 Conclusion & Summary

By way of numerical simulations, we study the morphological evolution and dynamics of microquasars with high space velocity, the functional equivalent of narrow-angle tail radio galaxies for accreting stellar mass black holes and neutron stars. Such dynamic X-ray binaries initially create a powered, spherically expanding shock/bubble, the expansion of which eventually decelerates to less than the velocity of the XRB relative to the ISM.

When the source reaches the edge of the bubble, it establishes a well defined structure with a bow shock around the source at one end, a spherical bubble at the other, and a neck connecting the bow shock and bubble. The shock angle around neck, β, decreases as the binary moves away from the bubble, but it cannot be less than $1/M_0$, where M_0 is the Mach number of the binary relative to the surrounding medium.

The shocks from all three components creates H_α emission that should be detectable in narrow band imaging. At early times, less than about 30,000 years in

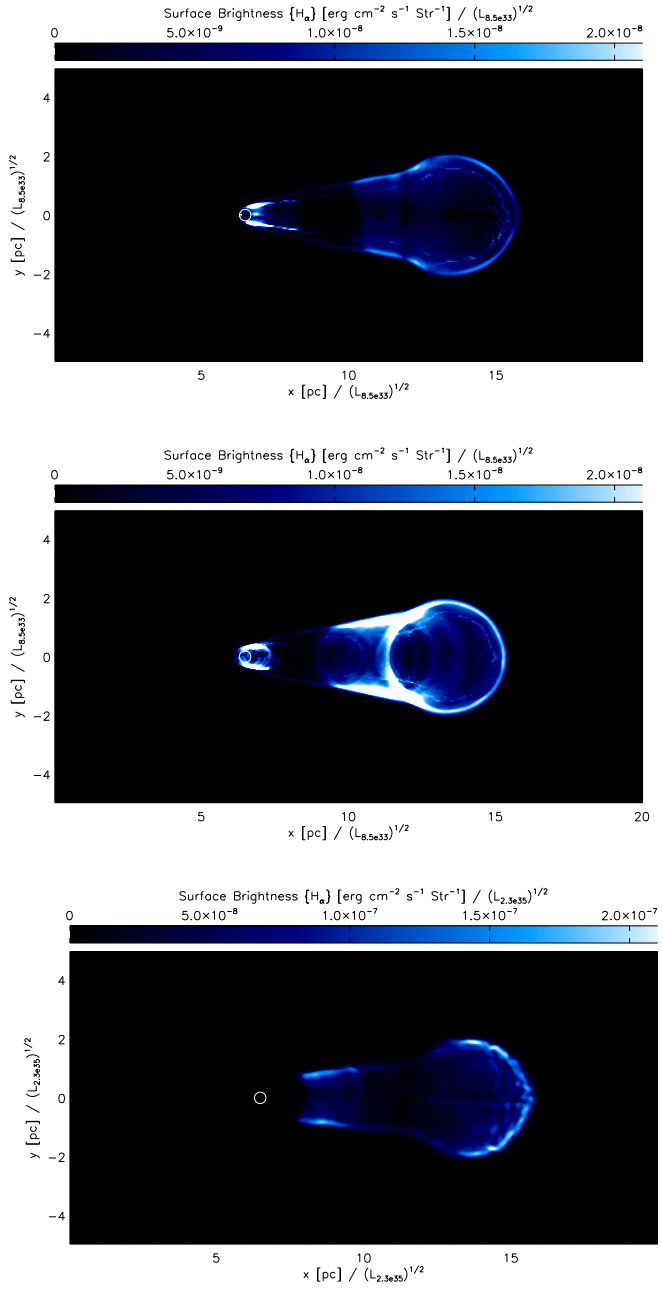

qq

Fig. 2.13. — : H_α images with different initial conditions; $L = 8.47 \times 10^{33}$ergs s^{-1}, $v_{\rm XRB} = 100$ km s^{-1} and edge-on at 69,000 yr (top panel), $L = 8.47 \times 10^{33}$ergs s^{-1}, $v_{\rm XRB} = 200$ km s^{-1} and inclination angle of 60° at 69,000 yr (middle panel), $L = 2.29 \times 10^{35}$ergs s^{-1}, $v_{\rm XRB} = 300$ km s^{-1} and edge-on at 23,000 yr (bottom panel). Note that the intensity scale of the bottom panel is 10 times higher than the other two panels.

our simulations, X-ray emission will be detectable around the bubble and neck, but this rapidly fades as the shock temperature decreases. At later times, X-ray emission is only detectable from the bow shock and only for fast sources ($v_s \geq 100$ km s^{-1}).

Synchrotron radio emission from the bubble is bright and covers a large area, but emission from the neck is significantly weaker. There is also strong synchrotron emission from near the binary, but it only covers a small area and thus would be difficult to detect without high resolution. Bubbles created by galactic XRBs should be visible in surveys of diffuse continuum emission. Binaries in other galaxies may also be detectable with a resolution such that the beam size is approximately the size of the bubble. The free-free emission is dimmer than the synchrotron emission and is generally not detectable.

New H_α observations of SAX J1712.6-3739 presented here (see §2.4) show both a strong bow shock and tentative evidence for a spherical shell trailing the XRB, consistent with the neck and bubble morphology predicted by our simulations. We are also able to constrain the Mach number of the XRB relative to the background ISM to be $M_s \geq 4.8$, corresponding to a velocity of $v_s \geq 83$ km s^{-1} in the plane of the sky for a sound speed of 17.3 km s^{-1}.

Extending our results into pulsar bow shock nebulae (PWBN) is plausible, since bow shock structures of PWBN are well described by the simulations presented in this paper. For example, the H_α images of PSR B2224+65 (Chatterjee & Cordes 2002; Cordes et al. 1993), called "Guitar nebula" for its peculiar shape, shows well developed structures of trailing neck and spherical bubble. We will present models specific to PWBN in a future paper.

References

Bell, J. F., Bailes, M., Manchester, R. N., Weisberg, J. M., & Lyne, A. G. 1995, ApJ, 440, L81

Bernstein, J. P., & Hughes, P. A. 2009, Journal of Computational Physics, 228, 6212

Bosch-Ramon, V., Perucho, M., & Bordas, P. 2011, A&A, 528, A89+

Castor, J., McCray, R., & Weaver, R. 1975, ApJ, 200, L107

Chatterjee, S., & Cordes, J. M. 2002, ApJ, 575, 407

Cordes, J. M., Romani, R. W., & Lundgren, S. C. 1993, Nature, 362, 133

Cox, D. P. 2005, ARA&A, 43, 337

Fender, R. P., Belloni, T. M., & Gallo, E. 2004, MNRAS, 355, 1105

Fryxell, B., Olson, K., Ricker, P., et al. 2000, ApJS, 131, 273

Gaensler, B. M., van der Swaluw, E., Camilo, F., et al. 2004, ApJ, 616, 383

Gallo, E., Fender, R., Kaiser, C., et al. 2005, Nature, 436, 819

Hao, J. F., & Zhang, S. N. 2009, ApJ, 702, 1648

Heinz, S., & Begelman, M. C. 1997, ApJ, 490, 653

Heinz, S., & Brüggen, M. 2009, ArXiv e-prints, arXiv:0903.0043

Heinz, S., Brüggen, M., Young, A., & Levesque, E. 2006, MNRAS, 373, L65

Heinz, S., Grimm, H. J., Sunyaev, R. A., & Fender, R. P. 2008, ApJ, 686, 1145

in 't Zand, J., Heise, J., Bazzano, A., Cocchi, M., & Smith, M. J. S. 1999, IAU Circ., 7243, 2

Körding, E., Rupen, M., Knigge, C., et al. 2008, Science, 320, 1318

Migliari, S., & Fender, R. P. 2006, MNRAS, 366, 79

Miley, G. K., Perola, G. C., van der Kruit, P. C., & van der Laan, H. 1972, Nature, 237, 269

Mirabel, I. F., Dhawan, V., Mignani, R. P., Rodrigues, I., & Guglielmetti, F. 2001, Nature, 413, 139

Rafferty, D. A., McNamara, B. R., Nulsen, P. E. J., & Wise, M. W. 2006, ApJ, 652, 216

Stappers, B. W., Gaensler, B. M., Kaspi, V. M., van der Klis, M., & Lewin, W. H. G. 2003, Science, 299, 1372

Stappers, B. W., Jones, D. H., & Gaensler, B. M. 2002, in Astronomical Society of the Pacific Conference Series, Vol. 271, Neutron Stars in Supernova Remnants, ed. P. O. Slane & B. M. Gaensler, 141–+

Sutherland, R. S., & Dopita, M. A. 1993, ApJS, 88, 253

Tudose, V., Fender, R. P., Linares, M., Maitra, D., & van der Klis, M. 2009, MNRAS, 400, 2111

Wiersema, K., Russell, D. M., Degenaar, N., et al. 2009, MNRAS, 397, L6

Chapter 3

The Dynamics of Bow Shock Pulsar Wind Nebulae in Non-uniform Ambient Medium

This chapter is in preparation to The Astrophysical Journal

D. Yoon, & S. Heinz 2015b, ApJ, in prep.

Abstract

Bow shock pulsar wind nebulae are a subset of pulsar wind nebulae that form when the pulsar has high velocity due to the natal kick during the supernova explosion. The interaction between the relativistic wind from the fast-moving pulsar and the interstellar medium produces a bow shock and a trail, which are detectable in H_α emission. Among such bow shock pulsar wind nebulae, the Guitar Nebula has peculiar morphology, which consists of a prominent bow shock head and a series of bubbles further behind. We present a scenario in which multiple bubbles can be produced when the pulsar encounters a density discontinuity due to the abrupt change of standoff distance in the bow shock. We tested the scenario by using 2-D/3-D hydrodynamic simulations, and reproduce the observed guitar shape in the Guitar Nebula from a series of density changes in the medium. We also show that if a pulsar encounters an inclined density discontinuity, it produces asymmetric bow shock head, which appears in millisecond pulsar J2124-3358.

3.1 Introduction

Pulsar Wind Nebula (PWNe) are shocked layers, produced when a pulsar's relativistic wind interacts with the surrounding medium. They produce broad range of emissions from radio synchrotron emission to γ-rays [Gaensler & Slane (2006) and references therein]. A subset of PWNe has been identified, in which pulsars with high spatial velocities produce bow shock structure and cometary shapes [e.g., B1957+20 (Kulkarni & Hester 1988); J0437-4715 (Bell et al. 1995); RXJ1856.5-3754 (van Kerkwijk & Kulkarni 2001); B0740-28 (Jones et al. 2002); J2124-3358 (Gaensler et al. 2002); J1747-2958 (the "mouse" nebula) (Gaensler et al. 2004)]. Such bow shocks are detectable in collisionally excited H_α emission (van Kerkwijk & Kulkarni 2001; Jones et al. 2002). A theoretical model of the Balmer-dominated pulsar bow shocks was developed by Kulkarni & Hester (1988). In the model, the Balmer emissions arise from pre-shock H atoms, being excited by collisions with the post-shock hot plasma.

Bernstein & Hughes (2009) carried out special relativistic, hydrodynamics simulation, and discussed that a relativistic backflow from a fast-moving pulsar thermalize energy, allowing the flow to inflate the trailing spherical bubble. This energy-supported bubble model is also shown in Yoon et al. (2011) for low-mass X-ray Binaries. This model describes the evolution of bow shock PWNe in early stage, when the pulsar locates not far away from its birth-place. The presence of bubbles behind the pulsar in later stage can not be explained by the bubble model in which the bubble initiated in supernova explosion.

A pulsar's high-spatial velocity is caused by the natal kick of the neutron star during its supernova explosion. Numerous models have been proposed to take into account the deviation from spherical symmetry at the core of the progenitor star. This deviation can occur because of anisotropic neutrino emission during the Kelvin-Helmholtz cooling of the nascent remnant (Sagert & Schaffner-Bielich 2008), anisotropic mass ejection during the SN explosion due to standing-accretion shock instability (Blondin et al. 2003; Hanke et al. 2012), or convective shell-burning during the final life cycle stage of the progenitor star (Burrows & Hayes 1996).

The Guitar Nebula is one of the most spectacular PWNe, produced by one of the fastest known pulsars, PSR B2224+65, which has a transverse velocity of $v_{\perp} \geq 1000\,\mathrm{km\,s^{-1}}$. In H_{α} observations, the nebula has a guitar-like shape with a bright head, trailing neck, and a series of bubbles (Cordes et al. 1993; Chatterjee & Cordes 2002). A possible explanation for the multiple bubbles is that the morphology may be affected by changes in any of the variables which relate to determine standoff distance, at which the pressure is balanced between the pulsar wind and the medium thrust. However, Chatterjee & Cordes (2004) claimed that there is a negligible amount of time-variable $\dot{E}$ compared to large morphological changes, and time-variable $\dot{E}$ fails to account for the brightening in the constricted region of the nebula. In consequence, the variation of the ambient density likely play a vital role in the evolution of the Guitar Nebula although instabilities in bow shock backflow, could produce similar results (van Kerkwijk & Ingle 2008). Small-scale density variations corresponding to tens of AU are observed in the Galactic HI absorption (Deshpande 2000; Faison & Goss 2001). Patat et al. (2010) also detect interstellar medium (ISM) column density variations on scales of ~ 100 AU by using the fast expansion of a Type Ia supernova

photosphere.

The primary goal of this study is to investigate the dynamic evolution of bow shock PWNe in inhomogeneous environments. Noutsos et al. (2013) reported that characteristic timescale $\tau_c = P/(2\dot{P})$ and kinematic ages $t_{\rm kyn}$ of the sampled pulsars are within the range $10^5 \sim 10^7\,{\rm yr}$. Under the reasonable assumption that pulsars are born somewhere within 100 pc of the galactic mid-plane, they are expected to intersect the galactic plane at least once in the time travel. It is quite possible that fast-moving pulsars encounter significant changes in their environment. In this paper, we modeled evolution of the bow shock PWNe when the pulsar passes through density discontinuities using multidimensional hydrodynamic simulations; we primarily performed two dimensional axisymmetric runs, but we also carried out 3-D runs for non-axisymmetric cases (*e.g.*, inclined density discontinuity should be developed in 3-D). We mainly used a non-relativistic hydrodynamic algorithm, but we tested some cases with relativistic hydrodynamics to verify our runs.

In this study, we discuss the origin of trailing bubbles which appear in several bow shock PWNe. Since the bubbles are not produced by initial supernova explosion if the pulsar locates sufficiently far away from its birth-place, their existence should be explained by instabilities or variation of density in the medium. We focus that the interaction of a pulsar wind and the non-uniform medium may cause producing additional bubbles. We also develop analytic formula for a bow shock and a neck to discuss the morphological variations of these structures when the pulsar passes along a non-uniform medium.

The organization of this paper is as follows. In Section 2, the numerical method and the initial setup will be presented. In Section 3, we discuss the evolution of the

PWNe encountering density discontinuities. In Section 4, we compare our numerical results with H_α observation of the Guitar Nebula. In Section 5, we summarize our results.

3.2 Numerical method

3.2.1 The code

Simulations were carried out with the FLASH 3.3 hydrodynamic code (Fryxell et al. 2000), which is a modular and parallel simulation code suitable to solve compressible flow problems. An adaptive mesh refinement (AMR) algorithm in the code enables us to investigate global structure in the evolution of PWNe efficiently using moderate computing resources. We adopt the piecewise-parabolic method (Colella & Woodward 1984) as a Riemann solver. We use a multi-gamma equation of state, where the adiabatic index of the ambient medium is $\gamma_{\rm ambient} = 5/3$ and that of the pulsar wind is $\gamma_{\rm pulsar} = 4/3$.

3.2.2 Pulsar Wind

The magnetic field interacts with charged particles around a neutron star. The bulk of the spin-down energy is converted into a relativistic pulsar wind (Michel 1969). In general, the anisotropy of the wind momentum flux should be taken into account to explain detailed bow shock structures (Vigelius et al. 2007). However, the global features produced by interactions between pulsar winds and surrounding medium are less influenced by the anisotropy of the wind. Moreover, there is no evidence for anisotropic- or clumping-pulsar winds in the series of H_α observations of the Guitar Nebula (Chatterjee & Cordes 2004). Therefore, we developed the pulsar

wind as a spherical nozzle injecting flux isotropically through the surface.

The pulsar wind is ultra-relativistic, interacting with the ambient medium of either the supernova remnant (SNR) or the ISM, and the Lorentz factor is in the range of $10^4 \sim 10^7$ (Kennel & Coroniti 1984). The pulsar wind produces an expanding bubble of relativistic particles around the neutron star. In principle, to model the internal structure and properties of these nebulae, relativistic magnetohydrodynamic (RMHD) simulations are necessary (Bucciantini et al. 2005; Bernstein & Hughes 2009). However, because the evolution of large-scale bubbles and bow shock is non-relativistic, we carried out purely hydrodynamic simulations. We compared our results with relativistic pulsar wind model in Bernstein & Hughes (2009), and it shows no noticeable differences in the dynamics of PWNe. We also carried out one test run with relativistic algorithms that will be discussed in §3.4.3.

While a pulsar that loses energy at the rate of $\dot{E}$ moves through the ambient density of ρ_0 with the moving velocity of v_*, the resulting bow shock features should appear with the standoff distance, which is the stagnation point where the pulsar wind momentum flux is balanced by the ISM's ram pressure:

$$R_0 = \left(\frac{\dot{E}}{4\pi \rho_0 v_*^2 v_{\rm wind}} \right)^{1/2}, \tag{3.1}$$

where the pulsar wind velocity in our case is $v_{\rm wind} = 10^{10}\,{\rm cm\,s^{-1}}$. We set the injection radius of the nozzle to be arbitrary, but not to be larger than this standoff distance. Values of $\dot{E}$ for the observed pulsar population are in range of $10^{28} \sim 10^{38}\,{\rm ergs\,s^{-1}}$ (Manchester et al. 2005), and pulsars with $\dot{E} \gtrsim 10^{36}\,{\rm ergs\,s^{-1}}$ produce prominent PWNe (Gotthelf 2004). To test bow shock PWNe, we set $\dot{E} = 10^{36}\,{\rm ergs\,s^{-1}}$ for all cases except for the Guitar nebula model which has the spin-down loss energy rate, $\dot{E} = 10^{33}\,{\rm ergs\,s^{-1}}$ (Chatterjee & Cordes 2004). To resolve the pulsar wind and bow

shock structure appropriately, we set the numerical resolution around the pulsar to have at least 10 cells across it.

3.2.3 Initial setup and boundary condition

The pulsar is initially turned on and fixed at $x = 0$ for all runs. In order to develop moving pulsar, instead we set the streaming medium with velocity of 300, 600, and 900 $\mathrm{km\,s^{-1}}$. For the Guitar nebula model, we set the velocity to 1,500 $\mathrm{km\,s^{-1}}$. The left boundary of the simulation domain was applied to inflow boundary conditions with same velocity of the medium. These velocities represent the actual proper speeds of the pulsars.

Following Cox (2005), the pressure and density in the ambient medium are set to $P_0 = 3 \times 10^{-12}\,\mathrm{erg\,cm^{-3}}$ and $n_{ISM} = 1\,\mathrm{cm^{-3}}$. The ISM temperature is between $10^4 \sim 10^5$ K. To study the evolution of PWNe in density continuity, after the PWNe generates bow shock structures and bubbles behind it, a pulsar is forced to penetrate the density discontinuity toward an enhanced density region by a factor of 10, or toward a decreased density region of 1/10. For all cases, we adopt the same value of distance, $d = 4.12 \times 10^{18}\,\mathrm{cm}$, between the density-changed place and the initial location for the purpose of comparison. The detailed information we use for this study is listed in table 3.1.

We carried out mainly axisymmetric 2-D simulations for the purpose of saving computing resources, and carried out two sets of 3-D simulations: one for validating 2-D runs, and one for studying the non-axisymmetric case (See Table 3.1). The latter case is that the angle between the pulsar velocity and the density discontinuity is not perpendicular. For this case, we set the incident angle to be 45°, and the result

will be discussed at §3.4.2.

3.3 Results

3.3.1 Bow Shock Head

The global evolution of the bow shock structure is generally identical to that of supersonic LMXBs (Yoon et al. 2011), despite the different engine between the two systems. It is because that both a pulsar wind and a jet were swept back by ram pressure producing the bow shock structure when the objects move through ISM. Although a pulsar wind is more isotropic than a jet, the large scale bow shock is not influenced by the shape of the sources. Around the pulsar, the unperturbed pulsar wind extends to the termination shock where the wind slows down to subsonic speed because of its interaction with the ambient medium. The supersonic speed of

Table 3.1. : Parameter of the Simulations

Model	v_* [km s^{-1}]	density ratio[a]	transition width	dimension	incident angle
L10_300	300	0.1	instant	2-D	90°
H10_300	300	10	instant	2-D	90°
L10_600	600	0.1	instant	2-D	90°
L10_600_45deg	600	0.1	instant	3-D	45°
L10br_600	600	0.1	5×10^{17} cm	2-D	90°
H10br_600	600	10	5×10^{17} cm	2-D	90°
Uniform_600	600	1	-	2-D	-
Wall_600	600	$10 \rightarrow 1/10$[b]	instant	2-D	90°
Wall3d_600	600	$10 \rightarrow 1/10$[b]	instant	3-D	90°
L10_900	900	0.1	instant	2-D	90°
H10_900	900	10	instant	2-D	90°
Guitar	1500	$10 \rightarrow 0.45$[b]	instant	2-D	90°

[a] density ratio of the changed ambient density to the initial density.

[b] There are two regions where the ambient density changes.

the bow shock PWN produces a tail, along which an oblique shock occurs when its pressure is below the thermal pressure in the ambient medium. The bow shock tail can be described as a narrow cavity filled with relativistic exhaust from the pulsar. As discussed in Yoon et al. (2011), the shape of the cavity along the x-axis can be described analytically by using an adiabatic equation of state, the Bernoulli equation, and mass continuity:

$$P_x = a\,\rho_x^{\gamma} \tag{3.2}$$

$$\frac{1}{2}v_x^2 + \frac{\gamma}{(\gamma-1)}\frac{P_x}{\rho_x} = b \tag{3.3}$$

$$\pi\, w^2\, \rho_x\, v_x = c, \tag{3.4}$$

where w is the width of the cavity, and a, b, c are constants. The values of b and c can be expressed in terms of a:

$$b = \frac{\gamma}{\gamma-1} a^{1/\gamma} \left(\rho_0 v_*^2\right)^{1-1/\gamma}, \tag{3.5}$$

$$c = \frac{\gamma-1}{\gamma} \dot{E} a^{-1/\gamma} \left(\rho_0 v_*^2\right)^{1/\gamma-1}. \tag{3.6}$$

In (Yoon et al. 2011), the value of a was a free parameter due to the complexity in jet geometry, however the spherical shape of pulsar winds allow us to determine it from the pressure balance at the standoff position.

$$P_{\rm st,wind} = a\,\rho_{\rm st,wind}^{\gamma} = P_{\rm ram} = \rho_0\, v_*^2. \tag{3.7}$$

where $\rho_{\rm st,wind} = \dot{E}/(4\pi R_{\rm st}^2 v_{\rm wind}^3)$ is the wind density at the standoff position. As a result, a can be expressed as

$$a = \frac{\rho_0 v_*^2}{\rho_{\rm st}^{\gamma}} = \left(\rho_0 v_*^2\right)^{1-\gamma}\, v_{\rm wind}^{2\gamma}. \tag{3.8}$$

Using eqns. (3.2)-(3.8), w_1 can be obtained if we assume the pulsar is moving supersonically (*i.e.* $P_x \ll \rho_0 v_*^2$):

$$w \simeq \left(\frac{1}{2\pi^2}\right)^{1/4} \left(\frac{\gamma-1}{\gamma}\right)^{3/4} \dot{E}^{1/2}\, v_{\rm wind}^{-1/2} \left(\rho_0 v_*^2\right)^{1/2\gamma-1/2}\, P_x^{-1/2\gamma} = A\, P_x^{-1/2\gamma}. \qquad (3.9)$$

The pressure can be calculated by the jump conditions for an oblique shock [detailed derivation is included in eqns.(13)-(18) in Yoon et al. (2011)], and the differential equation for the width can be expressed as

$$\frac{dw}{dx} = \left(\frac{\gamma}{2}\right)^{-1/2} {\mathcal{M}_0}^{-1} \left[\frac{(w/A)^{-2\gamma}}{P_0} - 1\right] \left[\frac{\gamma+1}{P_0}\left(\frac{w}{A}\right)^{-2\gamma} + \gamma - 1\right]^{-1/2}, \qquad (3.10)$$

where P_0 is the ambient pressure and $\mathcal{M}_0 = v_*/\sqrt{\gamma\, P_0/\rho_0}$ is the Mach number of the pulsar relative to the ISM. Integrating eq. 3.10 yields the analytic shape of the bow shock and the neck from the physical properties (ambient density, ambient pressure, spin-down loss energy rate, velocity of the pulsar, wind velocity, and adiabatic index of the pulsar wind), and this is consistent with our numerical results (Figure 3.1). This semi-analytic solution helps us to understand the morphological evolution of a bow shock head and a trailing neck when the pulsar moves the medium in which the density changes gradually. If the ambient density increase gradually along the pulsar's passage, the ram pressure becomes stronger against internal pressure of the neck. Thus, the neck width in analytic lines in Figure 3.1 becomes thinner in the case. On the contrary, if the ambient density decreases, the bow shock and the neck becomes wider. We will apply this analysis to the Guitar Nebula's head in §3.4.1.1.

3.3.2 Density Discontinuity

High spatial velocity of a pulsar undergoes ram pressure of the ambient medium, producing a bow shock and a trailing neck. The smooth variation of the ambient

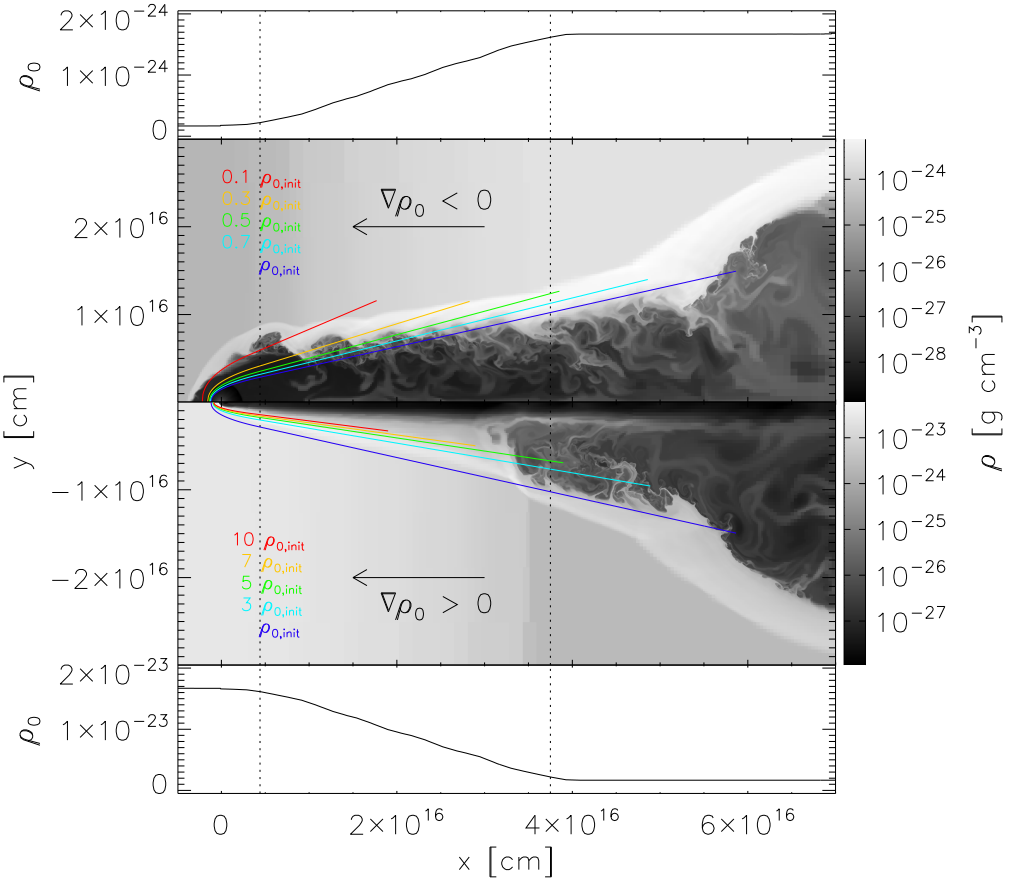

Fig. 3.1. — : Density contour map of the PWN head when the pulsar passes through either 10 fold increase (upper) or 1/10 fold decreased (lower) in ambient density. The top and bottom plots show the smooth variation of the ambient density with the transition width of 5×10^{17} cm (L10br_600 & H10br_600 in Table 3.1). The transition places were noted by vertical dashed lines. The colored lines indicate analytic solutions with different ambient densities.

density changes morphology of the bow shock and the neck, but it does not produce bubbles. We carried out 2-D hydrodynamic simulations to test if a bubble forms when the pulsar passes the medium in which the density changes sharply (i.e. density discontinuity). For this study, we set the discontinuity perpendicular to the pulsar's velocity.

When the pulsar encounters the low density medium, the standoff distance increases (eq. 3.1) and the bow shock becomes wider. The increase is extremely rapid, producing a bubble at the discontinuity. Figure 3.2 shows that the formation and the evolution of a bubble processes in same way between pulsar's initial explosion and its encountering a low density discontinuity. In early stage, the expansion velocity of the bubble is larger than the pulsar's spatial velocity, thus the pulsar is inside the bubble. In this time, the isotropic pulsar wind generates spherical bubble. The expansion velocity slows down, and the pulsar breaks out of the bubble at $t_{\rm break}$, which can be expressed as

$$t_{\rm break} = \eta^{1/2} \left(\frac{\dot{E}}{\rho_0} \right)^{1/2} v_*^{-5/2}. \tag{3.11}$$

After then, the pulsar's wind interacts with ISM producing bow shocks and trailing necks. One difference between two cases is that the bubble from the pulsar's initial explosion is exactly spherical, but the bubble, which is produced when the pulsar encounters a low density discontinuity, is flattened at the side of discontinuity. It is because the higher density in upstream medium exerts the higher ram pressure on the bubble.

Figure 3.4 shows a well-developed double-bubble structure behind the bow shock head. The first bubble was originated from initial launch of the pulsar wind, and the second bubble was generated when the pulsar encountered the discontinuity.

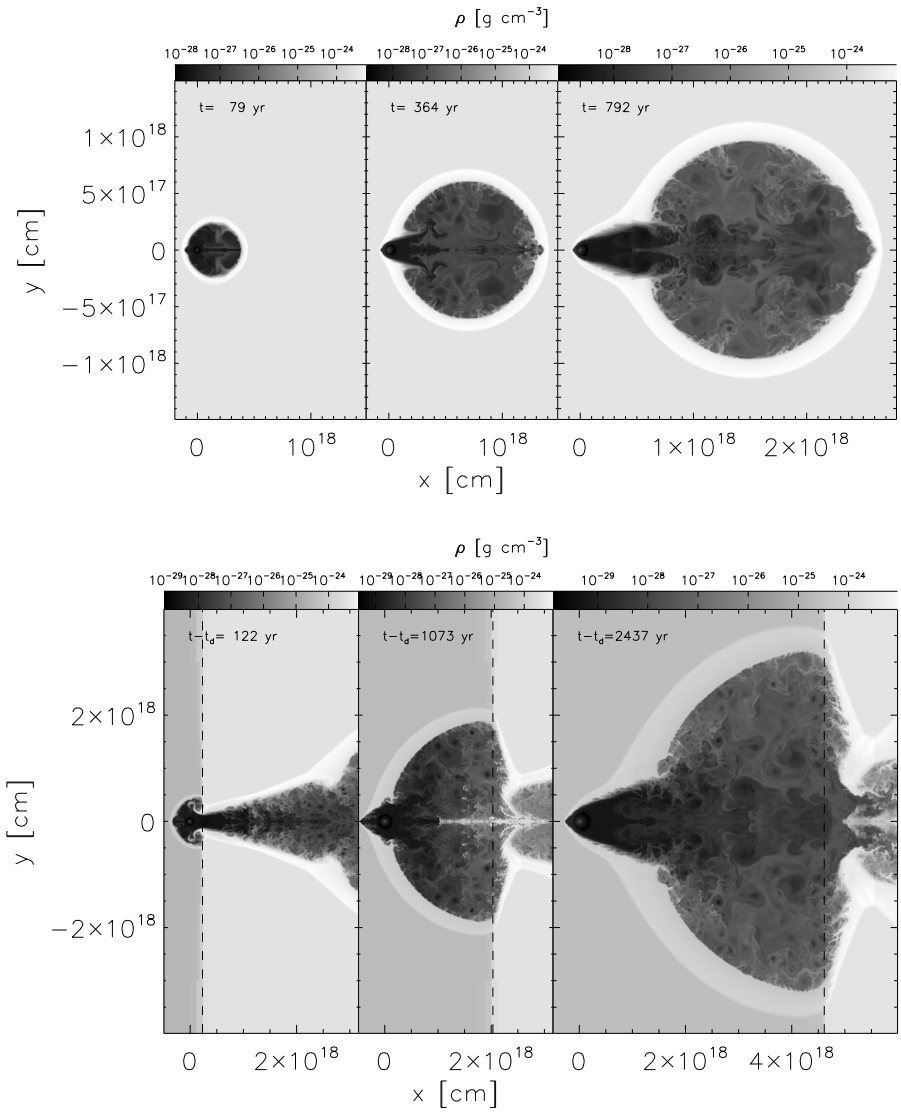

Fig. 3.2. — : Density contour maps of the evolution of expanding bubbles from the initial explosion (upper panel) and from the density discontinuity (lower panel). The vertical dashed lines (lower) indicate the location of the discontinuity. The ambient densities are $\rho_0 = 1.67 \times 10^{-24}\,\mathrm{g\,cm^{-3}}$ (upper), and $\rho_0 = 1.67 \times 10^{-24} \rightarrow 1.67 \times 10^{-25}\,\mathrm{g\,cm^{-3}}$ (lower). The pulsars are still inside the bubbles in left most plots, and break out of the bubbles in middle plots, and interact with ISM producing bow shocks in right most plots.

Note that the protrusion occurs in the right side of the first bubble. This is a 2-D numerical artifact that is caused by the exaggerated downstream flows along x-axis (i.e. y=0), hitting to the bubble edge. In the 3-D test run, this protrusion disappears. However, the effects of this structure on the evolution of the bubble is negligible. The white cross indicates the location of the pulsar, and the black circles represent the expanding bubbles in the analytic model (Castor et al. 1975),

$$R_b(t) = \eta^{1/5} \left(\frac{\dot{E}}{\rho_0} \right)^{1/5} t^{3/5}, \tag{3.12}$$

where η is a constant that equals $125/154\pi$, which is derived by the assumption that the gas is swept-up into a cold, thin shell.

We carried out simulations with the pulsar's proper speeds of 300, 600, and 900 $\mathrm{km\,s^{-1}}$. Figure 3.3 shows the evolution of the expanding bubbles with time. The solid line represents the analytic model in eq. 3.12, and each filled region represents the location of the shell of the bubble. Note that in this work, we neglect cooling, broadening the shell at the surface of the bubble. If cooling is taken into account, the shell thins, but the overall dynamic evolution is not affected (Yoon et al. 2011). For all cases, the evolving bubbles in the simulations are consistent with the analytic model.

If multiple bubbles are observed in a bow shock PWNe, we can constrain the parameters from the bubble's geometry. In our simulations, we fixed the separation between the initial position of the pulsar and the density discontinuity to be $l_{sep} = 4.12 \times 10^{18}\,\mathrm{cm}$. This implies that if the pulsar moves faster, it reached the discontinuity in a shorter time, thereby the size ratio of the second bubble to the first bubble becomes larger compared to the case of slowly moving pulsars. The ratio

of the bubble size can be derived from the ratio in eq. 3.12,

$$\begin{aligned} R_{b2}(t)/R_{b1}(t) &= \left(\frac{\rho_{0,1}}{\rho_{0,2}}\right)^{1/5}\left(1-\frac{t_d}{t}\right)^{3/5} \\ &= \left(\frac{\rho_{0,1}}{\rho_{0,2}}\right)^{1/5}\left(1-\frac{l_{\rm sep}}{t\,v_*}\right)^{3/5}, \end{aligned} \tag{3.13}$$

where $\rho_{0,1}, \rho_{0,2}$ are the ambient densities surrounding the first and second bubble, respectively, and t_d is time when the pulsar encounters the density continuity. The time relates with the separation between the two bubbles using $l_{\rm sep} = t_d \times v_*$. This robust expression is useful for estimating the density changes in the medium around the mulitple bubbles.

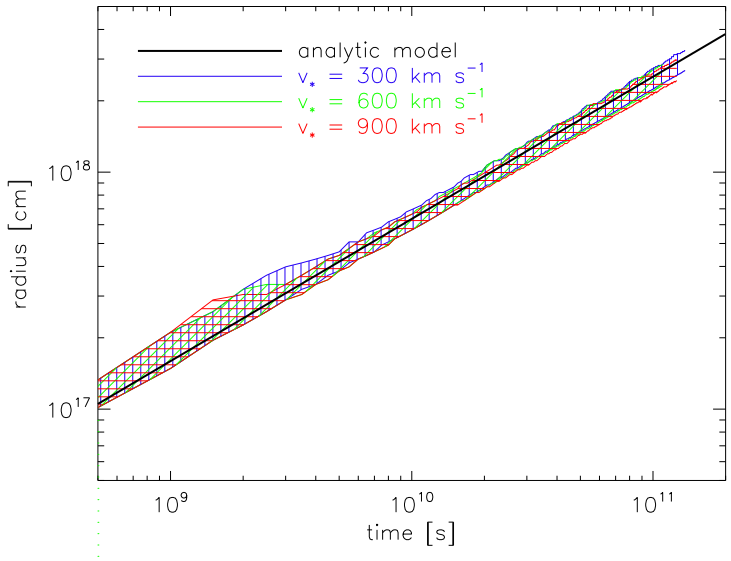

Fig. 3.3. — : The time evolution of the expanding bubbles. The black solid line represent the analytic solution, and the colored areas represent the bubble shells from the simulation results with $v_* = 300,\ 600,\ 900\,\mathrm{km\,s^{-1}}$

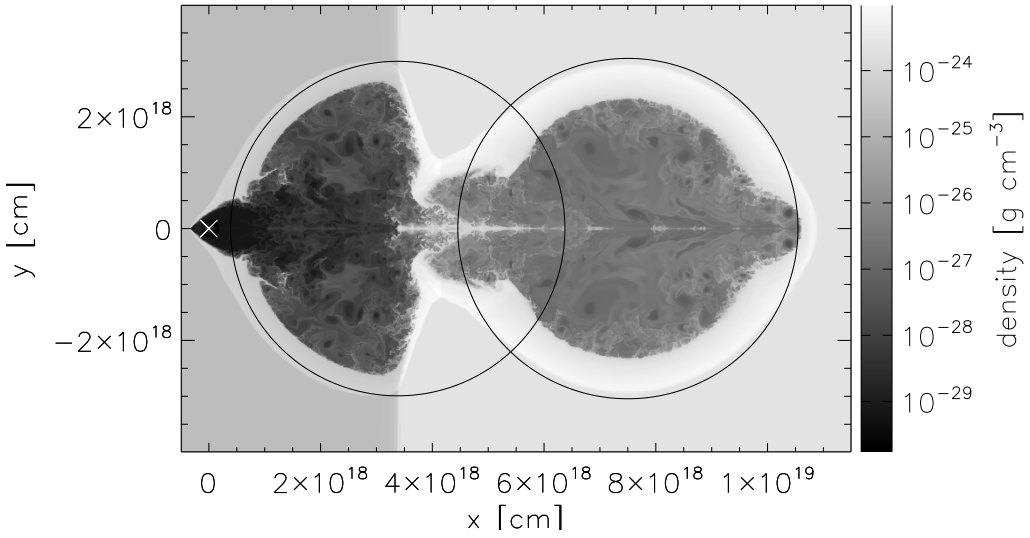

Fig. 3.4. — : The density contour map when the pulsar penetrates the density discontinuity toward lower ambient density. The black circles are analytic models of the bubbles. White cross indicates the location of the pulsar.

3.4 Discussion

3.4.1 Guitar Nebula

The sets of H_α bow shocks and multiple bubbles far behind has been detected in Guitar Nebula, produced by the relativistic wind from the high-velocity pulsar, PSR B2224+65, interacting with medium (Figure 3.5). We use the Guitar Nebula to test the effects of non-uniform density on the dynamical evolution of bow shock PWNe.

We adopt the model parameter of the Guitar nebula from van Kerkwijk & Ingle (2008, and references therein): $\dot{E} = 10^{33}\,\mathrm{ergs\,s^{-1}}$, $v_* = 1.5 \times 10^8\,\mathrm{cm\,s^{-1}}$. The spin-down loss energy of the nebula is a few orders of magnitude lower than that of typical H_α bow shock pulsar nebulae (Gotthelf 2004). However, the extremely fast

motion of the pulsar in the Guitar nebula enables to produce the visible bow shock features despite of such low $\dot{E}$ and low density.

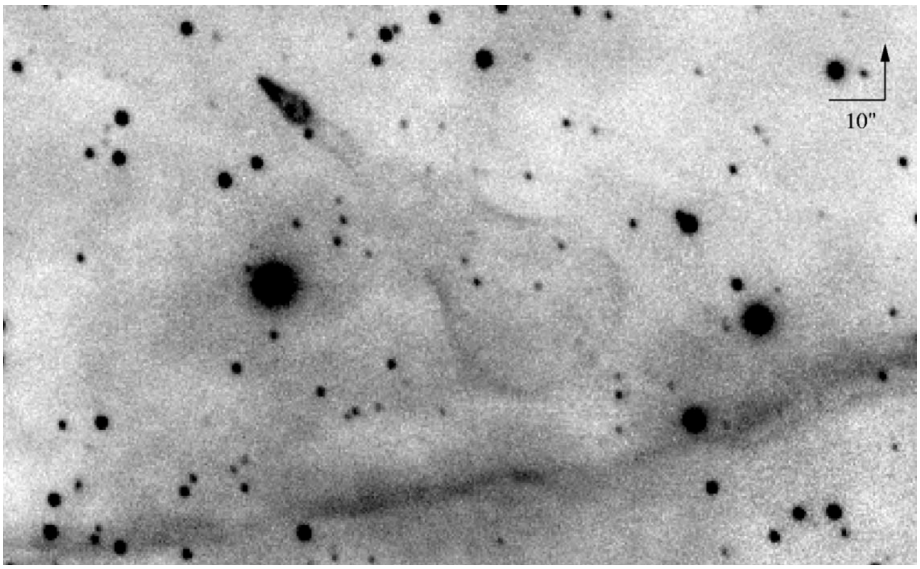

Fig. 3.5. — : Guitar Nebula in H_α, imaged with the 5m Hale Telescope at Palomar Observatory (Chatterjee & Cordes 2002).

3.4.1.1 bow shock and neck

Chatterjee & Cordes (2004) observed morphological changes of Guitar Nebula's head in H_α emission for two epochs spaced by 7 years (1994, 2001). Under the assumption of a momentum-conserving bow shock model (Wilkin 1996), they have modeled the shock front, concluding that the ambient density at the nebula tip should decrease by $n_{\rm A}(2001)/n_{\rm A}(1994) \approx 0.7$, where $n_{\rm A}$ is a number density of the surrounding medium. However, this work is the purely analytic approach, so time-dependent simulations of the shock fronts with density fluctuation is required to support the result.

We carried out numerical simulations to understand how bow shock and trail-

ing neck evolve if the pulsar moves through the medium with either gradual increase or decrease in density. Figure 3.1 shows that if the pulsar moves through decreased-density medium (*i.e.*, $\nabla\rho_0 < 0$), the standoff radius becomes larger, and the shape of bow shock becomes rounder, producing wider neck. On the contrary, if the pulsar moves through increased-density medium (*i.e.*, $\nabla\rho_0 > 0$), the standoff position becomes closer to the pulsar, and the neck is more suppressed than that in the initial density medium. The analytic lines describe the change of shock fronts along the density variation in the medium.

Figure 3.6 shows that morphologies of the bow shocks and necks are apparently different between three cases: $\nabla\rho_0 < 0$, $\nabla\rho_0 > 0$, and constant ρ_0. We found that the rounder shape in the tip of the bow shock head and the flattened neck in case of $\nabla\rho_0 < 0$ have a good agreement with observed morphology of the Guitar head at 2001 [See Figure 2 in (Chatterjee & Cordes 2004)], indicating that the pulsar likely moves decreased-density medium during the epochs. Under the assumption of no time-dependent variation in the spin-down loss energy, spatial velocity, and pulsar wind velocity, we can obtain the density ratio in the medium by using eq. 3.1, into which we plug the ratio of standoff data, $\theta_{0,2001}/\theta_{0,1994} \approx 1.25$, where θ_0 is a modeled standoff angle (Chatterjee & Cordes 2004). The resultant density ratio, $\rho_{0,2001}/\rho_{0,1994}$, is 0.64 which is consistent with Chatterjee & Cordes (2004).

3.4.1.2 Guitar Body

The origin of the multiple bubbles in Guitar Nebula has been elusive. As we discussed in § 3.3.2, an expanding bubble can be produced if the pulsar encounters density discontinuity at which the density sharply decrease.

We adopt the angular separation and angular size of the bubbles that were

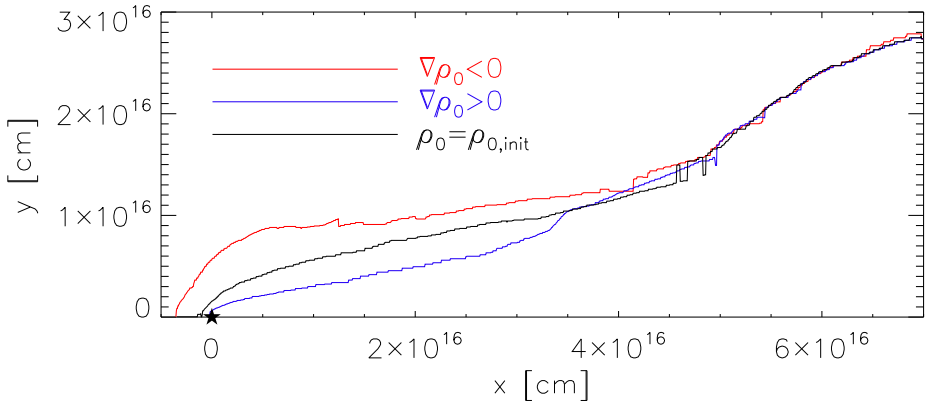

Fig. 3.6. — : The comparison of bow shock head. The red, blue and black represent the bow shock and the trailing neck from the model of L10br_600, H10br_600, and Uniform_600, respectively. The black star symbol indicates the location of the pulsar.

reported by van Kerkwijk & Ingle (2008). We assumed that the distance is $d = 1.8\,\mathrm{kpc}$, inferred by the dispersion measure and the NE2001 electron density model of Cordes & Lazio (2002), yielding the separation length from the pulsar to the first and second bubbles (named by the birth sequence) can be calculated to $l_{\mathrm{b1}} = 1.75 \times 10^{18}\,\mathrm{cm}$ and $l_{\mathrm{b2}} = 1.1 \times 10^{18}\,\mathrm{cm}$, respectively. Given the pulsar proper velocity, $v_* = 1.5 \times 10^8\,\mathrm{cm\,s^{-1}}$, we expect that the first and second bubbles were born 370 and 233 years ago, respectively, while the pulsar passes a non-uniform density medium.

In order to reproduce multiple bubbles in the Guitar Nebula, we calculated the change of ambient density around the bubbles. Using the energy-supported expanding bubble model (eq. 3.12), the ratio of the ambient density around the second bubble (ρ_2) and first bubble (ρ_1) can be expressed as,

$$\frac{\rho_2}{\rho_1} = \left(\frac{R_{\mathrm{b1}}}{R_{\mathrm{b2}}}\right)^5 \left(\frac{l_{\mathrm{b2}}}{l_{\mathrm{b1}}}\right)^3, \tag{3.14}$$

where R is the bubble radius Given observed parameters (van Kerkwijk & Ingle

2008), the ratio of the bubble radius is $R_{\rm b1}/R_{\rm b2} = 16''/9'' \approx 1.78$, and the ratio of the separation is $l_{\rm b1}/l_{\rm b2} = 65''/41'' \approx 1.58$. This implies that the density around the second bubble should be 4.5 times higher than that around the first bubble. Since the higher density medium in pulsar's passage does not produce a bubble, the presence of density wall , in which the density is higher than ρ_2, is required in this case. However, in this model, the H_α emission in the second bubble is brighter than that in the first bubble due to the enhanced ambient density. This is inconsistent with the observed features.

We propose a possible scenario for producing the guitar shape in the nebula from a density variation in the medium. In this scenario, the density changes in three times: (1) When the pulsar passes through a low density discontinuity, it produces a first bubble. (2) Then, the pulsar, which breaks out of the first bubble, moves along smooth gradient toward a reduced density, the neck becomes wider, producing bubble-like structure between the pulsar and the first bubble. (3) Then, the pulsar passes through high density medium, producing a narrow neck.

We carried out 2-D hydrodynamic simulation to test this scenario. The variation of an ambient density is shown in upper plot of Figure 5.2. The density contour map in Figure 5.2 shows that this model reproduces the guitar body and the narrow neck. In order to compare this result to observed H_α emission, under the assumption of collisional equilibrium, we calculated the emission from our result. The ionization balance in the shocked gas was calculated by the MAPPING III code (Sutherland & Dopita 1993). The temperature of the shocked shell is above 10^6 K, thus the gas is nearly fully ionized. The right panel of Figure 5.2 shows the surface brightness in H_α for the model. The H_α emission of the body is dim due to the low density in the

medium, which is consistent with the observed features.

The first bubble is flattened toward the discontinuity because the high density suppresses the expansion of bubble in the region. However, its shape can project into a circle if the viewing angle, $\theta_{\rm LOS}$, between the pulsar velocity vector and the line of sight (LOS) varies (see right panel of Figure 5.2). Although the pulsar velocity vector is likely perpendicular to the LOS due to the pulsar's high spatial velocity, the viewing angle is not clear yet (Chatterjee & Cordes 2004). In our model, $\theta_{\rm LOS} = 60°$ is a best fit to the observed shape.

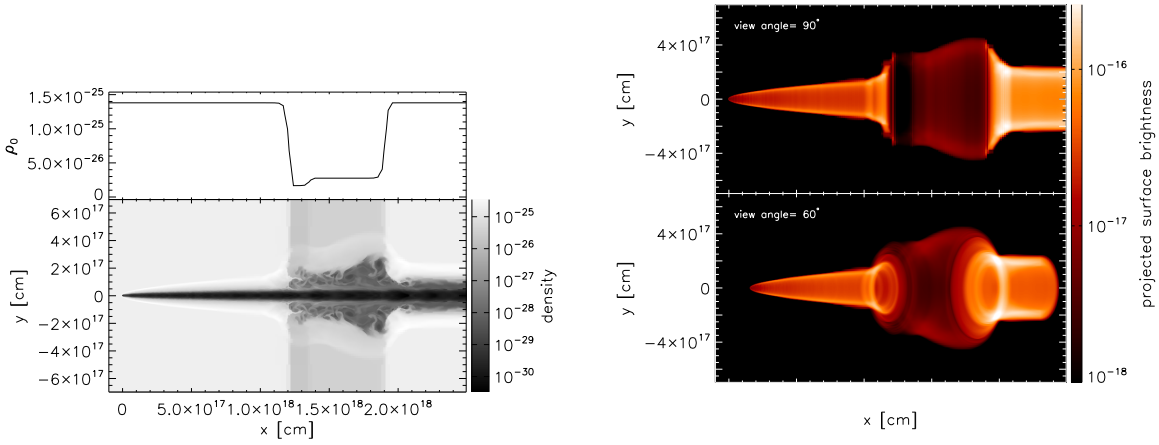

Fig. 3.7. — : Left panel:Density contour map for the Guitar Nebula model. The variation of ambient density was described in upper plot. Right panel: Projected H_α emissions with the viewangle of 90°(upper) and 60°(lower).

3.4.2 Asymmetric Shape of Bow Shock

The H_α-emitting bow shock nebula powered by the nearby millisecond pulsar J2124-3358 has a highly asymmetric shape in its head around the pulsar's velocity vector (Gaensler et al. 2002). This shape can not be explained by the interaction of an isotropic pulsar wind with a homogeneous ambient medium. Gaensler et al.

(2002) argued that the asymmetric bow shock structure is caused by the combination of three components: a density gradient in the ISM, a bulk flow in the ambient medium, and an anisotropy in the pulsar wind. However, in their semi-analytic models for the structure, an inclination angle between the pulsar's velocity vector and the density discontinuity cannot be taken into consideration due to the complexity. In the models, the density gradient was either perpendicular or parallel.

To study the effect of the inclination angle, we carried out a 3-D hydrodynamic simulation for a bow shock PWN, penetrating the density discontinuity with the angle of 45° (L10_600_45deg in Table 3.1). In the model, we assumed that the pulsar wind is isotropic, and there is no bulk flow in the medium. As discussed in §3.3.2, the tip of the bow shock head inflates as the pulsar passes through the density discontinuity at which the density decrease. The inclined discontinuity brakes the symmetry, and a kink-like structure occurs at the lower side of the bow shock head (see the arrow in Figure 3.8). The kink-like structure and the asymmetric shape of the bow shock from our result are apparently similar with the morphology of the pulsar J2124-3358 [Figure 1 in Gaensler et al. (2002)]. Consequently, we argue that the inclined density-discontinuity to the pulsar's velocity vector plays a significant role in producing the asymmetric features, although an anisotropic pulsar wind is also important(Vigelius et al. 2007).

3.4.3 Caveats

Pulsar winds are magnetized and relativistic outflows, indicating that relativistic magnetohydrodynamic (MHD) treatment is required in studying the internal flow structure and the emission properties of bow shock PWNe (Bernstein & Hughes 2009). However, even for the fastest known pulsar, the pulsar velocity is of 2 orders

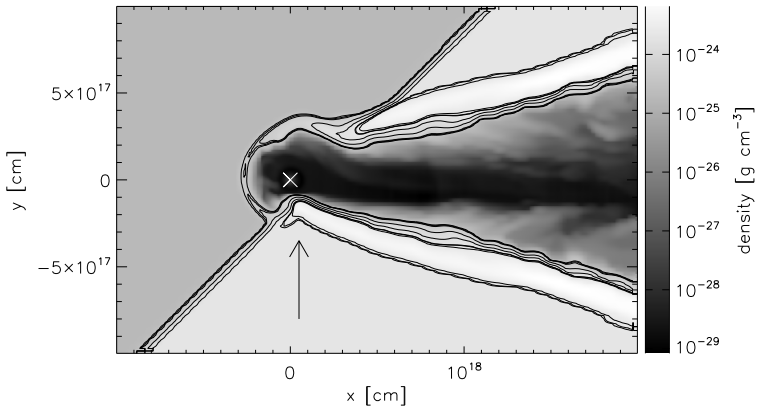

Fig. 3.8. — : Density contour map that the pulsar encounters density discontinuity which has inclination angle of 45° to the pulsar's velocity vector. The white cross indicates the location of the pulsar, and the black arrow points the kink-like structure.

of magnitude less than the speed of light, which is non-relativistic. Moreover, an expansion speed of bubbles is non-relativistic. Bucciantini et al. (2005) argued that the structure of the external layer of shocked medium does not change significantly with the pulsar wind magnetization factor.

We carried out some subsets of runs with special relativistic hydrodynamic treatment, developed in FLASH 2, to compare with our results with hydrodynamic simulations. In these test runs, we varied the velocity of the pulsar wind ($v_{\rm wind}$ = 0.33c, 0.6c, 0.9c, 0.99c) for both hydrodynamics and relativistic hydrodynamics runs, and otherwise we used identical parameters. Figure 3.9 shows the evolution of bubbles, which the energy is injected by pulsar wind. For various pulsar wind velocities, the trends of the bubble expansion are consistent with analytic solution (red solid line) from eq. 3.12. The error is about 8% for the extreme case ($v_{\rm wind} = 0.99c$), and is less then 2% for rest cases.

The relativistic MHD treatment is out of scope in this study. As we discussed,

the relativistic effect is negligible in the evolution of bubbles. Also, Bucciantini et al. (2005) argued that the variation of a pulsar wind magnetization does not change the shock layer significantly apart from the very head of the nebula. Consequently, although our hydrodynamic runs has a limit to study the relativistic magnetized pulsar wind, our study is valid in understanding the dynamical evolution of global structures around bow shock PWNe.

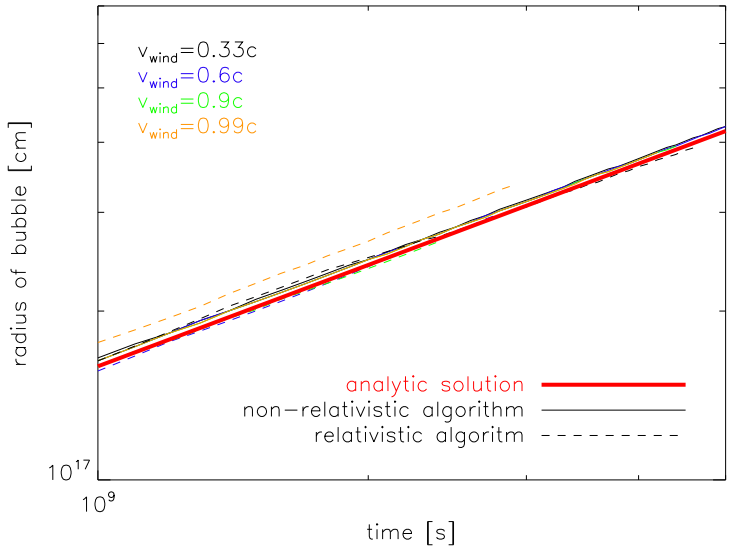

Fig. 3.9. — : The time evolution of the expanding bubbles. The red solid line represents the analytic model, and black lines represents the inner radius of the bubbles from the simulations. The solid black lines are hydrodynamic results, and the dashed black lines are relativistic hydrodynamic results.

3.5 Conclusion

When a pulsar moves with supersonic speed, it produces a bow shock and a trailing neck. In order to study the effect of inhomogeneous ambient density on bow

shock pulsar wind nebulae, we performed 2-D/3-D hydrodynamic simulations.

We found that if the pulsar passes through a density gradient in the medium which is decreasing, the bow shock becomes wider. As a result, overall shape of the trailing neck becomes more flattened. However, if the density gradient in the medium is increasing, the bow shock becomes narrower. We derived analytic formula for the shape of the bow shock head and the trailing neck as a function of ambient density and pulsar wind parameters. We applied this analysis into the observed change in the shape of the Guitar Nebula head, and concluded that the pulsar in the nebula moves through a density-decreasing medium.

If the pulsar encounters density discontinuity, at which the density decreases, the standoff distance increases rapidly, producing a bubble. We reproduced the observed guitar shape in the Guitar Nebula from a series of density changes in the medium. The bubble, which is produced at the discontinuity, is flattened toward the discontinuity because high density medium suppresses the expansion of the bubble. We showed that this flattened shape becomes rounder as the viewing angle between the pulsar's velocity vector and the LOS increases. The model reproduces a guitar body and a narrow neck between the body and the pulsar.

References

Bell, J. F., Bailes, M., Manchester, R. N., Weisberg, J. M., & Lyne, A. G. 1995, ApJ, 440, L81

Bernstein, J. P., & Hughes, P. A. 2009, Journal of Computational Physics, 228, 6212

Blondin, J. M., Mezzacappa, A., & DeMarino, C. 2003, ApJ, 584, 971

Bucciantini, N., Amato, E., & Del Zanna, L. 2005, A&A, 434, 189

Burrows, A., & Hayes, J. 1996, Physical Review Letters, 76, 352

Castor, J., McCray, R., & Weaver, R. 1975, ApJ, 200, L107

Chatterjee, S., & Cordes, J. M. 2002, ApJ, 575, 407

—. 2004, ApJ, 600, L51

Colella, P., & Woodward, P. R. 1984, Journal of Computational Physics, 54, 174

Cordes, J. M., & Lazio, T. J. W. 2002, ArXiv Astrophysics e-prints, astro-ph/0207156

Cordes, J. M., Romani, R. W., & Lundgren, S. C. 1993, Nature, 362, 133

Cox, D. P. 2005, ARA&A, 43, 337

Deshpande, A. A. 2000, MNRAS, 317, 199

Faison, M. D., & Goss, W. M. 2001, AJ, 121, 2706

Fryxell, B., Olson, K., Ricker, P., et al. 2000, ApJS, 131, 273

Gaensler, B. M., Jones, D. H., & Stappers, B. W. 2002, ApJ, 580, L137

Gaensler, B. M., & Slane, P. O. 2006, ARA&A, 44, 17

Gaensler, B. M., van der Swaluw, E., Camilo, F., et al. 2004, ApJ, 616, 383

Gotthelf, E. V. 2004, in IAU Symposium, Vol. 218, Young Neutron Stars and Their Environments, ed. F. Camilo & B. M. Gaensler, 225

Hanke, F., Marek, A., Müller, B., & Janka, H.-T. 2012, ApJ, 755, 138

Jones, D. H., Stappers, B. W., & Gaensler, B. M. 2002, A&A, 389, L1

Kennel, C. F., & Coroniti, F. V. 1984, ApJ, 283, 694

Kulkarni, S. R., & Hester, J. J. 1988, Nature, 335, 801

Manchester, R. N., Hobbs, G. B., Teoh, A., & Hobbs, M. 2005, AJ, 129, 1993

Michel, F. C. 1969, ApJ, 158, 727

Noutsos, A., Schnitzeler, D. H. F. M., Keane, E. F., Kramer, M., & Johnston, S. 2013, MNRAS, 430, 2281

Patat, F., Cox, N. L. J., Parrent, J., & Branch, D. 2010, A&A, 514, A78

Sagert, I., & Schaffner-Bielich, J. 2008, A&A, 489, 281

Sutherland, R. S., & Dopita, M. A. 1993, ApJS, 88, 253

van Kerkwijk, M. H., & Ingle, A. 2008, ApJ, 683, L159

van Kerkwijk, M. H., & Kulkarni, S. R. 2001, A&A, 380, 221

Vigelius, M., Melatos, A., Chatterjee, S., Gaensler, B. M., & Ghavamian, P. 2007, MNRAS, 374, 793

Wilkin, F. P. 1996, ApJ, 459, L31

Yoon, D., Morsony, B., Heinz, S., et al. 2011, ApJ, 742, 25

Chapter 4

Global Simulations of the Interaction of Microquasar Jets with a Stellar wind in High-Mass X-ray Binaries

This chapter has previously appeared in The Astrophysical Journal

D. Yoon, & S. Heinz, 2015, vol. 801, p. 55

Abstract

Jets powered by high-mass X-ray binaries must traverse the powerful wind of the companion star. We present the first global 3D simulations of jet-wind interaction in high-mass X-ray binaries. We show that the wind momentum flux intercepted by the jet can lead to significant bending of the jet and that jets propagating through a spherical wind will be bent to an asymptotic angle ψ_∞. We derive simple expressions for ψ_∞ as a function of jet power and wind thrust. For known wind parameters, measurements of ψ_∞ can be used to constrain the jet power. In the case of Cygnus X-1, the lack of jet precession as a function of orbital phase observed by the VLBA can be used to put a lower limit on the jet power of $L_{\rm jet} \gtrsim 10^{36}\,{\rm ergs\,s^{-1}}$. We further discuss the case where the initial jet is inclined relative to the binary orbital axis. We also analyze the case of Cygnus X-3 and show that jet bending is likely negligible unless the jet is significantly less powerful or much wider than currently thought. Our numerical investigation is limited to isotropic stellar winds. We discuss the possible effect of wind clumping on jet-wind interaction, which are likely significant, but argue that our limits on jet power for Cygnus X-1 are likely unaffected by clumping unless the global wind mass loss rate is orders of magnitude below the commonly assumed range for Cyg X-1.

4.1 Introduction

X-ray binaries consist of a compact object, such as a neutron star (*e.g.*, Sco X-1, Hjellming et al. 1990) or a black hole (*e.g.* Cygnus X-1, Orosz et al. 2011; Cygnus X-3, Zdziarski et al. 2013), accreting mass from a companion. In certain spectral states, the accretion flow near the compact object generates powerful, collimated jets (Mirabel & Rodríguez 1999; Gallo et al. 2005). These jets appear remarkably similar to the jets produced by supermassive black holes (SMBH) in active galactic nuclei (AGN) in morphology, spectral properties, and energetics (when set in relation to the overall energy released by accretion).

The mostly featureless non-thermal spectra of relativistic jets limit quantitative analysis of jet properties to relatively coarse estimates. However, the propagation of jets and their interaction with the environment offers a very powerful way to study jet properties that complements direct studies of jets themselves. The observations of cavities in galaxy clusters by the *Chandra* X-ray Telescope offer an example of how jet-environment interactions can be used to constrain the properties of large samples of AGN jets (e.g. McNamara & Nulsen 2007, and references therein).

A sub-class in the study of jet-environment interactions involves cases where the accreting black hole launching the jets is moving relative to the surrounding medium. In AGN, when the black hole is moving with considerable speed with respect to the environment, the radio emitting jets are swept backward by ram pressure, generating a bow shock ahead of the moving black hole. AGN jets that show bent morphology are often called "bent doubles" or tailed radio sources (Begelman et al. 1979; Freeland

& Wilcots 2011; Morsony et al. 2013).

It has been suggested that a subset of low mass x-ray binaries (LMXBs) that move through the ISM at high speed due to the kick velocity the LMXB received in the supernova explosion should also exhibit bow shocks and trailing neck structures (Heinz et al. 2008; Wiersema et al. 2009; Yoon et al. 2011), very similar to the case of bent-double AGN sources.

However, an aspect that makes jet propagation in X-ray binaries fundamentally different from AGN jets is the presence of the companion star. The early type companion stars of high mass X-ray Binaries (HMXBs) drive powerful winds in the vicinity of the compact object, which are often the source of accretion in these objects. The wind mass loss rates of the OB-type donor star can be substantial: $\dot{\mathrm{M}}_{\mathrm{wind}} \sim 10^{-7} - 10^{-5}\,\mathrm{M}_{\odot}\,\mathrm{yr}^{-1}$. The stellar wind dominates the HMXBs' circum-binary environment compared to any winds launched by the accretion flow. In this work, we study the dynamics and evolution of the jets affected by spherical stellar winds from OB-type donor stars in HMXBs. A subset of HMXB systems consist of a Wolf-Rayet star in orbit with a black hole (*e.g.* Cygnus X-3 Martí et al. 2001; Zdziarski et al. 2013); the mass-loss rate from Wolf-Rayet stars is even higher than that from OB-type stars. Moreover, the Wolf-Rayet star in Cygnus X-3 is tidally locked to the 4.8-h orbital period, resulting in a considerable equatorial enhancement of the mass-loss rate (van Kerkwijk 1993). An investigation of non-spherical and highly-flattened winds is beyond the scope of this study. While we briefly discuss the case of Cygnus X-3 under the assumption of a spherical wind, we plan to discuss the effects of non-spherical winds in a future paper.

HMXB winds are not simple. For example, they are likely clumpy (Owocki

et al. 1988; Oskinova et al. 2012), like winds generated by other high-mass stars. The interaction of a microquasar jet with clumpy wind medium has been studied in 3D simulations by Perucho & Bosch-Ramon (2012), which we will refer to as P12 hereafter, who show that clumping can significantly increase jet disruption. Moreover, even on average, they are not spherically symmetric due to the gravitational focusing by the compact object and Coriolis and centrifugal effects due to orbital motion (Friend & Castor 1982; Miller et al. 2005; Hadrava & Čechura 2012). In addition, the wind can be ionized by X-rays from the accretion flow, reducing or eliminating line driving and stalling the wind (Gies et al. 2008). If the X-ray flux is high enough to excite the outer layer of the star, a thermally driven wind may replace the quenched radiatively driven wind. At the current time, it is not clear whether the illuminated side of the wind would suffer from the same line-driving instability that generates clumps in regular massive star winds.

In this pilot paper, we will neglect some of the more poorly understood complications likely present in binary winds and instead treat the wind as a radiatively driven wind that is isotropic at the surface of the companion (following, e.g. Castor et al. 1975). This will allow us to isolate the fundamental differences in jet propagation in the presence of a wind compared to jets propagating into uniform medium. We will discuss the effects of some of the likely complications in §4.4.8. The likely most important caveat is the potential clumpiness of the wind; in that sense, the global simulations presented below should be considered a complementary approach to the detailed 3D jet-clump simulations presented in P12.

In §2, we present the numerical setup and the code used in our parameter study of jet-wind interaction. In §3 we discuss the results of the simulations. In §4,

we compare the numerical results with analytic expressions derived for the limiting case of small deflection angles and apply our model to the HMXBs Cygnus X-1 and Cygnus X-3. In §5 we summarize our results.

4.2 Technical Description

4.2.1 The FLASH Code

Simulations were performed with the FLASH 3.3 hydrodynamics code (Fryxell et al. 2000), which is a Message Passing Interface(MPI)-parallelized, modular, block-structured adaptive mesh refinement code. We employ the non-relativistic unsplit mesh solver, which solves the Riemann problem using an unsplit staggered mesh scheme on a three dimensional Cartesian grid (Lee & Deane 2009).

4.2.2 The Wind and Jet Nozzles

Both the jet and the wind injection are modeled as inflow-boundary conditions on an interior portion of the grid (we will refer to the regions excluded from the hydro-dynamic integration and instead treated as an interior boundary as "nozzles" following Heinz et al. 2006).

The jet nozzle has a cylindrical shape with inflow boundary conditions at the surface, injecting a bipolar outflow with a prescribed energy, mass, and momentum flux to match the parameters we choose for the jet. For reasons of numerical stability, we inject a slow lateral outflow from the side walls of the cylinder with negligible mass and energy flux in order to avoid complete evacuation of zones adjacent to the nozzle due to the large velocity divergence along the jet axis.

The stellar wind nozzle is modeled as a spherical boundary with inflow bound-

ary conditions matching the desired wind parameters. We evolve the simulation with only the stellar wind present for one full orbital period to establish a stable, self-consistent wind profile before switching on the jet nozzle.

The equation of state is assumed to be adiabatic, tracking two separate phases of the fluid (each represented by a separate passive tracer fluid to distinguish wind and jet fluids during the computation and in post-processing). The wind gas is assumed to be a monatomic ideal gas with an adiabatic index of $\gamma = 5/3$. The internal composition of jets is currently unknown, however, it is reasonable to assume that they are strongly magnetized and that a sizeable fraction of their internal energy is carried by relativistic electrons, given the observed synchrotron radiation. We investigate jets composed of fluids both with relativistic equation of state with $\gamma = 4/3$ and with a cold-gas equation of state with $\gamma = 5/3$ and present results in terms of an unspecified value of γ wherever possible.

Most simulations were performed using $\gamma = 4/3$, representing the equation of state for a gas with relativistic internal pressure, either from a fully tangled magnetic field (Heinz & Begelman 2000) or a relativistic component of the gas; since our simulations are sub-relativistic, a relativistic equation of state implies that the inertial density is dominated by cold particles (e.g., protons). A non-relativistic equation of state represents a jet with internal pressure dominated by non-relativistic thermal plasma. As we will show, our results are only moderately sensitive to the actual value of γ.

The gravitational fields of the black hole and the companion are modeled as point source potentials.

To allow for direct comparison with the analytic formulae we derive in §4.4.2,

most of the simulations presented in this paper do not include wind driving by radiation pressure. Instead, we assumed an asymptotic wind at the injection at the stellar surface, *i.e.*, a wind with terminal velocity v_∞ and at fixed mass flux of $\dot{\mathrm{M}}_{\mathrm{wind}} \sim 10^{-5}\,\mathrm{M}_\odot\,\mathrm{yr}^{-1}$, which is typical for OB stars (Puls et al. 2008).

Wind driving was incorporated in a sub-set of the simulations presented in this paper to test the sensitivity of our results against the assumption of an asymptotic radial wind. (See §4.4.3). For the radiatively driven wind, the initial velocity field follows the so-called β-law

$$v(r) = v_\infty(1 - r_0/r)^\beta, \tag{4.1}$$

where $v_\infty = 2,500\,\mathrm{km\,s^{-1}}$ is the wind terminal speed [chosen to match the wind parameters of typical OB-type stars (Puls et al. 2008)] and $r_0 = R_* x$, where R_* is the radius of the star and x is applied to avoid zero velocity and infinite density on the surface of the star. We set the stellar radius $R_* = 1.4 \times 10^{12}\,\mathrm{cm}$. The value of x can be expressed as $x = \left[1 - (v_*/v_\infty)^{1/\beta}\right] = 0.99$, where the wind surface velocity, v_*, is of the order of $10^6\mathrm{cm\,s^{-1}}$, which is the sound speed with $T_{\mathrm{eff}} \approx 30,000\,K$. However, due to the steep variation of density and pressure around the surface, there is a limit in performing a numerical calculation with such a high value of x. Alternatively, we set the value of $x = 0.95$, which was chosen to be high enough to maintain the initial wind profile from a typical OB-type star by iterative 1D simulations. The mass flux of the wind was fixed at the surface of the star (where density and velocity of the injected wind determine $\dot{\mathrm{M}}$ uniquely) and line driving was modeled using the Sobolev approximation (Castor 1974), such that the total line acceleration results in $g_{\mathrm{rad}} \propto \left(\frac{1}{\rho}\frac{dv_r}{dr}\right)^{\alpha_{\mathrm{CAK}}}$, where α_{CAK} is the parameter of the CAK model (Castor et al. 1975), typically depending on the effective temperature of the star. We choose a

value of $\alpha_{\rm CAK} = 0.64$ in our model corresponding to a typical OB-type star.

Our simulations are adiabatic and scale-free. In physical units chosen to approximately match the wind and binary properties of Cygnus X-1 and allow simulations to be completed within the available computational resources, the jet velocity was set to be $v_{\rm jet} = 3{\times}10^9\,{\rm cm\,s^{-1}}$, with an initial internal Mach number of $\mathcal{M}_{\rm jet,0} = 30$ at the base of the jet (the "nozzle"). To explore the dependence on Mach number, we ran a simulation at $\mathcal{M}_{\rm jet,0} = 10$ and otherwise identical parameters compared to our fiducial run with a jet power of $L_{\rm jet} = 10^{36}\,{\rm ergs\,s^{-1}}$. Note that the Mach number $\mathcal{M}_{\rm jet}$ varies along the jet given the adiabatic behavior of the fluid.

In order to resolve the hydrodynamics at the injection scale with at least 10 cells across the nozzle, we forced the jet nozzle to be at maximum refinement, resulting in an effective resolution of $4.7 \times 10^9\,{\rm cm} = 1.6 \times 10^{-3}\,a$, compared to an orbital separation of $a \approx 3 \times 10^{12}\,{\rm cm}$ for Cygnus X-1 (Gies & Bolton 1982). The radius of the jet nozzle is about $2.5 \times 10^{10}\,{\rm cm}$ and the full box size of the simulation is about $4 \times 10^{13}\,{\rm cm}$, centered on the center of mass of the binary.

We varied the jet power to span the range $L_{\rm jet} \approx 10^{35}$, 10^{36}, $10^{37}\,{\rm ergs\,s^{-1}}$, comparable to the range of uncertainty in the jet power of Cygnus X-1, $9 \times 10^{35} - 10^{37}\,{\rm ergs\,s^{-1}}$ (Gallo et al. 2005; Russell et al. 2007).

For the bulk of our simulations, the jet was injected in a direction perpendicular to the orbital plane, *i.e.*, along the z-axis of our grid. We also investigated off-axis jets with angles of 30°, 60°, 75° relative to the orbital axis of the system, inclined towards the binary companion (inclination angles perpendicular to the orbital separation vector would not result in any change in the simulation, given that simulations only cover a small fraction of the binary period once the jet is switched on). The detailed

model parameters of our different runs are described in table 4.1.

Note also that in cases where the jet is oriented perpendicular to the binary separation vector $\vec{a}$, the simulations have mirror-symmetry about $\vec{a}$; in these cases, in order to reduce the need for computational resources, we only simulate the upper hemisphere at full resolution, but include both hemispheres to avoid spurious boundary effects near the orbital plane. Results in those cases are quoted for the high-resolution half of the simulation.

4.2.3 Orbital Motion

The binary parameters were set loosely approximate the parameters for of Cygnus X-1. For simplicity, we set the mass of the black hole and the star to be 10 and 20 $M_\odot$, respectively, and the separation between them is set to be 3×10^{12} cm, which gives an orbital period of 5.8 days for Cygnus X-1, compared to the observed value of 5.6 days (Brocksopp et al. 1999; Pooley et al. 1999)

As we show below, the jet propagation time across one binary separation (1.7 minutes) and the time required for a quasi-stationary bent jet solution to be established (approximately 10 hours) is much shorter than the orbital time. For numerical simplicity and to allow direct comparison with the analytic formulae presented in §4.4.2, we neglected orbital rotation in most of our simulations, keeping the two nozzles stationary in our cartesian grid. As a first order approximation, this is justified because the orbital velocity is only of order 20% of the wind velocity, and thus orbital effects on the wind ram pressure introduce corrections of the order of only 5%.

In order to verify that the effects of orbital motion on the gross dynamics of jet propagation are small, we ran a sub-set of the simulations including orbital rotation, presented in §4.4.2. In this case, the nozzles (star and jet) move along their orbital

trajectories in the x-y plane (*i.e.*, we simulated the orbit in a fixed, non-rotating frame, which eliminates the need to introduce terms for Coriolis and centrifugal forces into the solver). The coordinate origin was set to be at the center of mass.

In the rotating case, we assumed that the star is co-rotating with the orbit, such that the outflow velocity at the stellar surface is given by

$$\vec{v}_{\rm wind,rot}(\vec{x}) = \vec{\omega} \times \vec{x} + \vec{v}_{\rm wind,*}\left(\vec{x} - \vec{R_*}\right), \tag{4.2}$$

where $\vec{\omega}$ is the orbital angular velocity, $\vec{v}_{\rm wind,*}$ the wind velocity at the stellar surface calculated from eq. (4.1), and $\vec{R_*}$ the position of the star.

We ran the simulations for one orbital period before switching on the jet in order to allow the flow to establish a converged velocity and density profile. After the jet launches, the simulations were carried out for several hours in real time units, long enough to establish the bow shock and the jet in a quasi-steady state (see §4.2.4).

Finally, we performed a comparison simulation of a jet propagating into a uniform wind with parameters matching those of our fiducial run at the position of the compact object (referred to below as UniWind_E36).

4.2.4 Measurement of the Jet Thickness and Propagation Direction

A key variable determining the strength of the jet-wind interaction is the thickness h of the jet as seen by the wind (*i.e.*, the size of the jet perpendicular to both jet and wind velocities). We measured h as follows.

In post-processing, we identified matter inside a computational cell as jet material if the value of $\zeta \equiv (v_z/v_{\rm jet})\, J$ exceeded a fixed threshold, where $(v_z/v_{\rm jet})$ is the flow velocity normalized by the initial jet speed, which is $3 \times 10^9\,{\rm cm\,s^{-1}}$ in our standard parametrization, and J is the fractional density of jet tracer fluid injected at the

nozzle. We found that a choice of $\zeta = 0.1$ successfully identified the jet material in all cases (see Figure 4.7). The thickness of the jet was measured in the direction perpendicular to the separation vector and the jet axis, since it is the dimension of the jet in that direction that determines the amount of wind momentum flux intercepted by the jet.

When the jet first turns on, it propagates in its initial direction, following the standard evolution of jet propagation until the expansion of the cocoon becomes slower than the wind velocity. As the head of the jet propagates, the accumulated perpendicular momentum flux begins to bend it away from its initial propagation direction. We then traced the propagation direction of the jet fluid to determine the jet trajectory and bending angle.

Table 4.1. : Parameter of the Simulations

Model	$L_{\rm jet}$ ($\rm ergs\,s^{-1}$)	$\mathcal{M}_{\rm jet,0}$	inclination (degree)	h_1 [b] ($\rm cm\,s^{-1}$)
SphWind_E35	10^{35}	30	0[a]	3×10^{10}
SphWind_E36	10^{36}	30	0	8×10^{10}
SphWind_E36_M10	10^{36}	10	0	1×10^{11}
SphWind_E36_rot	10^{36}	30	0	8×10^{10}
SphWind_E36_acc	10^{36}	30	0	8×10^{10}
SphWind_E36_30deg	10^{36}	30	30	8×10^{10}
SphWind_E36_60deg	10^{36}	30	60	8×10^{10}
SphWind_E36_75deg	10^{36}	30	75	8×10^{10}
SphWind_E37	10^{37}	30	0	1.5×10^{11}
SphWind_E37_gam166	10^{37}	30	0	1.5×10^{11}
UniWind_E36	10^{36}	30	0	8×10^{10}

[a] 0° indicates that the direction of the jet is perpendicular to the line between the star and the Black hole.

[b] The jet thickness at the re-collimation shock, h_1, is measured naively by checking the variation of the jet thickness along the jet from simulation results.

4.3 Results

4.3.1 Jet Bending in Spherical Winds

Our simulations confirm the general expectation that a powerful wind from a companion star can affect the propagation of the jet, and that the ultimate trajectory of the jet depends on the relative momentum flux in the wind and the jet, as well as the geometry of the system.

We briefly describe the morphology of the jet-wind interaction and compare it to simulations of jet bending observed in the interaction of a jet with a uniform medium (Yoon et al. 2011). Figure 4.1 shows snapshots of our fiducial run at a jet power of $L_{\rm jet} = 10^{36}\,{\rm ergs\,s^{-1}}$.

Upon injection into the grid, the jet fluid is generally over-pressured compared to the external pressure and the ram pressure of the stellar wind (the pressure is fixed by our choice of the jet power, the jet velocity, the Mach number, and the cross sectional area of the jet nozzle).

We chose this setup to allow the jet to establish a self-consistent, stable structure by letting the jet reach pressure equilibrium with the bow shock. During this phase, the jet does not experience any bending, given that it is strongly over-pressured with respect to the ram pressure in the stellar wind. We show a typical setup in Figure 4.1, which displays a density slice through the simulation. Generally, the lack of external confinement leads to free lateral expansion of the jet with a half-opening angle of order $\alpha_0 \sim 1/\mathcal{M}_{\rm jet,0}$. The wind is gravitationally focused by the black hole in the down stream region, generating the density enhancement along the equatorial plane visible to the left of the black hole in Figure 4.1. Here and in

the following, we place the x-axis along the orbital separation vector at t=0 and the z-axis along the orbital angular momentum vector.

The free expansion of the jet proceeds until its pressure reaches the pressure behind the bow shock of the wind, at which point the jet goes through a re-collimation shock and reaches a stable equilibrium thickness h_1. Thus, h_1 is not directly set as a simulation parameter, but instead determined by the initial Mach number of the jet.

However, since neither the re-collimation region nor the initial Mach number of the jet are observable, we will carry out most of the analysis in this paper using the jet thickness h beyond the re-collimation shock, relating it where possible to observables like the large scale opening angle of the jet $\alpha_{\rm obs}$. We will describe the details of the re-collimation region, which is very close to the black hole compared to the size of the simulation box, in §4.3.2.

The approaching stellar wind material goes through a stationary bow shock as it is forced to propagate around the jet. Beyond the re-collimation shock, the transverse pressure gradient imparted on the jet by the lateral momentum flux of the stellar wind then gradually bends the jet fluid away from the companion star, while the jet thickness h is set by lateral pressure balance with the wind bow shock pressure.

The effects of the radially declining wind density and the changing velocity of the wind as a function of distance along the jet imprint a qualitatively different asymptotic behavior of the jet compared to interaction with a uniform medium. Because the density declines roughly as r^{-2}, where r is the distance from the center of the star, the effect of bending declines with distance, and most of the bending

occurs within about a binary orbital separation from the jet nozzle.

More importantly, jet bending is caused only by transverse momentum flux, which depends on the angle $\vartheta = \sin^{-1}\left(\left|\hat{\vec{v}}_{\rm jet} \times \hat{\vec{v}}_{\rm wind}\right|\right)$ between the local jet velocity and wind velocity through $\sin^2(\vartheta)$. Because ϑ decreases with increasing r, the amount of transverse momentum flux also decreases with r. Asymptotically, any initially large ϑ will tend to zero (even in the absence of any jet bending) and the amount of lateral momentum flux across the jet decreases strongly with distance. At infinity, jet and wind travel parallel to each other at some asymptotic angle ψ_∞ relative to the initial jet direction. In contrast, in a uniform wind, ϑ does not decrease with distance from the nozzle, and both jets must eventually be bent such that the jet plasma asymptotically flows parallel to the wind direction.

We ran simulations with jet powers of $L_{\rm jet} = 10^{35}$, 10^{36}, $10^{37}\,{\rm ergs\,s^{-1}}$, and the results are shown in Figure 4.2. The dashed lines indicate the converged asymptotic lines towards which the jet is bent by the wind, showing that the ψ_∞ is a strong function of jet power. In the case of $L_{\rm jet} = 10^{35}\,{\rm ergs\,s^{-1}}$, the ram pressure by the stellar wind is sufficiently strong to bend the jet by almost 90°, similar to the case of the UniWind_E36 uniform wind model. On the other hand, for the highest jet power case in our simulation, $L_{\rm jet} = 10^{37}\,{\rm ergs\,s^{-1}}$, the bending angle is small. We will discuss the relationship between the jet kinetic power and the inclination angle in §4.4.2.

We generally find that the jet is bent towards its asymptotic bending angle within a time scale of $\tau_{\rm bend} \sim 0.05\,\tau_{\rm orbit}$, where $\tau_{\rm orbit}$ is the orbital period; this is roughly the time for the geometry of the inner jet to reach a steady state. We measured the propagation direction and asymptotic bending angle of the jet after it

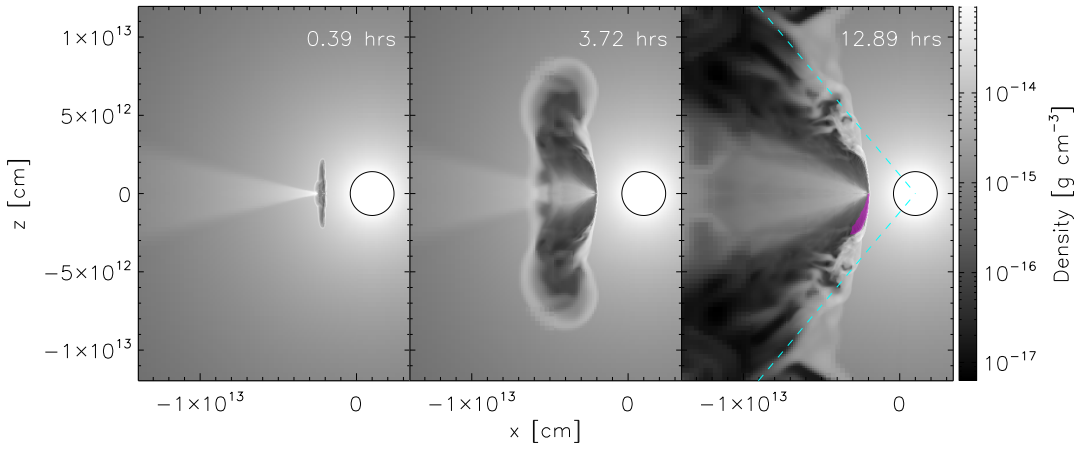

Fig. 4.1. — : Time sequence of density maps for our fiducial simulation Sph-Wind_E36. The black circle indicates the surface of the companion star. The enhanced density in the down stream of equatorial plane to the left of the black hole is due to the gravitationally focused wind. The bow shock structure along the jet reaches steady state approximately in 12 hours after it launches. The magenta area in the right-most image indicates the jet materials (marked only in the lower half of the image), identified by a certain threshold (see §4.4.1). The cyan dashed lines in the right-most panel indicate asymptotic lines along which the jets converge, showing that the jet is bent by approximately 30° from the initial direction. In the down-stream region, the bow-shocked wind passes around the jet and re-collimates in an expansion fan and a (weak) re-collimation shock, as expected for super-sonic flow around an object, leaving the post-shock region filled with wind gas, visible in the right-most two panels.

settled into its steady state. Note that the short bending time scale $\tau_{\rm bend} << \tau_{\rm orbit}$ implies that the jet reacts instantaneously to changes in binary orbit, which further implies that the jets must be precessing on the orbital period of the system if bent by jet-wind interaction.

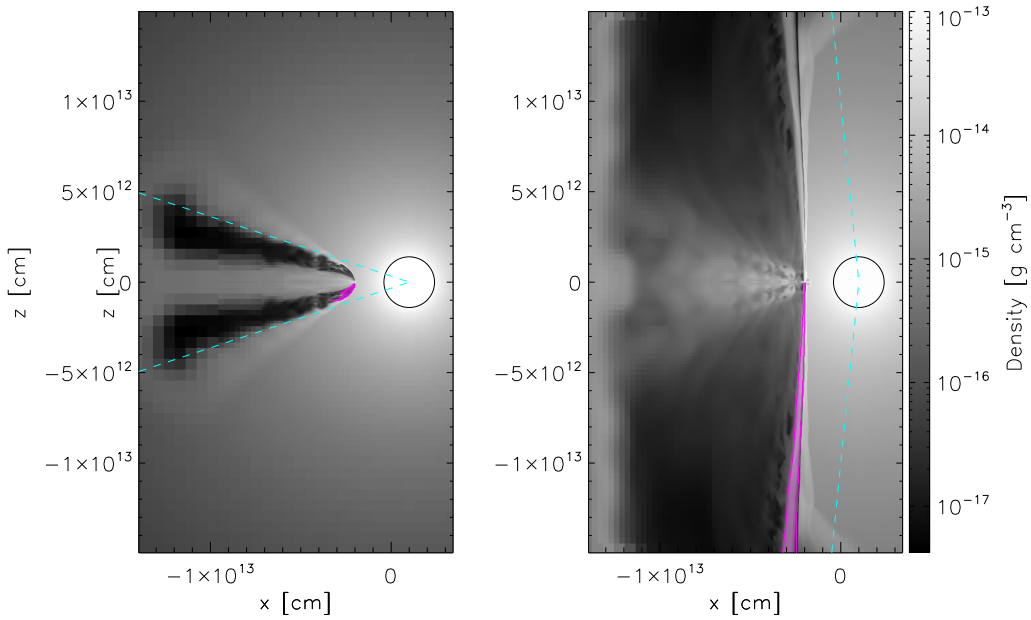

Fig. 4.2. — : Density maps for the case of SphWind_E35 (left panel) and SphWind_E37 (right panel) after the steady state bow shock structure has been established. While the jet for SphWind_E35 is disrupted within a short distance from its injection, the jet for SphWind_37 is steadily maintained (marked in magenta color). The cyan dashed lines indicate that the jet bending angles are 65° and 8° for SphWind_E35 and SphWind_E37, respectively. The vertical black thin trajectory in right panel is the low density area generated by the shear layer between the jet and the bow shock.

Figure 4.3 explores the dependence of our simulations on the initial internal Mach number of the jets, with $\mathcal{M}_{\rm jet,0}$ set to one third of our fiducial value. With

otherwise identical parameters, a smaller Mach number implies larger thermal energy relative to the total energy of jet. The increased thermal pressure leads to a larger initial opening angle of the jet, which in turn results in an increase in transverse momentum transfer and jet bending. The increased surface area and decreased Mach number also increase the incidence of Kelvin-Helmholtz instability and earlier onset of jet disruption.

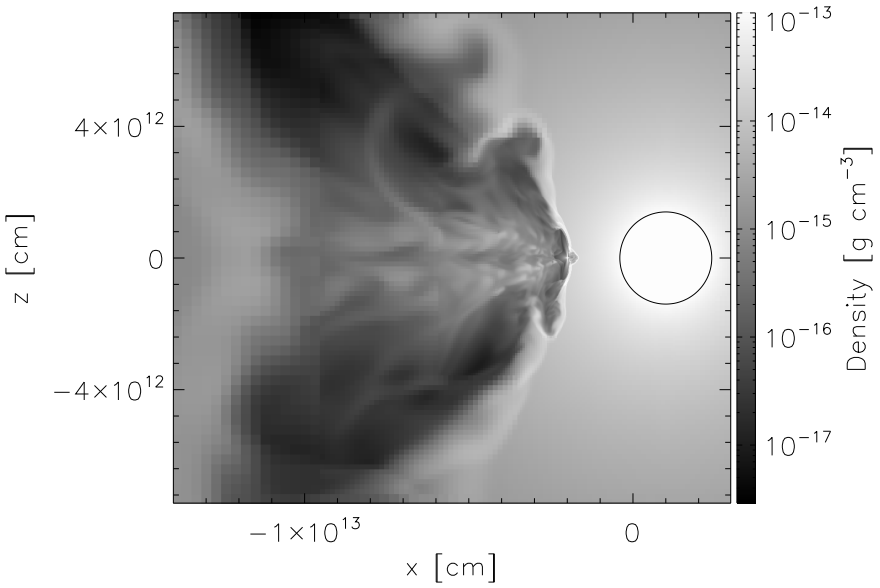

Fig. 4.3. — : Density map in the case of lower Mach number, $\mathcal{M}_{\rm jet,0} = 10$ (SphWind_E36_M10).

4.3.2 The Re-collimation Shock

In order to investigate the physics of jet re-collimation by the wind, we carried out a set of test simulations with significantly increased resolution, restricted to a shorter duration. We performed the tests with two jet Mach numbers, $\mathcal{M}_{\rm jet,0} = 10, 30$. Snapshots of the re-collimation region are shown in Figure 4.4. We measured the jet thickness along the y-axis (y-z slice) for the analysis below because the effective

cross section of the wind momentum flux captured by the jet depends only on the width of the jet in y-direction. Jet bending is facilitated by the pressure gradient in the x-z plane, where only the leading edge of the jet is subject to the increased pressure behind the bow shock.

In our simulations, the jet is initially freely expanding. Acceleration of the lateral expansion will become inefficient once the lateral motion itself becomes supersonic. This sets the characteristic semi-opening angle α_0 of such a supersonic "fan" simply as

$$\alpha_0 \sim \frac{1}{\mathcal{M}_{\mathrm{jet},0}} = \frac{c_{\mathrm{s},0}}{v_{\mathrm{jet}}} = \sqrt{\frac{\gamma P_0}{\rho_0}} \frac{1}{v_{\mathrm{jet}}}. \tag{4.3}$$

In Figure 4.5 we plot the measured jet thickness h as a function of height z. As expected, the jet with the initially higher Mach number has a narrower opening angle.

From the numerical experiment, the initial half-opening angle α_0 of the jet is roughly

$$\alpha_0 \sim \frac{3}{\mathcal{M}_{\mathrm{jet},0}} \tag{4.4}$$

slightly larger than the simplistic estimate $\alpha_0 \sim 1/\mathcal{M}_{\mathrm{jet},0}$.

Once the conical expansion has been established, the lateral ram pressure $P_{\mathrm{jet,ram},\perp}$ of the jet

$$P_{\mathrm{jet,ram},\perp} = \rho_{\mathrm{jet}} \sin^2 \alpha_0 \, v_{\mathrm{jet}}^2 = \rho_0 \left(\frac{z_0}{z}\right)^2 \sin^2 \alpha_0 \, v_{\mathrm{jet}}^2 \tag{4.5}$$

is always larger than the internal pressure (since the lateral expansion is supersonic).

In terms of the kinetic jet power

$$L_{\mathrm{jet,kin}} = \pi \rho_{\mathrm{jet}} v_{\mathrm{jet}}^3 h^2/4 = \pi \rho_{\mathrm{jet}} v_{\mathrm{jet}}^3 z^2 \sin^2 \alpha_0 \tag{4.6}$$

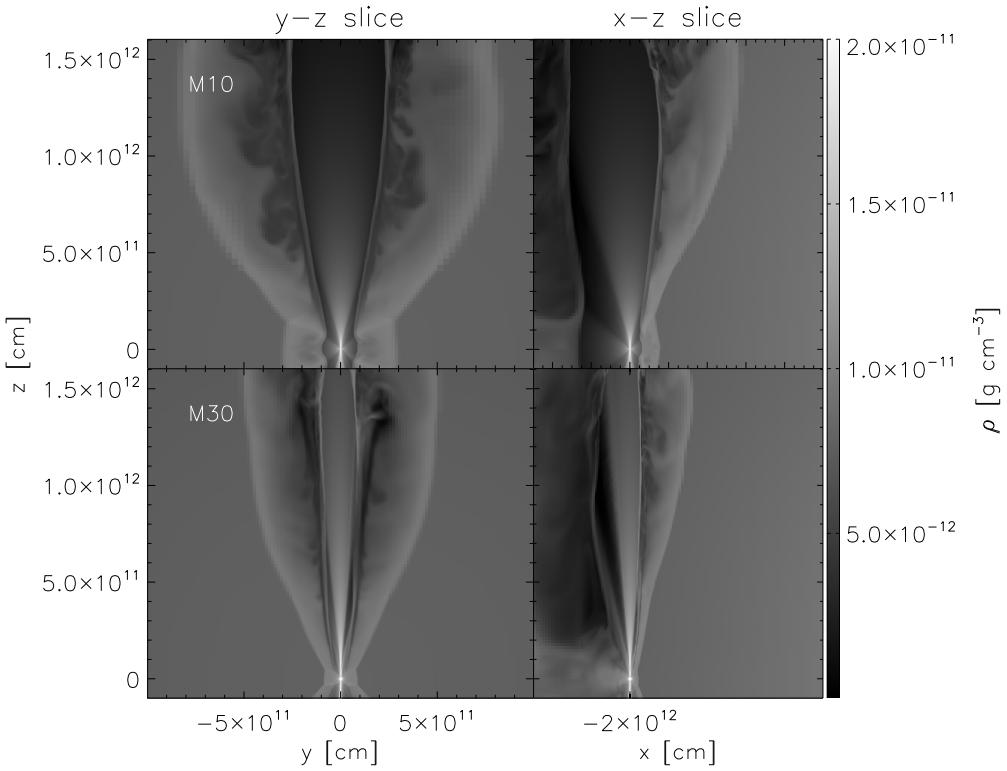

Fig. 4.4. — : Density map for re-collimating jets in $\mathcal{M}_{\rm jet,0} = 10$ (upper panels), and $\mathcal{M}_{\rm jet,0} = 30$ (lower panels). The jet is re-collimated in the y-z plane while bending occurs in the x-z plane.

the lateral ram pressure is

$$P_{\rm jet,ram,\perp} = \frac{L_{\rm jet,kin}}{\pi z^2 v_{\rm jet}} \tag{4.7}$$

independent of $\sin\alpha_0$ and $\mathcal{M}_{\rm jet,0}$.

Lateral expansion will proceed until $P_{\rm jet,ram,\perp}$ drops below the pressure in the wind bow shock that forms around the jet, $P_{\rm wind,ram}$. At this point, a re-collimation shock must form in the jet and bring the internal pressure of the jet into equilibrium with the bow shock. We will denote the location of the re-collimation shock along the jet as z_1. For parameters considered in this paper, z_1 is always much smaller than

the binary separation a, so we will assume that ram pressure of the wind is constant for the discussion of z_1 and h_1, so the wind ram pressure is given by its value in the equatorial plane at the location of the black hole.

In terms of the mass loss rate of the wind[1], $\dot{\mathrm{M}}_{\mathrm{wind}} = 4\pi r^2 v_{\mathrm{wind}} \rho_{\mathrm{wind}} = 4\pi a^2 v_{\mathrm{wind}} \rho_{\mathrm{wind},0}$, the wind ram pressure at the jet nozzle is then

$$P_{\mathrm{wind,ram},0} = \rho_{\mathrm{wind},0} v_{\mathrm{wind}}^2 = \frac{\dot{\mathrm{M}}_{\mathrm{wind}} v_{\mathrm{wind}}}{4\pi a^2} \tag{4.8}$$

where, $\rho_{\mathrm{wind},0}$ is the wind density at the footpoint of the jet and v_{wind} is the velocity of the stellar wind, assumed to be constant.

The location of the re-collimation shock z_1 is given by equating $P_{\mathrm{jet,ram},\perp} = P_{\mathrm{wind,ram},0}$:

$$z_1 = a\sqrt{\frac{4L_{\mathrm{jet}}}{\dot{\mathrm{M}}_{\mathrm{wind}} v_{\mathrm{wind}} v_{\mathrm{jet}}}} \tag{4.9}$$

again independent of $\mathcal{M}_{\mathrm{jet},0}$ and α_0.

This simple picture is confirmed by the high-resolution simulations of the re-collimation shock: Figure 4.5 shows the re-collimation shock at $z \approx 7 \times 10^{11}$cm regardless of the jet Mach number, consistent with the analytic solution from eq. (4.9) for the assumed parameters.

At the re-collimation shock, the jet will have a thickness h_1 and will be in pressure equilibrium. Beyond z_1, the jet will thus adjust its thickness h to maintain pressure equilibrium with the wind. We will discuss the propagation of the jet in this phase, and the interaction with the wind that occurs beyond z_1, in the next section.

---

[1]Given typical properties of OB-type stars, the mass loss rate is of order $\dot{\mathrm{M}}_{\mathrm{OB}} \sim 10^{-7} \sim 10^{-5}\,\mathrm{M}_\odot\,\mathrm{yr}^{-1}$ with a terminal velocity of $v_{\mathrm{wind}} \approx 2000 - 3000\,\mathrm{km\,s}^{-1}$ (Castor et al. 1975; Puls et al. 2008).

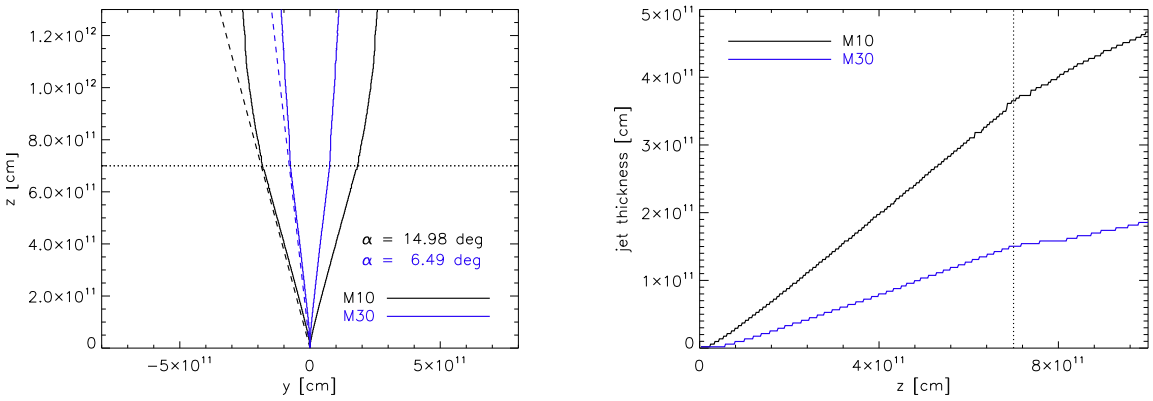

Fig. 4.5. — : Left panel: Identified jets from simulation for the case of $\mathcal{M}_{\rm jet,0} = 10, 30$. Right panel: Measured jet thickness along jet. The dotted lines indicate the location of re-collimation shock.

4.4 Discussion

As described above, the development of an asymptotic bending angle ψ_∞ is expected from simple considerations of the geometry of the interaction between jet and wind.

A full analytic description of the detailed dynamical evolution of the jet (including the onset of dynamical instabilities such as Kelvin-Helmholtz instability) is beyond the scope of this paper. Therefore, for the following analysis, we make the assumption that the bending angle ψ of the jet is small (implying relatively weak interaction).

Because non-linear effects (like dynamical instabilities) tend to increase the cross section of the jet, they will tend to increase the bending angle due to the large net transverse momentum intercepted by the jet. In that sense, the relations derived below will be lower limits on the actual bending angle. This is borne out by our simulations (See Figure 4.9 below).

We will further assume that the wind is asymptotic, *i.e.*, has reached constant velocity before interacting with the jet and thus follows a simple r^{-2} density profile. We will also neglect effects of orbital motion in the analytic approximations below (justified by the fact that they can be expected to be about an order of magnitude smaller than the dominant effects, as argued above).

4.4.1 The Evolution of the Jet Thickness Beyond the Re-Collimation Shock

We will assume that the jet is in pressure equilibrium with the ram pressure of the wind,

$$P_{\rm jet,ram,\perp} = \rho_{\rm wind}(\theta)\left(v_{\rm wind}\cos^2\theta\right)^2 = \rho_{\rm wind,0} v_{\rm wind}^2 \cos^4\theta = \rho_{\rm wind,0} v_{\rm wind}^2 \left(\frac{a^2}{a^2+z^2}\right)^2 \tag{4.10}$$

where we have used $\cos\theta = a/\sqrt{a^2+z^2}$, where θ is the angle between the orbital separation vector $\vec{a}$ connecting the star and the black hole, and the vector $\vec{r}$ from the star to a given position along the jet. The jet has an initial jet thickness h_1, as discussed above, which we take as a parameter in the following.

The geometry of the jet and the re-collimation shock and the definitions of the relevant angles and coordinate axes are sketched in Figure 4.6.

Beyond the re-collimation shock, the jet thickness h follows from pressure equilibrium between the jet and the bow shock:

$$P_{\rm jet,ram,\perp} = \rho_{\rm wind,0} v_{\rm wind}^2 \left(\frac{a^2}{a^2+z^2}\right)^2 = P_{\rm jet} = P_{\rm eq,1}\left[\frac{h(z)}{h_1}\right]^{-2\gamma} \tag{4.11}$$

where $P_{eq,1}$ and h_1 are the pressure and the jet thickness at the re-collimation shock. This sets the jet thickness h:

$$h\,(z) = h_1\left(\frac{a^2}{a^2+z^2}\right)^{-1/\gamma} \tag{4.12}$$

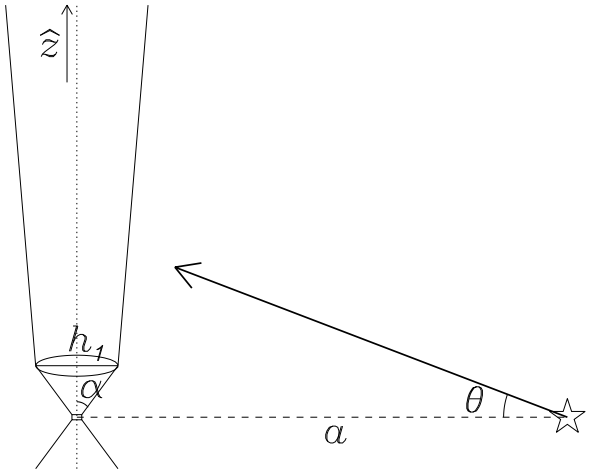

Fig. 4.6. — : Schematic figure. α is a jet semi-opening angle, a is a separation, θ is an inclination angle from the orbital plane, and h_1 is the jet thickness at the collimation shock.

Figure 4.7 shows the measured jet thickness h as a function of z for simulation SphWind_E37, compared to the value calculated from eq. (4.12), for different choices of the jet threshold (see §4.2.4). The figures show good agreement between the model and the simulation.

Generally, h_1 will not be measurable. However, we can us eq. (4.12) to relate a measured jet thickness (or an upper limit) at large z to the jet thickness at any other z, given values for γ and a.

Stirling et al. (2001) reported that the VLBA jet of Cygnus X-1 has a semi-opening angle of $\alpha_{\rm VLBA} = h/2\,z_{\rm VLBA} \lesssim 2^\circ$, where $z_{\rm VLBA}$ is the scale length of the extended jet on which the opening angle is measured; the orbital separation and the length of the jet are 0.1 mas and 15 mas, respectively. By using eq. (4.12) with $\gamma = 4/3$, the jet thickness at the re-collimation shock can be estimated as $h_1 \lesssim 5.7 \times 10^{-3}\,a$. For a value of $\gamma = 5/3$, we find a value of $h_1 \lesssim 1.3 \times 10^{-2}\,a$. We

will further discuss the constraints on the initial half-opening angle in the case of the Cygnus X-1 jet in §4.4.4.

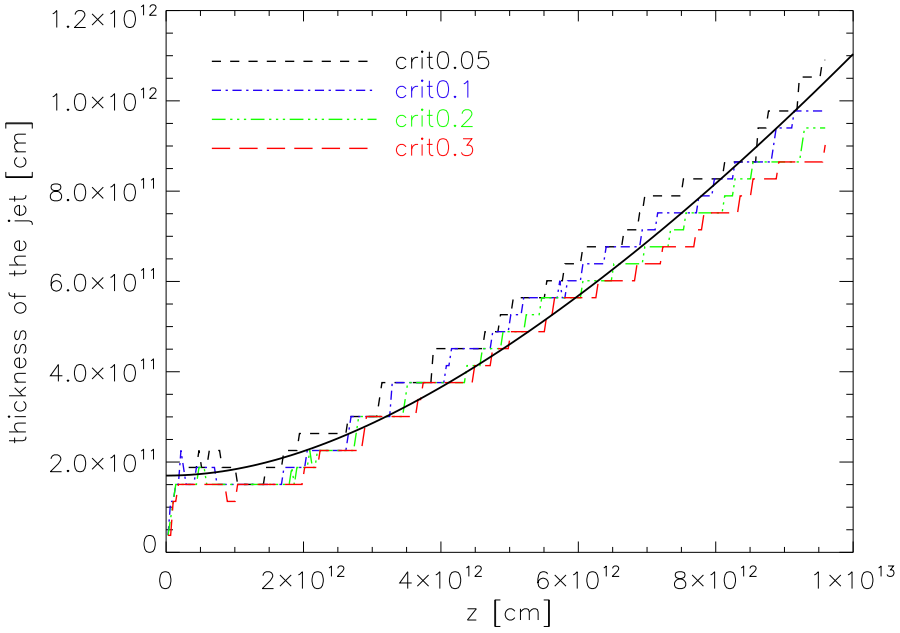

Fig. 4.7. — : The thickness of the jet in SphWind_E37 model. The solid black line represents the analytic solution from eq. (4.12) with the parameters appropriate for the model of SphWind_E37, and dashed and dot-dashed lines indicate the numerical results for different choices of the threshold used to determine whether a computational cell belongs to the jet.

4.4.2 Jet Bending and the Asymptotic Bending Angle

With an expression for the jet thickness h from eq. (4.12), we can now discuss the amount of bending experienced by the jet. Technically, jet bending occurs because a transverse pressure gradient exists behind the bow shock that the wind drives around the jet, such that the external pressure at the leading edge is $P_1 \sim P_{\rm bow}$ and

the pressure on the trailing edge of the jet is $P_2 \ll P_1$. Thus, a transverse pressure gradient exists inside the jet as well, acting to accelerate/bend the jet fluid away from the star.

In deriving an estimate for ψ_∞, we will make the simplifying assumption that the bending angle is small, *i.e.*, that the accumulated transverse momentum flux is small compared to the lateral momentum flux. The reason for this assumption is that the jet will be dynamically disrupted if the bending angle is large, as the jet-boundary interaction must be significant in this case. Our simulations bear out the validity of this assumption at least in the hydrodynamic case studied here. Similarly, we neglect the momentum transfer from the wind to the jet in the longitudinal direction, which would lead to acceleration or deceleration by a small amount.

Based on the properties of observed astrophysical jets (the presence of shocks, the inferred large kinetic power compared to the minimum internal energy based on the observed synchrotron intensity), we further assume the jet to be supersonic (large internal Mach number) and ballistic (no further acceleration beyond the nozzle). This reflects the setup of our simulations.

Under the assumption of constant longitudinal jet velocity and $\mathcal{M}^2_{\rm jet,0} \gg 1$, the longitudinal jet momentum per unit jet length is conserved and given by

$$\Phi_{m,\rm jet} = \int dA_\perp \rho_{\rm jet} v_{\rm jet} = \pi\, r^2_{\rm jet,0}\, \rho_{\rm jet,0}\, v_{\rm jet} = \frac{L_{\rm jet,kin}}{v^2_{\rm jet}}, \tag{4.13}$$

where $dA_\perp$ is the area element perpendicular to the initial jet direction, $r_{\rm jet,0}$ and $\rho_{\rm jet,0}$ are the radius and the density of the jet at the nozzle.

The transverse momentum per unit jet length accumulated by the jet can be

derived as a function of z:

$$\begin{aligned}
\Delta\Phi_{m,\mathrm{wind}} &= \int_0^{t(z)} dt \int_{-h/2}^{h/2} dy \int_{-X(y)/2}^{X(y)/2} dx \nabla_x P_{\mathrm{bow}} \\
&= \int_0^z \frac{dz'}{v_{\mathrm{jet}}} \int_{-h/2}^{h/2} dy P_{\mathrm{bow}} \\
&= \int_0^z \frac{dz'}{v_{\mathrm{jet}}} h(z') P_{\mathrm{bow}} \\
&= \int_0^z \frac{dz'}{v_{\mathrm{jet}}} \rho_{\mathrm{wind},0} v_{\mathrm{wind}}^2 \left(\frac{a^2}{a^2+z'^2}\right)^2 h_1 \left(\frac{a^2}{a^2+z'^2}\right)^{-1/\gamma} \\
&= \frac{h_1 \rho_{\mathrm{wind},0} v_{\mathrm{wind}}^2}{v_{\mathrm{jet}}} a f(z,\gamma) \\
&= \frac{h_1 \dot{\mathrm{M}}_{\mathrm{wind}} v_{\mathrm{wind}}}{4\pi\, a\, v_{\mathrm{jet}}} f(z,\gamma) \qquad (4.14)
\end{aligned}$$

where

$$f(z,\gamma) \equiv \int_0^{z/a} dy \left(\frac{1}{1+y^2}\right)^{2-1/\gamma} \qquad (4.15)$$

which can be expressed as a combination of hypergeometric functions, but is most easily evaluated numerically.

In the first order (small bending angle) approximation we are making here, the ratio of transverse to longitudinal momentum is equal to the bending angle (*i.e.*, the angle between the local and the initial velocity vector or tangent vector of the jet as a function of z):

$$\begin{aligned}
\psi(z,\gamma) &= \frac{v_\perp}{v_\parallel} = \frac{\Delta\Phi_{m,\mathrm{wind}}}{\Phi_{m,\mathrm{jet}}} \\
&= \frac{\dot{\mathrm{M}}_{\mathrm{wind}} v_{\mathrm{wind}} v_{\mathrm{jet}}\, h_1}{4\pi\, a\, L_{\mathrm{jet,kin}}} f(z,\gamma) \qquad (4.16)
\end{aligned}$$

The asymptotic value for $z \longrightarrow \infty$ can then be evaluated in terms of elementary

Gamma functions by taking the appropriate limit of $f(z,\gamma)$:

$$\begin{aligned}\psi_\infty &= \lim_{z\to\infty}\psi(z,\gamma) = \frac{\dot{\mathrm{M}}_{\rm wind} v_{\rm wind} v_{\rm jet}\, h_1}{4\pi\, a\, L_{\rm jet,kin}} \lim_{z\to\infty} f(z,\gamma) \\ &= \frac{\dot{\mathrm{M}}_{\rm wind} v_{\rm wind} v_{\rm jet}\, h_1}{4\pi\, a\, L_{\rm jet,kin}} \frac{\sqrt{\pi}}{2} \frac{\Gamma(3/2-1/\gamma)}{\Gamma(2-1/\gamma)} \end{aligned} \tag{4.17}$$

where

$$f(\gamma) \equiv \lim_{z\to\infty} f(z,\gamma) = \frac{\sqrt{\pi}}{2} \frac{\Gamma(3/2-1/\gamma)}{\Gamma(2-1/\gamma)} \tag{4.18}$$

with $f(4/3) = 1.2$ and $f(5/3) = 1.07$ for a relativistic and non-relativistic monatomic gas, respectively. Hence, for otherwise identical parameters, the jet should be bent about 10% less in the case of $\gamma = 5/3$ compared to the case of $\gamma = 4/3$, showing that the effect of adiabatic index on ψ_∞ is moderate. Figure 4.8 shows the dependence of the $f(\gamma)$ on the adiabatic index from $\gamma = 4/3$ to $\gamma = 5/3$.

While h_1 cannot be measured observationally, we can express eq. (4.17) in terms of the observable jet width on VLBA scales, $h_{\rm obs}$ measured at distance $z_{\rm obs} \gg a$, or alternatively, the observed opening angle $\alpha_{\rm obs} = h_{\rm obs}/(2z_{\rm obs})$:

$$\begin{aligned}\psi_\infty &= \frac{h_{\rm obs}}{a}\left(\frac{a^2}{a^2+z_{\rm obs}^2}\right)^{1/\gamma} \frac{\dot{\mathrm{M}}_{\rm wind} v_{\rm wind} v_{\rm jet}}{4\pi L_{\rm jet,kin}} f(\gamma) \\ &\approx \alpha_{\rm obs}\left(\frac{z_{\rm obs}}{a}\right)^{1-2/\gamma} \frac{\dot{\mathrm{M}}_{\rm wind} v_{\rm wind} v_{\rm jet}}{2\pi L_{\rm jet,kin}} f(\gamma) \end{aligned} \tag{4.19}$$

where $z_{\rm obs} = z_{\rm VLBA}/\sin(\theta_{\rm LOS})$ and $\alpha_{\rm obs}$ are assumed to be corrected for foreshortening given the line-of-sight inclination angle $\theta_{\rm LOS}$ of the jet.

We carried out one test simulation, SphWind_E37_gam166, with $\gamma = 5/3$ for the jet fluid, and the resulting jet appears more straight, consistent with analytic expression (see Figure 4.9). Note that the ratio is independent of the orbital separation, a, because of the relationship $h_1 = 2z_1 \sin\alpha_0$, where z_1 can be calculated from eq. (4.9).

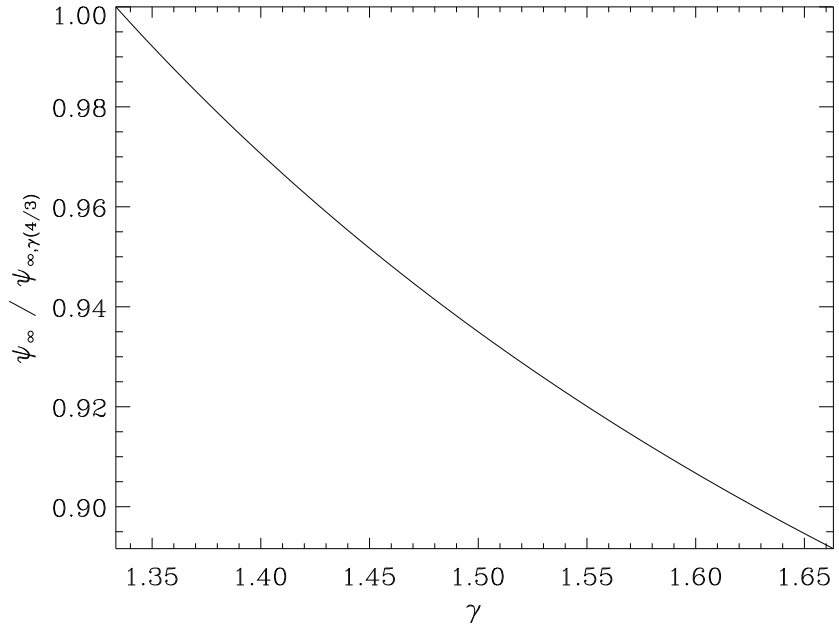

Fig. 4.8. — : The asymptotic jet bending angle as a function of adiabatic index, γ. The angle is normalized by the one for the case of $\gamma = 4/3$.

While these expressions are strictly non-relativistic, it is straight forward to show that in the ultra-relativistic case, the estimate for the bending angle ψ is increased by a factor of $\sqrt{2}$ over the non-relativistic case (where the velocity is simply set to $v = c$). Thus, the lower limits we derive below on $L_{\rm jet}$ from observational upper limit on ψ becomes *stronger* in the relativistic case.

In the small bending angle regime, our analytic expressions are consistent with the simulation results, as shown in Figure 4.9. In the figure, the solid curves were constructed by integrating the jet trajectory along z, given the analytic expression for the transverse velocity $v_{\rm jet,\perp} \approx \psi v_{\rm jet}$ from eq. (4.16) in the small angle approximation [*i.e.*, $d(x - x_0)/dz = \tan\psi$ where x_0 is the location of the black hole]. For small bending angles, the figure shows excellent agreement between the model and the

simulations.

As expected, for the case of stronger jet power, $L_{\rm jet} = 10^{37}\,{\rm ergs\,s^{-1}}$, the jet is only moderately bent from the initial direction, while lower power jets are more strongly affected by the winds, resulting in a higher degree of deflection. In the figure, the solid lines represent analytic trajectories calculated by eqs. (4.13)-(4.14) and dashed lines indicate the asymptotic direction estimated in eq. (4.17).

In the case of our fiducial simulation (jet power $L_{\rm jet} = 10^{36}\,{\rm ergs\,s^{-1}}$), the jet becomes dynamically unstable around $z = 2.5 \times 10^{12}\,{\rm cm}$, which leads to significant broadening of the jet and enhanced bending, and, as a result, the jet begins to deviate from the analytic estimate. Further quantitative analysis of the turbulent structures and their effect to the evolution of the jet is beyond this work. It is, however, clear from the simulations that jet-instability will only *increase* $\Delta\Phi_{m,{\rm wind}}/\Phi_{m,{\rm jet}}$ and ψ_∞.

Thus, our small jet bending angle approximation can be considered a robust lower limit of the actual jet bending angle. Figure 4.10 shows the fractional deviation of the numerical result from the analytic estimate as a function of jet bending angle. Our analytic formula is very accurate for bending angles smaller than 20°. For larger bending angles, the approximation breaks down.

4.4.3 The Effects of Orbital Motion and Wind Acceleration

We carried out two simulations including the effects of orbital motion(SphWind_E36_rot) and radiatively driven winds (SphWind_E36_acc) in order to evaluate the importance of both effects by comparing to our standard model.

Figure 4.9 shows that, for small bending angles, the effects are small and the results with and without orbital motion and wind acceleration are consistent with each other. This is not surprising, since the centrifugal force from the orbital motion

is about 3 orders of magnitude less than radiative force, and the Coriolis force acts purely in the transverse direction. Therefore, our setup with fixed black hole and star positions is sufficiently accurate in the context of this analysis.

We reach a similar conclusion about the effect of radiative acceleration. The model with a radiatively driven wind has a negligibly small difference in the momentum flux of the stellar wind at the binary separation compared to our standard model. It implies that our assumption that the wind reaches terminal velocity before encountering the jet is valid.

For large bending angles, where dynamical instabilities lead to rapid jet disruption and increased bending, the deviation between individual simulations is noticeable, as expected given the time variability of the jet trajectory on those scales.

4.4.4 Jet Bending as a Diagnostic of Jet Power: The case of Cygnus X-1

In the limit that $\Delta\Phi_{m,\mathrm{wind}} > \Phi_{m,\mathrm{jet}}$, bending in the simulation is so strong that the jet is dynamically disrupted, rather than simply bent. The interaction disperses the jet into a broad, no longer collimated flow at much lower velocity than the jet velocity. We would not expect such a strongly bent jet to survive as an observable radio jet. This suggests a simple diagnostic: If a stable compact jet is observed intact in an HMXB, one can conclude that the bending angle should be moderate.

For example, the compact VLBA jet of Cyg X-1 is extended, with a scale length z_{VLBA} of approximately 15 mas (compared to the angular scale of the orbital separation a of 0.1 mas), with an upper limit to the half-opening angle of $\alpha_{\mathrm{VLBA}} < 2^\circ$ where the viewing angle, θ_{LOS}, is approximated to 40° (Stirling et al. 2001). Combined with the other fiducial parameters of Cyg X-1, a robust limit can be derived from the observed stable compact jet by taking the bending angle to be

$\psi_\infty = \Delta\Phi_{m,\rm wind}/\Phi_{m,\rm jet} \ll \pi/2$, which gives

$$\frac{(L_{\rm jet}/10^{37}\,{\rm ergs\,s^{-1}})\,(\sin\theta_{\rm LOS}/\sin 40^\circ)^{-2/\gamma}\,[f(\gamma=4/3)/f(\gamma)]\,\left(\frac{z_{\rm VLBA}}{a}\right)^{\frac{3}{2}\left(\gamma-\frac{4}{3}\right)}}{\left(\dot{\rm M}_{\rm wind}/2.6\times10^{-6}\,{\rm M_\odot\,yr^{-1}}\right)\,(v_{\rm wind}/1.6\times10^{8}\,{\rm cm\,s^{-1}})\,(v_{\rm jet}/0.6\,c)\,(\alpha_{\rm VLBA}/2^\circ)} \gg 8.5\times10^{-3} \tag{4.20}$$

where $\gamma = 4/3$ in our standard model. For the case of $\gamma = 5/3$, the limit increases to 3.9×10^{-2} due to relatively shallow increase in jet thickness along the jet, which requires a larger initial opening angle α_0 and thus a wider initial jet to give the same observed $\alpha_{\rm VLBA} \lesssim 2^\circ$.

This limit can be made more specific by the fact that the jet appears to be oriented in the same direction in separate VLBA radio observations, taken during different orbital phases (Stirling et al. 2001). The data suggest a possible moderate bending on the jet of less then 10° on VLBA scales. Given the stability of the jet, we consider this an upper limit on the jet bending angle, *i.e.*, $\psi_\infty \lesssim 10^\circ$, which translates to

$$\begin{aligned} L_{\rm jet} \;\gtrsim\; & 7.6\times10^{35}\,{\rm ergs\,s^{-1}} \\ & \times\left(\frac{\dot{\rm M}_{\rm wind}}{2.6\times10^{-6}\,{\rm M_\odot\,yr^{-1}}}\right)\left(\frac{v_{\rm wind}}{1.6\times10^{8}\,{\rm cm\,s^{-1}}}\right)\left(\frac{v_{\rm jet}}{0.6\,c}\right)\left(\frac{\alpha_{\rm VLBA}}{2^\circ}\right)\left(\frac{\sin\theta_{\rm LOS}}{\sin 40^\circ}\right)^{2/\gamma} \\ & \left[\frac{f(\gamma)}{f(\gamma=4/3)}\right]\left(\frac{z_{\rm VLBA}}{a}\right)^{\frac{3}{2}\left(\gamma-\frac{4}{3}\right)}, \end{aligned} \tag{4.21}$$

where for $\gamma = 5/3$, this limit increases to $3.47 \times 10^{36}\,{\rm ergs\,s^{-1}}$.

This lower limit on the jet power is consistent with the range of jet powers quoted in Gallo et al. (2005), Russell et al. (2007), and Sell et al. (2015), but derived from a completely independent, likely more robust argument.

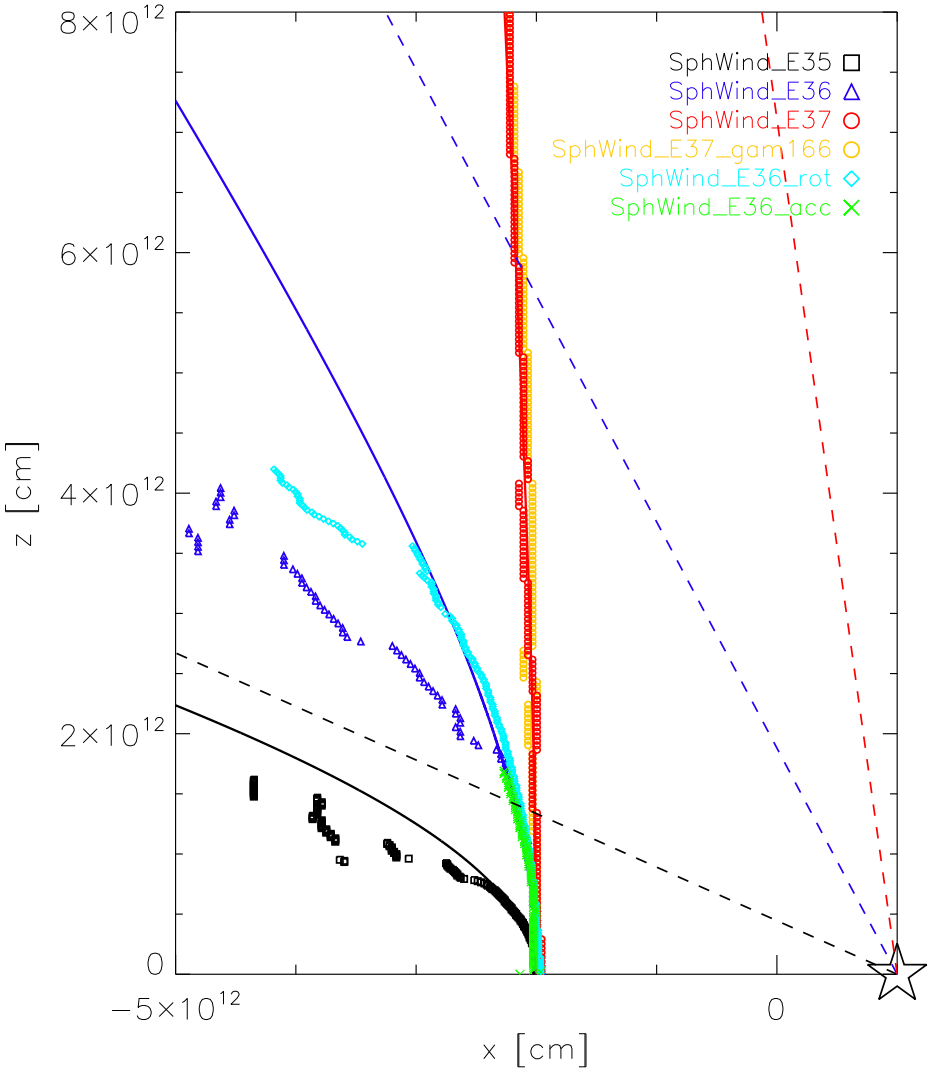

Fig. 4.9. — : Comparison of numerical results with analytic estimates. Each symbol represents the numerical result, and solid lines indicate the analytic jet trajectories. Dashed lines indicate the asymptotic towards which the jet is expected to converge analytically.

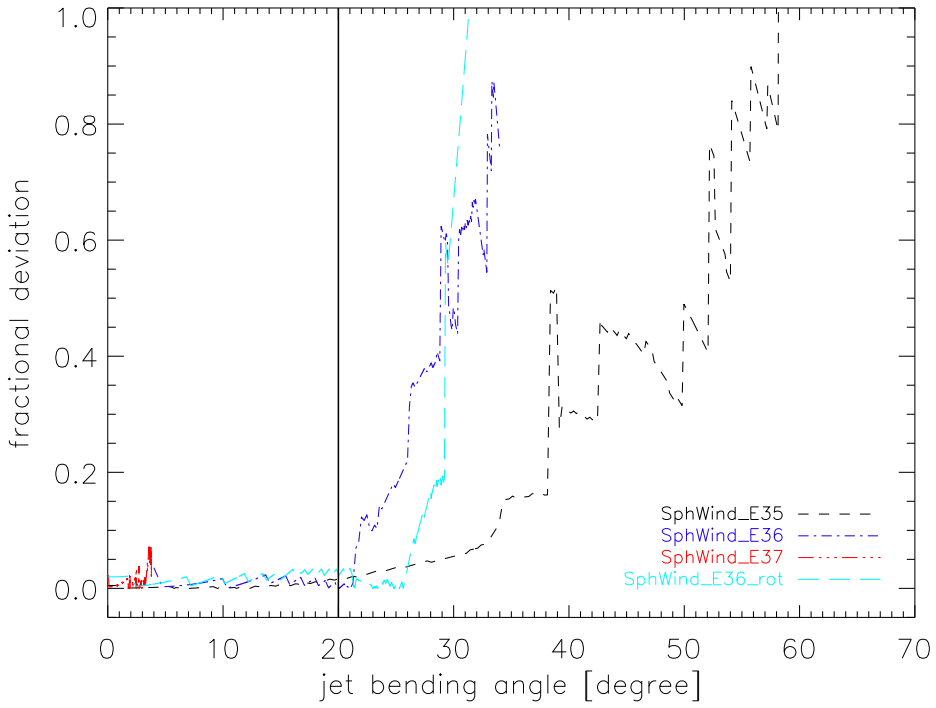

Fig. 4.10. — : Fractional deviation of the jet trajectory between numerical result and analytic formula as a function of jet bending angle.

4.4.5 Off-axis Jets

When the progenitor of the compact object in an X-ray binary undergoes a supernova explosion in its last stage of stellar evolution, it likely receives a substantial kick. Such a kick is capable of leaving the binary in an orbit where the spin and the orbital angular momentum are misaligned (Brandt & Podsiadlowski 1995).

The spin will slowly align with the orbital axis through a combination of the Lense-Thirring effect and the internal viscosity of the accretion disk (Bardeen & Petterson 1975). Martin et al. (2008) showed that the alignment time scale is a few times smaller than the life time of the mass-transfer state, typically $t_{align} \sim 10^6 - 10^8$ yr. While this implies that in most XRBs, spin and orbital angular momentum

are likely aligned, it is plausible that they are mis-aligned in a sub-set of young XRBs, especially for HMXBs, given the short main sequence life time of the companion.

In this situation, the jet-wind interaction will become phase dependent. Because the jet propagation and bending time is short compared to the binary orbital period, the analysis presented above applies only to the phase of the binary orbit where the jet is perpendicular to the orbital separation vector $\vec{a}$. For any given orbit, there are two such node points. During other orbital phases, one side of the jet will approach the companion star (*i.e.*, the minimum distance between jet and star is smaller than the orbital separation), while the other side of the jet is receding; the approaching side will be more strongly bent.

We performed a set of simulations to explore this scenario. We define the inclination angle $\pi/2 - \theta_0$ between the initial direction of the jet $\hat{\vec{z}}$ and the orbital separation vector $\vec{a}$, such that

$$\theta_0 = \pi/2 - \cos^{-1}\left(\hat{\vec{z}} \cdot \hat{\vec{a}}\right) \tag{4.22}$$

i.e., $\theta_0 = 0$ implies the jet is perpendicular to $\vec{a}$, corresponding to the case discussed so far, while $\theta_0 = \pi/2$ implies a jet maximally inclined, pointed at the star/away from it. In other words, in the limit of instantaneous reaction of the jet to orbital changes, the angle $\phi_{\rm jet,orbit}$ between the jet and the orbital velocity vector does not affect jet bending (reflected also in the fact that most of our simulations neglect orbital motion entirely). Clearly, for any non-zero jet inclination relative to the orbital axis, the angle θ_0 will change as a function of orbital phase.

Because jet bending reacts instantaneously to orbital changes, the jet will always propagate in a plane spawned by the initial jet direction and the orbital separation vector, to order considered here. For circular binary orbits, the asymptotic

bending angle therefore only depends on θ_0, and only implicitly depends on binary phase through θ_0.

We now extend our analytic formula to the off-axis case. The momentum flux of the jet will be the same, but the accumulated momentum flux of the stellar wind changes with inclination angle. The accumulated wind momentum per unit jet length is then (following eq. (4.14)):

$$\Delta\Phi_{m,\mathrm{wind}}(\theta) = \frac{h_1 \dot{\mathrm{M}}_{\mathrm{wind}} v_{\mathrm{wind}}}{4\pi\, a\, v_{\mathrm{jet}}}\, \tilde{f}(z,\gamma,\theta_0), \tag{4.23}$$

where

$$\tilde{f}(z,\gamma,\theta_0) \equiv (\cos\theta_0)^{-2+1/\gamma} \int_{-\tan\theta_0}^{z/a} dy \left(\frac{1}{1+y^2}\right)^{2-1/\gamma}. \tag{4.24}$$

We can use the ratio of the accumulated wind momentum to jet momentum per unit length, eq. (4.17), to derive the asymptotic bending angle ψ_∞

$$\psi_\infty = \frac{\dot{\mathrm{M}}_{\mathrm{wind}} v_{\mathrm{wind}} v_{\mathrm{jet}}\, h_1}{4\pi\, a\, L_{\mathrm{jet,kin}}}\, \tilde{f}(\gamma,\theta_0), \tag{4.25}$$

where

$$\tilde{f}(\gamma,\theta_0) \equiv \lim_{z\to\infty} \tilde{f}(z,\gamma,\theta_0). \tag{4.26}$$

It is obvious that if θ_0 is 0, this expression reduces to eq. (4.17).

For the approaching side of the jet, which is inclined towards the companion star in our simulation (Figure 4.11), $\tilde{f}(\gamma,\theta_0)$ is monotonically increasing, resulting in stronger bending of the jet.

If θ_0 is larger than some value, the jet collides with the star. Given the binary parameters for Cygnus X-1, this limit angle is 62.18°. The impact region where the jet directly encounters the star is marked by the grey area in the Figure 4.11&4.12.

Figure 4.12 shows ψ_∞ as a function of θ_0, assuming h_1 is kept constant in the approaching side of the jet where it heads toward the companion star. From this

analysis we can infer the jet bending angle for an initially off-axis jet. As one might expect, a more inclined jet will be more strongly bent. The right panel of Figure 4.12 shows ψ_∞ with respect to the orbital plane. The figure shows a monotonic increase of jet bending angle with initial jet inclination.

Figure 4.13 shows the momentum ratio and asymptotic angle for the receding jet. For jets with higher inclination angles, the bending angle is reduced.

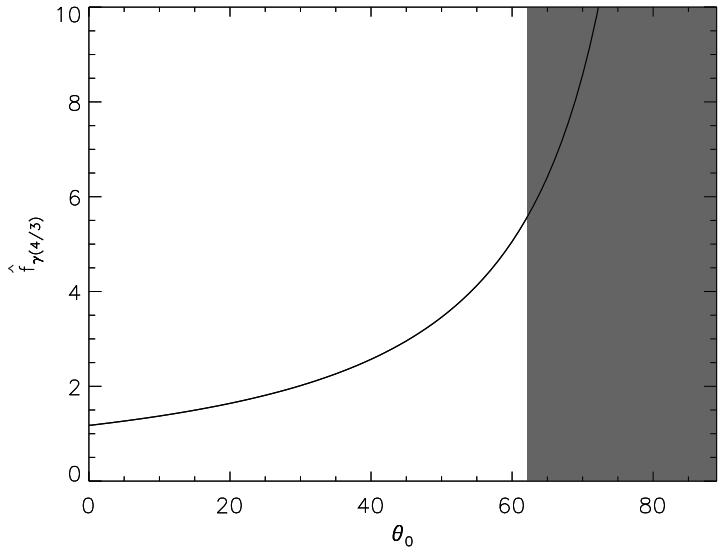

Fig. 4.11. — : Variation of $\tilde{f}$ as a function of θ_0. The grey area shows the impact region where the approaching jet runs into the stellar surface.

Figure 4.14 shows density maps for several cases of the misaligned simulations. All other parameters are the same as in our standard model, SphWind_E36. The inclination angles are 30°, 60°, 75 °, respectively. The magenta solid line represents the analytic jet trajectory which is derived using the assumption of pressure balance between the jet and the ambient medium. For all cases, the approaching jet shows some degree of disruption and dynamical instability and the analytic approximation

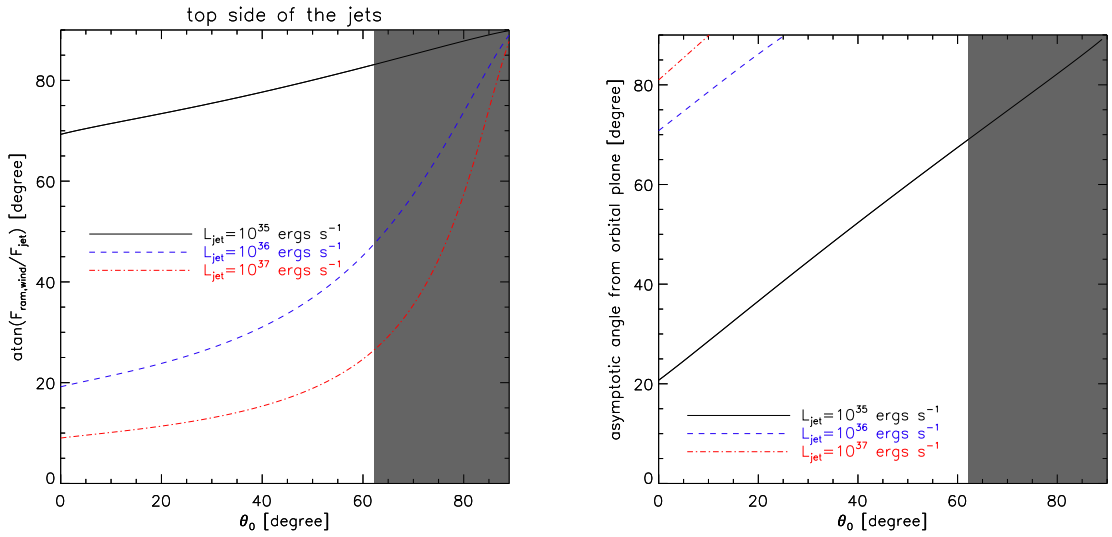

Fig. 4.12. — : Case of approaching jet, initially pointing towards the companion star. Left panel: The ratio of the accumulated wind momentum flux to the jet momentum flux as a function of θ_0. Right panel: Asymptotic jet bending angle with respect to the orbital plane. The grey area shows the impact region where the approaching jet runs into the stellar surface.

breaks down for bending angles larger than about 20°. On the other hand, the figures show that our analytic approach is acceptable for the receding side of the jets.

As one would expect from simple geometric considerations, while a jet launched perpendicular to the orbital separation $\vec{a}$ is bent symmetrically on either side, an inclined jet shows asymmetric behavior between approaching jet and receding jet. Such a configuration would lead to increased jet bending in the approaching jet. Our limit on the jet power in Cyg X-1 was derived under the most conservative assumption that the jet is not inclined relative to the orbital axis. Because jet bending and disruption increase for inclined jets, the possible inclination of the jet will strengthen our limit on the jet power.

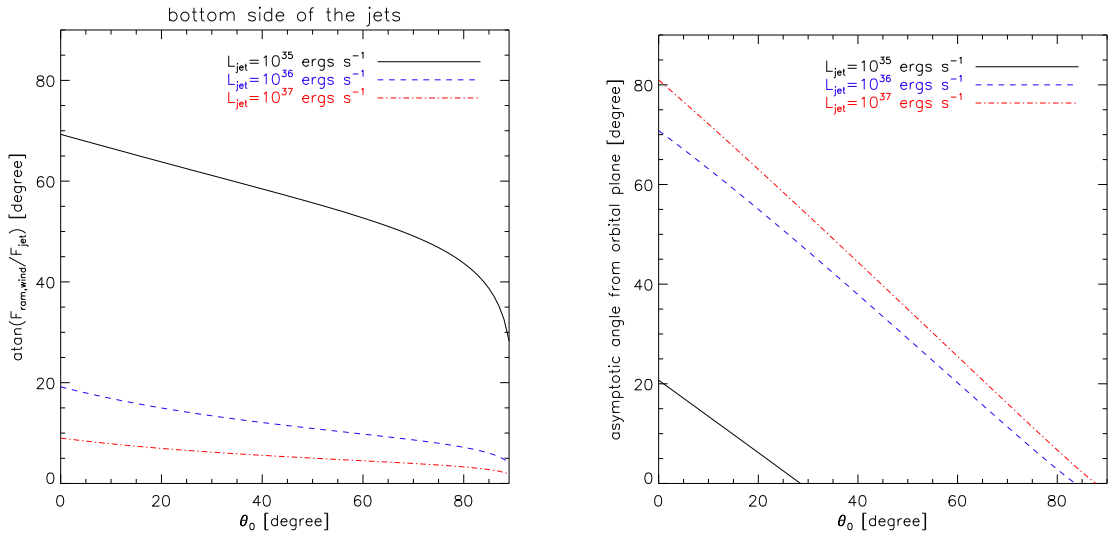

Fig. 4.13. — : Case of receding jet, initially pointing away from the companion star. Same panels as in Figure 4.12

Szostek & Zdziarski (2007) argued that in Cygnus X-1, the orbital modulation of radio emission occurs due to free-free absorption in the asymmetric wind as a function of orbital phase, and the observed phase lag of the modulation with respect to the orbital phase could be attributed to the time delay for the emission from the dynamically curved jet. However, the jet bending we studied in this work is likely not the cause of the phase lag, because the bending direction is parallel to the orbital separation vector, leading to only very small phase lags due to light-travel-time delays, while the observed phase lags would require bending in the direction against the orbital velocity, as argued by Szostek & Zdziarski (2007).

For higher jet inclination angles, (*e.g.* SphWind_E36_60deg or SphWind_E36_75deg), both jet and counter-jet will impact the star once per orbit, leading to jet disruption and reformation; one might thus expect to observe episodic jet eruption from such a system.

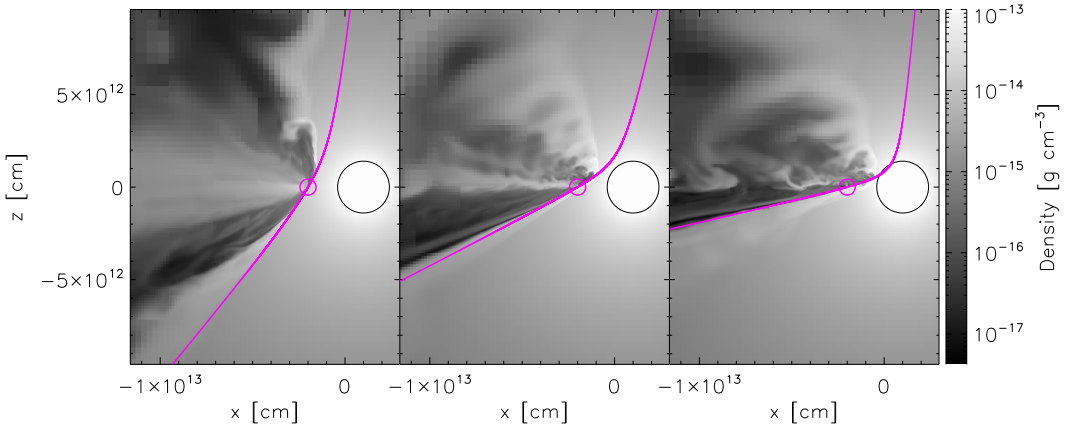

Fig. 4.14. — : Density maps for off-axis jets, deviating from perpendicular direction to orbital plane: 30°, 60°, 75° from left to right panel. The solid magenta line indicates the analytical trajectory of the jet. The magenta circle indicate the location of the black hole.

4.4.6 The case of Cygnus X-3

We can apply a similar argument to the case of Cygnus X-3, an HMXB consisting of a compact object and a Wolf-Rayet companion. In this case, it is still not clear whether the compact object is a black hole or a neutron star, but the observational evidence of collimated jet-like structures is strong in multi-epoch radio maps (Martí et al. 2001). The radio jets with γ-ray flares occur during bright soft X-ray states or during state transitions (Szostek et al. 2008; Tavani et al. 2009).

Dubus et al. (2010) suggested that the jet of Cygnus X-3 is inclined relative to the orbital plane ($20° < \psi_{\rm jet} < 80°$) in order to obtain good fits to the gamma-ray modulation, with a significant offset between the jet footpoint and the site of the gamma-ray emission.

This estimate does not take potential jet bending into account. In fact, as shown above, even if the orbital angular momentum and the jet axis are aligned, we should expect some bending to occur, and the asymptotic jet direction will change over the course of the binary orbit. As a result, the precession of the jet occurs on a time scale, $\tau_{\rm precess} \approx \tau_{\rm orbit}$ in our model. We should point out that there is currently no evidence for (or against) jet precession in Cygnus X-3. The observed gamma-ray modulation can be explained by an inclined jet. An inclined jet is likely bent more than a jet perpendicular to the orbital plane, so jet bending by the jet-wind interaction may have to be taken into account in detailed models of Cygnus X-3.

Assuming the initial jet direction is perpendicular to the orbital plane, we can estimate the bending angle from eq. (4.17) from the binary and jet parameters $L_{\rm jet} = 10^{38}\,{\rm ergs\,s^{-1}}$, $\dot{\rm M}_{\rm wind} = 10^{-5}\,{\rm M_\odot\,yr^{-1}}$, $a = 3 \times 10^{11}{\rm cm}$, $v_{\rm wind} = 10^{8}\,{\rm cm\,s^{-1}}$, and $v_{\rm jet} = 0.5\,c$ as used by Dubus et al. (2010).

Note that Cygnus X-3 is a considerably tighter system with higher inferred jet energy than Cygnus X-1, while the momentum flux from its neighboring Wolf-Rayet star is higher than that from OB companion in Cygnus X-1. In terms of the fiducial parameters given above, the jet bending angle can be calculated from eqs. (4.9) and (4.17) as

$$\psi_\infty \sim 2.35^\circ \times \left(\frac{\dot{\rm M}_{\rm wind}}{10^{-5}\,{\rm M_\odot\,yr^{-1}}}\right)^{1/2} \left(\frac{v_{\rm wind}}{10^{8}\,{\rm cm\,s^{-1}}}\right)^{1/2} \left(\frac{v_{\rm jet}}{0.5\,c}\right)^{1/2} \left(\frac{L_{\rm jet}}{10^{38}\,{\rm ergs\,s^{-1}}}\right)^{-1/2} \left[\frac{f(\gamma)}{f(\gamma=4/3)}\right] \left[\frac{\sin\alpha_0}{\sin\left(2^\circ\right)}\right], \tag{4.27}$$

indicating that for jet bending to be important, the initial opening angle of the jet would have to be significantly larger than a few degrees, or the jet would have to be

strongly misaligned with the orbital axis, with the jets very closely approaching the stellar surface for part of the orbit.

4.4.7 Recollimation in Strong Jet Kinetic Power

In §4.3.2, I performed calculations assuming that the recollimation shock takes place at a distance $\ll a$, where a is the separation between the black hole and the companion star. In our simulations, a jet with a moderate jet kinetic power, $10^{37}\,\mathrm{ergs\,s^{-1}}$ interacts with a strong wind with a high mass loss rate of $\dot{M}_{\rm wind} = 10^{-5}\,\mathrm{M_\odot\,yr^{-1}}$, generating recollimation shock at $z \approx 7 \times 10^{11}\,\mathrm{cm}$. However, if a jet has a sufficiently strong kinetic power, a recollimation shock in the jet can take place at distances comparable to a, or not happen at all. Zdziarski et al. (2015) expressed the critical jet kinetic power, above which the jet is not recollimated, as

$$L_{\rm jet} \leq L_{\rm jet,crit} = \frac{1}{8}\dot{M}_{\rm wind}\, v_{\rm wind}\, v_{\rm jet}, \tag{4.28}$$

where the velocities are constant.

We performed 3-D hydrodynamic simulations for testing the presence of recollimation shock for such high jet kinetic powers. All parameters of jets and stellar winds are the same as the parameters in the model SphWind_E37, except for the jet kinetic power. We carried out two simulations with different jet kinetic power, $L_{\rm jet} = 3 \times 10^{37}$ and $10^{38}\,\mathrm{ergs\,s^{-1}}$. (we named the models as SphWind_3E37 and SphWind_E38).

4.4.7.1 Jet Bending in a conical Jet

Even for such high jet kinetic power ($L_{\rm jet} = 10^{38}\,\mathrm{ergs\,s^{-1}}$), the jet is slightly bent by a transverse pressure gradient that the wind drives around the jet. Therefore, we firstly identified the jet center to estimate the jet thickness in a y-direction (See

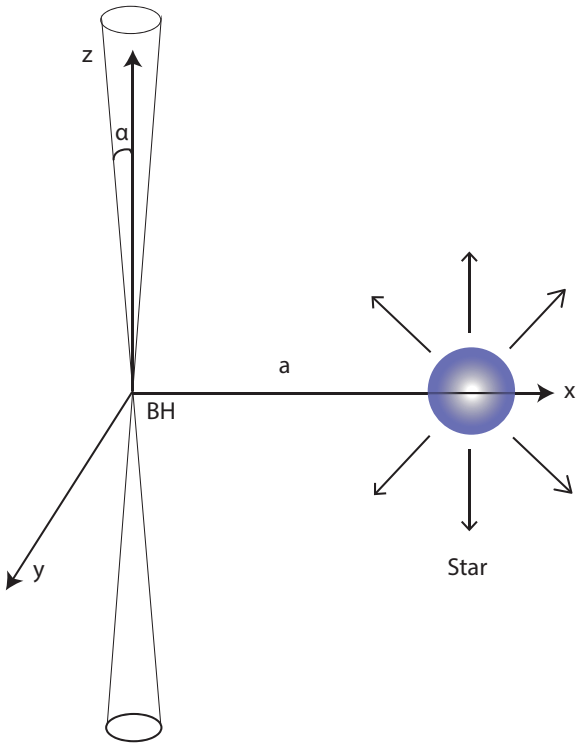

Fig. 4.15. — : Sketch for the numerical configuration. The black hole and the star are located at $x_{\rm black\,hole} = -2 \times 10^{12}\,{\rm cm}$ and $x_{\rm star} = 10^{12}\,{\rm cm}$, respectively. The jet direction is perpendicular to the orbital plane (*i.e.,* z-direction), and the star launches an isotropic and uniform stellar wind.

Figure 4.15). Figure 4.16 shows how the jet deviates from its initial direction, which is parallel to the z-direction. The yellow symbols identify the jet center and the red lines are analytic curves. The figure shows good agreement, indicating that the simple analytic model can describe the bending jet.

For the analytic jet bending model, we assume a conical-shaped jet. In this model, the jet opening angle, α, is fixed, and the jet has a conical shape (See Figure 4.15). In §4.4.1, we used the analytic jet model in which the jet is confined by pressure equilibrium between the jet and the wind. However, as we discuss in

the §4.4.7.2, jets in this test are not recollimated, but maintain their initial opening angle; therefore, we adopt a conical shape for the analytic jet model for this work.

Assuming that the longitudinal jet velocity is constant and the mach number of the jet is high $\mathcal{M}_{\rm jet} \gg 1$, the longitudinal jet momentum flux per unit jet length can be calculated by

$$\Phi_{\rm m,jet} = \int dA_{\perp} \rho_{\rm jet}\, v_{\rm jet} = \frac{L_{\rm jet,kin}}{v_{\rm jet}^2}, \tag{4.29}$$

where $dA_{\perp}$ is the area perpendicular to the initial jet direction.

The transverse wind momentum per unit jet length accumulated by the jet can be derived as a function of z;

$$\Delta\Phi_{\rm m,wind} = \frac{1}{v_{\rm jet}} \int_0^z dz\, v_{\perp,\rm wind}^2(z)\, \rho_{\rm wind}(z)\, h(z), \tag{4.30}$$

where the transverse wind velocity, $v_{\perp,\rm wind}(z) \approx v_{\rm wind,0}\, a/\sqrt{a^2+z^2}$; the wind density in the jet position, $\rho_{\rm wind}(z) = \rho_{\rm wind,0}\, a^2/(a^2+z^2)$; and jet width, $h(z) = 2\, z\, \tan\alpha$. Here, $\rho_{\rm wind,0}$ and $v_{\rm wind,0}$ are the wind density and velocity at the black hole, and a is the orbital separation. Therefore, the eq. 4.30 can be integrated to

$$\begin{aligned} \Delta\Phi_{\rm m,wind} &= \frac{v_{\rm wind,0}^2\, \rho_{\rm wind,0}\, a^2\, \tan\alpha}{v_{\rm jet}} \frac{z^2}{a^2+z^2} \\ &= \frac{v_{\rm wind,0}\, \dot{M}_{\rm wind}\, \tan\alpha}{4\,\pi\, v_{\rm jet}} \frac{z^2}{a^2+z^2}, \end{aligned} \tag{4.31}$$

where the wind mass-loss rate, $\dot{M}_{\rm wind} = 4\pi\, a^2\, \rho_{\rm wind,0}\, v_{\rm wind,0}$.

In the first-order approximation, the jet bending angle can be derived by the ratio between the accumulated transverse momentum and the longitudinal momentum as a function of z;

$$\psi(z) = \frac{\Delta\Phi_{\rm m,wind}}{\Phi_{\rm m,jet}} = \frac{v_{\rm wind,0}\, v_{\rm jet}\, \dot{M}_{\rm wind}\, \tan\alpha}{4\,\pi\, L_{\rm jet,kin}} \frac{z^2}{a^2+z^2}. \tag{4.32}$$

In the small-angle approximation, we can derive the analytic jet trajectory through $d(x - x_0)/dz = \tan\psi$, where x_0 is the black hole location. Figure 4.16 shows good agreement between this model (solid red lines) and the simulations (yellow symbols). The amount of bending angle is similar between SphWind_3E37 and SphWind_E38, because, although Le38 is 3 times larger in jet kinetic power than SphWind_3E37, the opening angle of SphWind_E38 is also 2.4 times larger than that of SphWind_3E37 (see §4.4.7.2).

4.4.7.2 Recollimations

To check the presence of recollimation shock, we measured the jet width facing the star (*i.e.* y-direction). Since the jet is bent in both cases, we measured the width along the jet center (yellow symbol in Figure 4.16). Figure 4.17 shows that the identified jet width increases linearly without recollimation. The opening angles are $\alpha_{\rm SphWind\_3E37} = 3.4^\circ$ and $\alpha_{\rm SphWind\_E38} = 8^\circ$.

To check the linear expansion of the jet, we superposed straight lines from the black hole to the end of jet (red lines in Figure 4.17). Then we calculated the fractional deviation as a function of z, $\sigma(z) = [y^2_{\rm jet,line}(z) - y^2_{\rm jet,data}(z)]/y^2_{\rm jet,line}(z)$, where $y_{\rm jet,data}$ and $y_{\rm jet,line}$ are the y positions of the jet edge for the data and the straight line, respectively. Figure 4.18 shows that in SphWind_E38, the identified jet has an excellent agreement with the linear line, indicating the conical shape of the jet. The identified jet in SphWind_3E37 also has a conical shape, but the deviation in lower height, $z \lesssim 5 \times 10^{12}\,{\rm cm}$, is negative, indicating that the initial opening angle of SphWind_3E37 may be larger than 3.4°, which is the opening angle of jet $\alpha_{\rm SphWind\_3E37}$.

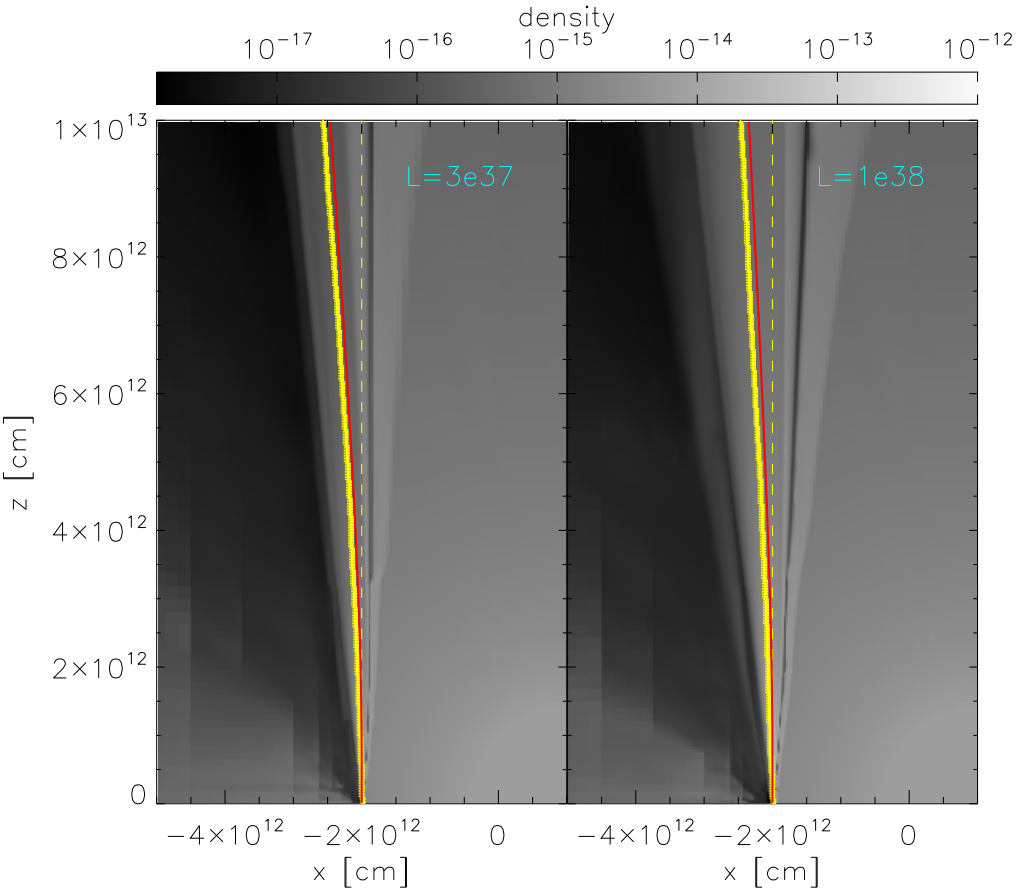

Fig. 4.16. — : Density contour map in x-z plane for SphWind_3E37(left) and SphWind_E38(right) models. The yellow dashed line represents a vertical line at the black hole position. The yellow symbols represent identified jet center from simulations and the red solid line represents analytic trajectory of the jet.

4.4.8 Caveats

Our simulations were carried out using an isotropic and homogeneous stellar wind model. This assumption allows us to study the dynamics of jet-wind interaction in a simple analytic framework. Several complications will affect this process in ways not included in this paper.

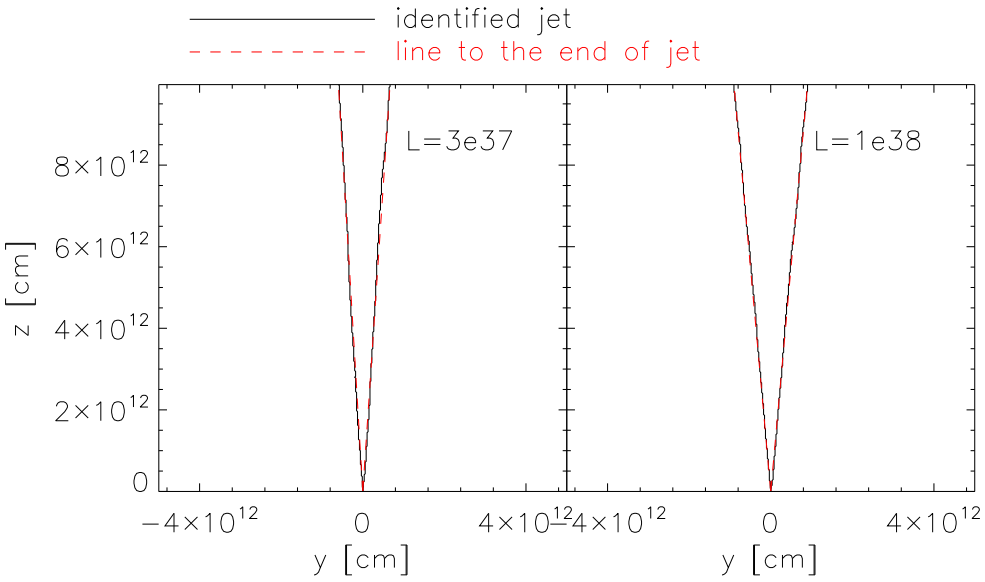

Fig. 4.17. — : The jet in y-direction as a function of z. The black solid line represents the jet identified from the simulation, and the red line represents the straight line between the black hole and the end of the jet.

4.4.8.1 X-ray Ionization

Firstly, the X-ray flux from the accretion disk may be intense enough to ionize the circum-stellar gas, so the wind can be reduced or quenched, decreasing the jet bending angle. Line driving is likely inefficient in the illuminated portion of the wind if the ionization parameter is above a critical threshold. Conversely, the X-ray illumination can itself produce thermal wind driving by heat input. The exact configuration of the wind is therefore not entirely clear.

However, from the fact that the black hole in Cygnus X-1 is accreting from the companion wind, the illuminated portion of the wind must be of similar density to that assumed in the shadowed region, which suggests that the estimates presented

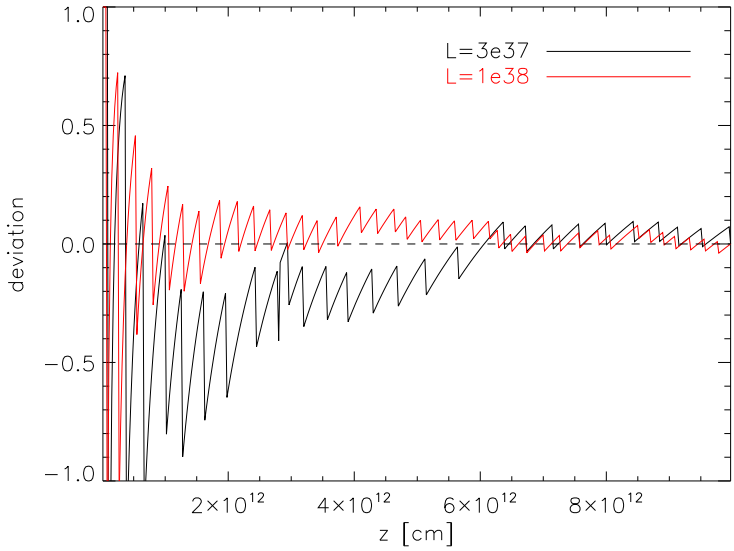

Fig. 4.18. — : Fractional deviation between the measured jet edge in y-direction and the linear line. The black and red colors represent SphWind_3E37 and SphWind_E38, respectively. The horizontal dashed line indicates no deviation.

above will not be changed drastically by the effects of ionization of the wind.

4.4.8.2 Clumping

More importantly, the stellar wind from OB-type stars is likely clumpy (Oskinova et al. 2012). Poutanen et al. (2008) suggested that the wind in Cygnus X-1 is clumped, based on dips in the X-ray lightcurve.

This situation was simulated by P12. Because global simulations that incorporate clumped winds with realistic clump sizes and densities will be computationally impossible in the foreseeable future, given the large dynamic range and resolution required to capture the mass in small clumps, our paper should be considered complementary to the work presented in P12.

While a detailed treatment of clumping in our simulations is beyond the scope

of this paper, we will briefly discuss how significant clumping would affect the results of our simulations. For a fixed mass loss rate and wind velocity, the net effect of wind clumping will depend on the filling factor, the average size of the clumps, and the density contrast. Since secular bending is facilitated by the pressure gradient across the jet, we should expect bending in the presence of clumps to be reduced by the amount the momentum flux in the hot low-density background component of the wind is reduced relative to an un-clumped wind. The reduction is set by the density ratio of the hot/low density background component $\rho_{\rm hot}$ to the density $\rho_{\rm wind}$ of an un-clumped wind of the same emission measure.

Since $\rho_{\rm hot}$ is poorly constrained, we cannot easily quantify the reduction expected in the bending angle by the presence of clumps. Clearly, if $\rho_{\rm hot}$ is of the same order as the estimates of $\rho_{\rm wind}$ used above, our results will be unaffected. However, if $\rho_{\rm hot} \ll \rho_{\rm wind}$, the amount of secular bending of the jet will be reduced by the density ratio $\rho_{\rm hot}/\rho_{\rm wind}$.

In the case of O-star winds in HMXBs, the presence of clumps in the illuminated side of the wind is even less well constrained, given the effects X-ray ionization may have on clump formation.

For all these reasons, a general statement about how our results change in the presence of clumping is difficult to make. However, considering the possible limits of clump sizes and density, we can estimate under which circumstances the jet would be able to propagate through the wind without disruption and derive similar constraints on the jet power for a given set of clump parameters.

If the density contrast between the clumps and the background wind is small, corrections should naturally be minor and the limit on the jet power from eq. (4.21)

will hold. If the density contrast is large and most of the mass is carried in clumps, the effect will depend on the average size of the clumps, relative to the width h of the jet:

Large clumps: If the clumps are large compared to the cross section of the jet, jet-clump interaction will be disruptive, and the conclusions of P12 hold, *i.e.*, the jet will be disrupted unless it is sufficiently powerful to escape, in the case investigated by P12, $L_{\rm jet} \gtrsim 10^{37}\,{\rm ergs\,s^{-1}}$, similar to the conclusion we reach in this paper, with the main difference being that interaction with a clumpy wind introduces significant stochasticity, which, in the case of Cygnus X-1. It has been suggested by Zdziarski et al. (2011) that fluctuations in the radio light curve may be an expression of such interaction.

Small clumps: If the clumps are much smaller than the cross section of the jet, such that the typical clump radius satisfies $R_{\rm clump} \ll h_{\rm jet}$, they will act like bullets passing through the jet, generating small bow shocks that slow down a small fraction of the jet. Small clumps will only globally disrupt the jet if **(a)** the covering fraction $f_{\rm clumps}$ of clumps is larger than unity *and* **(b)** the total mass within clumps is sufficiently high to stop the jet fluid. *Both* conditions must be met for the jet to be disrupted by wind whose mass flux is dominated by small clumps.

Note that in this case, jet disruption will not be stochastic, since it requires the presence of many small clouds passing through the jet continuously, rather than a few large clouds. Since the jet in Cygnus X-1 is *not* disrupted continuously, at least one of the two conditions for jet disruption must be violated. We can now estimate the constraints the observed stability of the jet against wind disruption places on the jet and cloud parameters.

(a) Low covering fraction: The covering fraction $f_{\rm cover}$ of clumps is given by

$$f_{\rm cover} = \int_0^\infty dz \frac{f}{R_{\rm clump}} \sim \frac{a f_{\rm vol}}{R_{\rm clump}} \tag{4.33}$$

where z is the path length along the jet, a is the orbital separation, and $f_{\rm vol}$ is the clump volume filling factor. If $f_{\rm cover} \gg 1$, the jet *may* be disrupted if the total mass within clumps is sufficiently high to stop the jet fluid ($f_{\rm clumps} \gg 1$ is a necessary condition for jet disruption). Conversely, a *sufficient but not necessary* condition for the jet *not* to be disrupted is that the covering fraction of clumps is small, $f_{\rm cover} \ll 1$, or

$$f_{\rm vol} \ll \frac{R_{\rm clump}}{a} \ll 1 \tag{4.34}$$

The condition that the emission measure of the clumped wind is the same as that of the un-clumped wind (in the optically thin limit) gives a clump volume filling fraction of $f_{\rm vol} = \rho^2_{\rm wind}/\rho^2_{\rm clump}$ or $\sqrt{f_{\rm vol}}\,\rho_{\rm clump}/\rho_{\rm wind} = 1$. With eq. (4.34), the condition $f_{\rm cover}$ implies that the wind mass loss rate must satisfy

$$\dot{\rm M}_{\rm wind,clumped} = \frac{\rho_{\rm clump} f_{\rm vol}}{\rho_{\rm wind}} \dot{\rm M}_{\rm wind} = \sqrt{f_{\rm vol}}\,\dot{\rm M}_{\rm wind} \ll \dot{\rm M}_{\rm wind} \sqrt{\frac{R_{\rm clump}}{a}} \ll \dot{\rm M}_{\rm wind} \tag{4.35}$$

(b) Low mass density: A second necessary condition for clumps in the wind to significantly disrupt the jet is that the clump mass $\Delta {\rm M}_{\rm clump}$ intercepted by the jet exceed the inertial mass of the jet plasma, ${\rm M}_{\rm jet}$. Conversely, a second *sufficient but not necessary* condition for the jet *not* to be disrupted is

$${\rm M}_{\rm jet} = \int_0^\infty dz A_{\rm jet} \rho_{\rm jet,inertial} \gg \int_0^\infty dz A_{\rm jet} f \rho_{\rm clump} = \Delta {\rm M}_{\rm clump} \tag{4.36}$$

which we can simplify as the condition

$$\rho_{\rm jet} \gg f_{\rm vol} \rho_{\rm clump} \tag{4.37}$$

Assuming that the location of the re-collimation shock of the jet is set by the ram pressure of the hot, low density background gas of the clumped wind, we can use eqs. (4.5) and (4.8) to write this condition as

$$f_{\rm vol}\frac{\rho_{\rm clump}}{\rho_{\rm hot}} \ll \frac{v_{\rm wind}^2 \mathcal{M}_{\rm jet,0}^2}{v_{\rm jet}^2} = \frac{v_{\rm wind}^2}{c_{\rm s,jet,0}^2} \tag{4.38}$$

where $\rho_{\rm hot} \ll \rho_{\rm wind} \ll \rho_{\rm clump}$ is the density of the hot background wind in the clumped wind scenario. This condition can be written as a limit on the wind mass flux:

$$\dot{\rm M}_{\rm wind,clumped} \ll \frac{\rho_{\rm hot}}{\rho_{\rm wind}}\frac{v_{\rm wind}^2}{c_{\rm s,jet,0}^2}\dot{\rm M}_{\rm wind} \ll \dot{\rm M}_{\rm wind} \tag{4.39}$$

where the last inequality reasonably assumes that $c_{\rm s,jet,0} > v_{\rm wind}$.

In summary, we can distinguish the following three cases, one of which must apply to Cygnus X-1:

1. The wind is not strongly clumped (that is, the mass flux in the diffuse/background wind is comparable to the mass flux used in this paper, even if clumps are present). In this case, our limit in eq. (4.21) applies and the jet must be powerful to propagate through the wind.

2. The wind is strongly clumped, with large clumps of size $R \gtrsim h$; in this case, the analysis of P12 applies and the jet must be powerful to propagate through the wind.

3. The wind is strongly clumped, with small clumps of size $R \ll h$; in this case, the mass loss rate must be orders of magnitude below the mass loss rate of an un-clumped wind, given the observed emission measure and lack of jet disruption. In this case, we cannot use the observed lack of jet disruption/bending to derive a limit on the jet power.

Thus, (a) either the wind mass loss rate must be orders of magnitude smaller than the nominal wind parameters for a uniform wind for the companion star, with important implications for wind formation in HMXBs, and/or (b) the jet power must be large [eq. (4.21)], similar to the conclusion reached from energy estimates of the large scale nebula.

4.5 Conclusion

We performed global hydrodynamic simulations to study jet-wind interaction in the wind of the companion star in HMXBs. The interaction results in the jet being bent with a characteristic bending angle that depends on the properties of the jet and the wind. Using the small bending angle approximation, we derived a simple analytic formula for the asymptotic bending angle. The formula is consistent with the numerical results, and it can be used to analyze observations of jets in HMXBs. We showed that the analysis is valid for bending angles smaller than about 20°.

We applied the formula to two observed HMXBs, Cygnus X-1 and Cygnus X-3. We constrained the jet power in Cygnus X-1 to be $L_{\rm jet} \gtrsim 10^{36}\,{\rm ergs\,s^{-1}}$ from the lack of observed precession of the VLBA jet. This limit is consistent with previous estimates, but derived from completely independent arguments and likely more robust.

Given Cygnus X-3 parameters, we argued that the jet bending is likely not significant, unless the jet in Cygnus X-3 has a large opening angle α or is significantly less powerful than estimated in previous studies.

The main caveat in the application of this model to observed HMXBs is the lack of knowledge about the properties of wind clumping in massive stars. We discussed conditions under which clumping will affect the analysis of jet bending presented

in this paper, and under which clumps themselves will lead to observable dynamic disruption of the jet. We showed that, if wind clumping is dynamically important for the jet-wind interaction in Cygnus X-1, our limit on the jet power holds unless the wind mass loss rate is orders magnitude below the nominal wind parameters derived for a uniform wind (in which case we would not be able to constrain the jet power from the lack of disruption or bending by the wind).

References

Bardeen, J. M., & Petterson, J. A. 1975, ApJ, 195, L65

Begelman, M. C., Rees, M. J., & Blandford, R. D. 1979, Nature, 279, 770

Brandt, N., & Podsiadlowski, P. 1995, MNRAS, 274, 461

Brocksopp, C., Tarasov, A. E., Lyuty, V. M., & Roche, P. 1999, A&A, 343, 861

Castor, J. I., Abbott, D. C., & Klein, R. I. 1975, ApJ, 195, 157

Castor, J. L. 1974, MNRAS, 169, 279

Dubus, G., Cerutti, B., & Henri, G. 2010, MNRAS, 404, L55

Freeland, E., & Wilcots, E. 2011, ApJ, 738, 145

Friend, D. B., & Castor, J. I. 1982, ApJ, 261, 293

Fryxell, B., Olson, K., Ricker, P., et al. 2000, ApJS, 131, 273

Gallo, E., Fender, R., Kaiser, C., et al. 2005, Nature, 436, 819

Gies, D. R., & Bolton, C. T. 1982, ApJ, 260, 240

Gies, D. R., Bolton, C. T., Blake, R. M., et al. 2008, ApJ, 678, 1237

Hadrava, P., & Čechura, J. 2012, A&A, 542, A42

Heinz, S., & Begelman, M. C. 2000, ApJ, 535, 104

Heinz, S., Brüggen, M., Young, A., & Levesque, E. 2006, MNRAS, 373, L65

Heinz, S., Grimm, H. J., Sunyaev, R. A., & Fender, R. P. 2008, ApJ, 686, 1145

Hjellming, R. M., Stewart, R. T., White, G. L., et al. 1990, ApJ, 365, 681

Lee, D., & Deane, A. E. 2009, Journal of Computational Physics, 228, 952

Martí, J., Paredes, J. M., & Peracaula, M. 2001, A&A, 375, 476

Martin, R. G., Reis, R. C., & Pringle, J. E. 2008, MNRAS, 391, L15

McNamara, B. R., & Nulsen, P. E. J. 2007, ARA&A, 45, 117

Miller, J. M., Wojdowski, P., Schulz, N. S., et al. 2005, ApJ, 620, 398

Mirabel, I. F., & Rodríguez, L. F. 1999, ARA&A, 37, 409

Morsony, B. J., Miller, J. J., Heinz, S., et al. 2013, MNRAS, 431, 781

Orosz, J. A., McClintock, J. E., Aufdenberg, J. P., et al. 2011, ApJ, 742, 84

Oskinova, L. M., Feldmeier, A., & Kretschmar, P. 2012, MNRAS, 421, 2820

Owocki, S. P., Castor, J. I., & Rybicki, G. B. 1988, ApJ, 335, 914

Perucho, M., & Bosch-Ramon, V. 2012, A&A, 539, A57

Pooley, G. G., Fender, R. P., & Brocksopp, C. 1999, MNRAS, 302, L1

Poutanen, J., Zdziarski, A. A., & Ibragimov, A. 2008, MNRAS, 389, 1427

Puls, J., Vink, J. S., & Najarro, F. 2008, A&A Rev., 16, 209

Russell, D. M., Fender, R. P., Gallo, E., & Kaiser, C. R. 2007, MNRAS, 376, 1341

Sell, P. H., Heinz, S., Richards, E., et al. 2015, MNRAS, 446, 3579

Stirling, A. M., Spencer, R. E., de la Force, C. J., et al. 2001, MNRAS, 327, 1273

Szostek, A., & Zdziarski, A. A. 2007, MNRAS, 375, 793

Szostek, A., Zdziarski, A. A., & McCollough, M. L. 2008, MNRAS, 388, 1001

Tavani, M., Bulgarelli, A., Piano, G., et al. 2009, Nature, 462, 620

van Kerkwijk, M. H. 1993, A&A, 276, L9

Wiersema, K., Russell, D. M., Degenaar, N., et al. 2009, MNRAS, 397, L6

Yoon, D., Morsony, B., Heinz, S., et al. 2011, ApJ, 742, 25

Zdziarski, A. A., Mikołajewska, J., & Belczyński, K. 2013, MNRAS, 429, L104

Zdziarski, A. A., Skinner, G. K., Pooley, G. G., & Lubiński, P. 2011, MNRAS, 416, 1324

Zdziarski, A. A., Yoon, D., & Sikora, M. 2015, in prep.

Chapter 5

Conclusion

In this thesis I have presented the theoretical study of the interactions between relativistic outflows from compact objects and the surrounding medium. Through analytic and numerical calculations, I have demonstrated how these interactions play a significant roles on the dynamical evolution of microquasar jets or pulsar winds, and can be used as diagnostics of jets and environment.

5.1 Fast-moving Low-mass X-ray Binaries

A subset of microquasars is moving through the interstellar medium with high spatial velocity, $v > 100\,\mathrm{km\,s^{-1}}$, due to the kicks they receive when being born in supernovae. In Chapter 2, I have presented the morphological evolution and dynamics of these fast-moving microquasars by means of 3-D hydrodynamic simulations.

The microquasar initially creates a powered, spherically expanding bubble. As it reaches the edge of the bubble, it establishes a well-defined structure with a bow shock and a trailing neck connecting the bow shock and the bubble. The shocks from these structures create collisionally excited H_α emissions. In fact, Wiersema et al. (2009) detected the bow shock head of the nebula of SAX J1712.6-3739 in H_α, and in the ensuing study the apparent expanding bubble structure behind the object was detected in H_α(see Figure 5.1).

I also presented calculations of the detectability of the structures in other spectral bands. Using the XIM program (Heinz & Brüggen 2009), I simulated *Chandra* X-ray observations of the objects. The result shows that X-ray emission is detectable around all these structures in early phases, but the emission around the bubble and neck will fade as the shock temperature decreases. As a result, the emission will be detected only around the bow shock in later phases. Under the assumption that the

plasma is in equipartition, I calculated the *upper limits* of observable synchrotron emission. This shows that the interior of the bubble will be visible in synchrotron emission due to the energetic flows transferred from the microquasar jet.

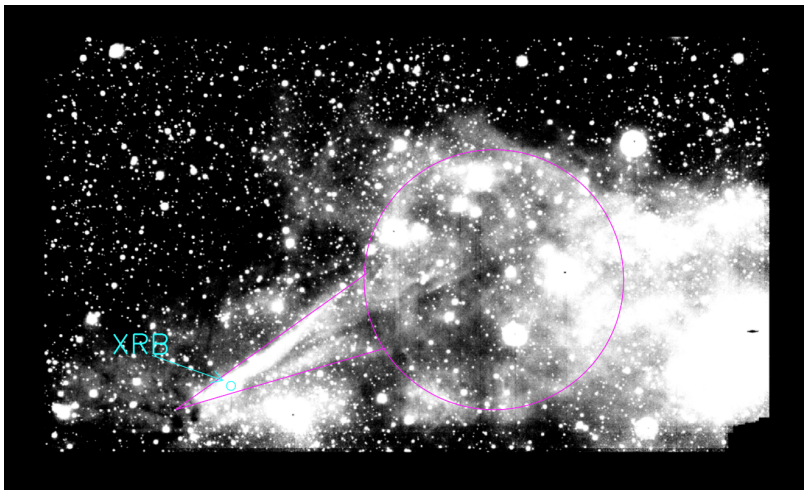

Fig. 5.1. — : SAX J1712.6-3739 image from the VLT FORS2 H_α data with location of neck and bubble highlighted (Yoon et al. 2011).

5.2 Bow Shock Pulsar Wind Nebulae around a Non-uniform Ambient Density

I extended the results from Chapter 2 into bow shock PWNe, since bow shock structures of the nebulae are similar with those of fast-moving microquasars. The peculiar multiple bubbles in the Guitar Nebula motivated me to study the effects of inhomogeneous ISM around bow shock PWNe (see Figure 5.2). In Chapter 3, I have presented models of the evolution of a bow shock and a trailing neck when the pulsar encounters broad density gradients or density discontinuities. I carried out 2-D(axisymmetric)/3-D hydrodynamic simulations for this study.

The analytic and numerical calculations for the bow shock head indicate that if

the pulsar passes through a density gradient in the medium which is decreasing, the bow shock becomes wider, producing a more flattened trailing neck. This morphology has a good agreement with the observed Guitar head from Chatterjee & Cordes (2004), indicating that the ambient density decreases along the pulsar's passage over past several years.

When a pulsar is born, it produces an expanding bubble shell initially. If the pulsar has a high spatial velocity and is old enough to move far away from its birth-place, the initial bubble will be invisible. However, some bow shock PWNe have a bubble behind the pulsar, which requires a mechanism to produce the bubble. I showed that if a pulsar passes through the density discontinuity in which the density decreases, a bubble can be generated due to the sudden increase in standoff distance.

Based on this result, I proposed a possible scenario for generating the guitar shape in the Guitar Nebula. I set a series of density change in the medium, and successfully reproduced the shape and narrow neck connecting between the pulsar and the bubble.

5.3 High-mass X-ray Binaries

A strong stellar wind from a high-mass companion star significantly affects nearby microquasar jets in HMXB. The jet-wind interaction results in the jet being bent with a characteristic bending angle that depends on the properties of the jet and the wind. In Chapter 4, I derived an analytic formula for the asymptotic bending angle which can be used to analyze observations of jets in HMXBs. Hydrodynamic simulations in 3-D showed that the asymptotic jet-bending angle varies dramatically with the strength of jet kinetic powers relative to the wind thrust.

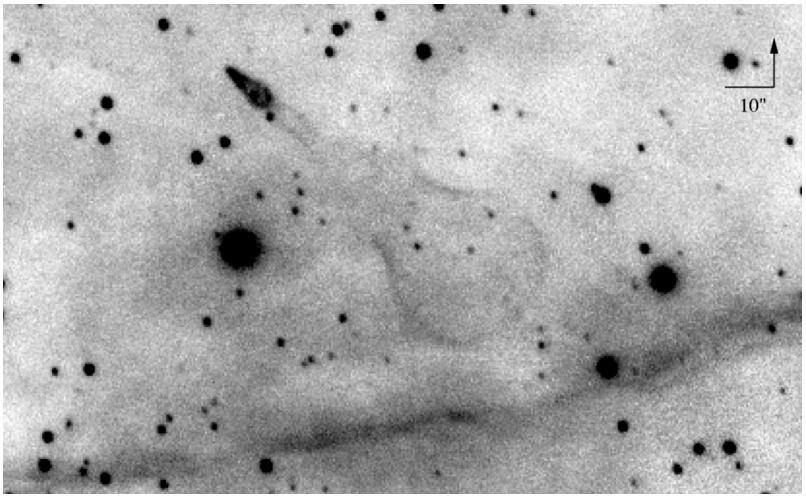

Fig. 5.2. — : Guitar Nebula in H_α (20 Å filter at 6564 Å), imaged with the 5 m Hale Telescope at Palomar Observatory in 1995 (Chatterjee & Cordes 2002).

Stirling et al. (2001) detected a well-resolved radio jet in Cygnus X-1 (see Figure 5.3). I applied the analytic formula, and constrained the jet kinetic power in Cygnus X-1 to be $L_{\rm jet} \gtrsim 10^{36}\,{\rm ergs\,s^{-1}}$. This limit is consistent with previous estimates, but it is derived from completely independent arguments and is likely more robust. I also analysed observations of Cygnus X-3, and argue that the jet bending is likely not significant.

In this study, I assumed that the stellar wind is isotropic and uniform. However, the wind from an OB-type star is likely clumpy (Oskinova et al. 2012). While the clumpy wind is currently numerically impossible to develop, because it requires extremely high resolution and small time scale, I argue analytically that the jet can maintain its shape against the clumpy wind, if either the wind mass-loss rate has orders of magnitude smaller than the nominal wind parameters for a uniform wind, or if the jet kinetic power is sufficiently large.

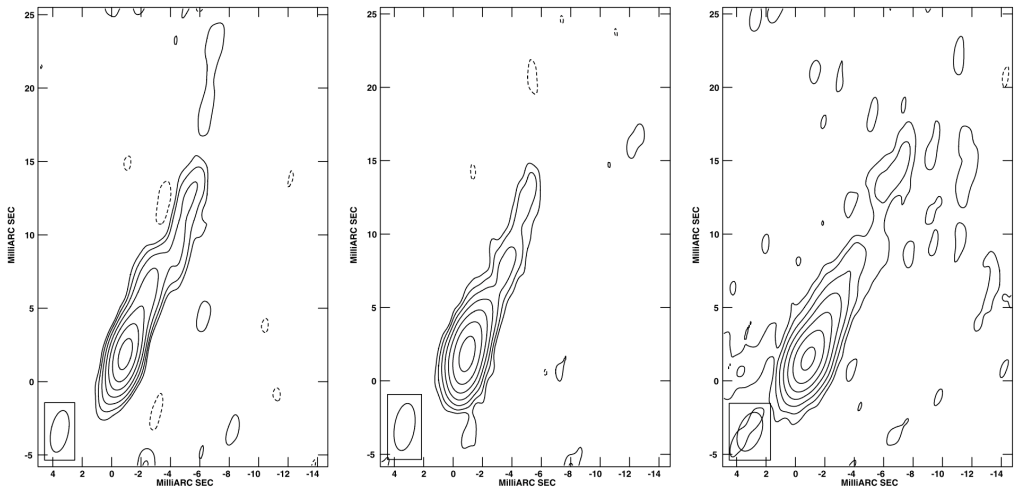

Fig. 5.3. — : Very Long Baseline Array (VLBA) and phased Very Large Array (VLA) images of Cygnus X-1 from 1998 at 8 GHz (Stirling et al. 2001).

References

Chatterjee, S., & Cordes, J. M. 2002, ApJ, 575, 407

—. 2004, ApJ, 600, L51

Heinz, S., & Brüggen, M. 2009, ArXiv e-prints, arXiv:0903.0043

Oskinova, L. M., Feldmeier, A., & Kretschmar, P. 2012, MNRAS, 421, 2820

Stirling, A. M., Spencer, R. E., de la Force, C. J., et al. 2001, MNRAS, 327, 1273

Wiersema, K., Russell, D. M., Degenaar, N., et al. 2009, MNRAS, 397, L6

Yoon, D., Morsony, B., Heinz, S., et al. 2011, ApJ, 742, 25